

**Transition Metal Chalcogenide (Cadmium Sulfide) Nanoparticles: (Bio)synthesis,  
Characterization and Photoelectrochemical Performance**

by

Yaying Feng

Department of Mechanical Engineering and Materials Science  
Duke University

Date: \_\_\_\_\_

Approved:

\_\_\_\_\_  
Stefan Zauscher, Advisor

\_\_\_\_\_  
Jeffrey T. Glass

\_\_\_\_\_  
Lingchong You

\_\_\_\_\_  
David Mitzi

\_\_\_\_\_  
Maiken Mikkelsen

Dissertation submitted in partial fulfillment of  
the requirements for the degree of Doctor  
of Philosophy in the Department of  
Mechanical Engineering and Materials Science in the Graduate School  
of Duke University

2019

ABSTRACT

**Transition Metal Chalcogenide (Cadmium Sulfide) Nanoparticles: (Bio)synthesis,  
Characterization and Photoelectrochemical Performance**

by

Yaying Feng

Department of Mechanical Engineering and Materials Science  
Duke University

Date: \_\_\_\_\_

Approved:

\_\_\_\_\_  
Stefan Zauscher, Advisor

\_\_\_\_\_  
Jeffrey T. Glass

\_\_\_\_\_  
Lingchong You

\_\_\_\_\_  
David Mitzi

\_\_\_\_\_  
Maiken Mikkelsen

An abstract of a dissertation submitted in partial  
fulfillment of the requirements for the degree  
of Doctor of Philosophy in the Department of  
Mechanical Engineering and Materials science in the Graduate School of  
Duke University

2019

Copyright by  
Yaying Feng  
2019

## **Abstract**

Cadmium sulfide (CdS) is one of the most commonly used and studied II/VI semiconductor materials due to its electron energy band structure with desirable band edges and direct band gap. CdS nanoparticles (NPs) are widely applied in different areas such as biosensing, antibacterial agents, photocatalytic hydrogen evolution, photoelectrochemical (PEC) energy conversion, and photovoltaic devices. Biosynthesis is an innovative, environmentally friendly route for the synthesis of CdS NPs. Specifically, bacterial precipitation of CdS NPs provides a simple, scalable production method. Our previous research shows that CdS NPs can be extracellularly precipitated with tunable CdS crystallite sizes ranging from 5 nm to over 15 nm in diameter. In this dissertation, I investigated the potential PEC application of bacterially precipitated CdS NPs and the engineering of their band structure. The results show that i) bacterially precipitated CdS NPs and their devices performed competitively when compared to chemical bath deposited (CBD) CdS NPs and their devices; ii) the performance difference is likely due to a layer of organic ligands that cap the bacterially precipitated CdS NPs and changed the carrier dynamics; and iii) the band structure of bacterially precipitated CdS NPs can be tuned by using different capping ligands. Collectively, my research demonstrates a promising approach for the biosynthetic precipitation of CdS NPS with tunable electronic properties and their application potential in photoelectrochemical devices.

# Contents

Abstract .....	iv
List of Tables .....	ix
List of Figures .....	x
Acknowledgements .....	xiii
1. Introduction .....	1
1.1 Current State of Knowledge.....	2
1.1.1 Biosynthesis of TM chalcogenide nanoparticles .....	3
1.1.2 Control over NP precipitation and properties .....	5
1.1.3 Energy applications of biosynthetic transition metal NPs .....	13
1.2 Significance.....	16
1.3 Specific Aims Summary.....	19
2. Characterization of biosynthetic cadmium sulfide nanoparticles and their photoelectrochemical (PEC) applications.....	25
2.1 Characterize the elemental composition, morphology, and optical activity of the bacterially precipitated CdS.....	26
2.1.1 Compositional and morphological properties characterizations .....	27
2.1.2 Optical properties characterizations.....	29
2.2 Photoelectrochemical properties of the BAC CdS NPs.....	33
2.2.1 EIS measurements .....	37
2.2.2 CV measurements .....	38
2.2.3 Transient photocurrent and the energy band structure.....	40

2.3 PEC applications of BAC CdS with reduced graphene oxide.....	43
2.3.1 Organic/inorganic photocharged capacitor electrode.....	45
3. Effect of cysteine passivation on the charge transport properties of BAC CdS and CBD CdS.....	51
3.1 Chemical synthesis of cysteine capped CdS NPs.....	55
3.1.1 Structural and compositional characterization of chemically synthesized cysteine capped CdS .....	55
3.1.2 Optical properties of chemically synthesized cysteine capped CdS .....	57
3.2 Effect of cysteine on charge carrier transport.....	58
4. Thiolate ligand modification of biosynthetic CdS NPs and control of their band structure .....	66
4.1 Biosynthesis of CdS NPs modified with different ligands using bacterial precipitation .....	66
4.1.1 Approach .....	67
4.1.2 Results .....	68
4.2 Cysteine used as an organic ligand improves the biosynthetic CdS yield.....	72
4.3 Organic ligands tune the band structure of biosynthesized CdS .....	74
5. Conclusions.....	82
5.1 Summary.....	82
5.2 Future work.....	84
Appendix A: Experimental Details.....	87
A.1 Sample preparation methods.....	87
A.1.1 CdS precipitation.....	87

A.1.2 Bacterially precipitated CdS nanoparticle (BAC CdS NP) electrode preparation.....	88
A.1.3 Bacterially precipitated non-cysteine CdS NP preparation .....	88
A.1.4 Chemically synthesized cysteine capped CdS NP preparation.....	89
A.1.5 Chemically synthesized non-cysteine CdS NP preparation .....	90
A.1.6 Bacterially precipitated CdS NPs with different ligands.....	90
A.1.7 Hybrid electrode assembly .....	91
A.1.8 Chemically synthesized CdS NPs passivated with different ligands.....	92
A.1.9 Electrochemical atomic layer deposition (EALD) CdS thin film preparation .	93
A.2 Characterization Methods.....	94
A.2.1 Scanning electron microscopy (SEM)/Electron dispersive X-ray spectroscopy (EDX).....	94
A.2.2 Transmission electron microscopy (TEM) .....	95
A.2.3 X-ray diffraction (XRD) analysis .....	95
A.2.4 UV-vis spectroscopy .....	96
A.2.5 Methyl orange (MO) molecule photodegradation. ....	96
A.2.6 Electrochemical measurements .....	97
A.2.7 Electrochemical measurements of the hybrid electrode .....	99
A.2.8 Photoluminescence (PL) spectra measurements.....	99
A.2.9 Time resolved PL (TRPL) measurements .....	100
A.2.10 X-ray Photoelectron Spectroscopy measurements (including the cut-off energy measurement) .....	100
A.2.11 Bacterially precipitation of CdS yield measurement.....	101

A.2.12 Cell viability measurements .....	101
A.2.13 Kelvin-Probe Force Microscopy (KPFM) for work function measurement .	102
A.3 Data analysis processes .....	103
A.3.1 XRD data analysis .....	103
A.3.2 EDS data analysis .....	103
A.3.3 UV-vis data analysis .....	104
A.3.4 TEM data analysis .....	104
A.3.5 XPS data analysis.....	104
A.3.6 Electrochemical data analysis.....	105
A.3.7 PL/TRPL data analysis.....	106
A.3.8 KPFM data analysis .....	106
Appendix B: Supplementary information .....	107
B.1 Tauc plots for the determination of the CdS bandgap.....	107
B.2 equivalent circuit of the BAC CdS.....	108
B.3 the estimation of band bending .....	109
B.4 CBD CdS cannot be made into the hybrid device due to the poor dispersity.....	110
B.5 Cd and S atomic ratio from XPS survey scans.....	111
B.6 The relationship between dipole moments and ionization energy for polarized ligand capped CdS NPs.....	111
B.7 Tauc plots for bandgap fitting for CdS with different ligands .....	112
Bibliography .....	113
Biography.....	125

## List of Tables

Table 1: Synthesis methods for CdS .....	17
Table 2: Four CdS NP groups prepared to study the effect of cysteine as the capping ligand .....	53
Table 3: The flat band potential and photovoltage measurement results.....	58
Table 4: d-spacing measured from HRTEM images in comparison with calculated values .....	70
Table 5: Work function, Fermi level to VBM energy difference, and bandgap of Ctrl, Cys, CysM, MP, and MHA CdS samples .....	81

## List of Figures

Figure 1: Overview of the three main research areas for biosynthetic TM chalcogenide NPs. ....	3
Figure 2: Biosynthesis optimization and control. ....	12
Figure 3: Energy applications of biosynthetic TM chalcogenide NPs. ....	14
Figure 4: Schematic showing the mechanism of CdS precipitation using <i>E. coli</i> . ....	18
Figure 5: The schematics of the PEC/energy storage device that is made of bacterially precipitated CdS NPs. ....	21
Figure 6: Schematic showing biosynthetic CdS NPs modified by a series of ligands and the effect of ligands on the band edges. ....	24
Figure 7: SEM and EDS mapping results of the BAC CdS NPs cross section. ....	27
Figure 8: TEM images of BAC CdS NPs under different magnifications. ....	28
Figure 9: XRD spectrum (light gray curve) and its fitting curve (red) by the Origin Lab. ....	29
Figure 10: UV-vis absorbance result of bacterially precipitated CdS NPs. ....	31
Figure 11: Photocatalytic degradations of MO for CdS NPs. ....	33
Figure 12: Experimental set-up used for measuring the transient photocurrent response of bacterially synthesized CdS NPs. ....	35
Figure 13: the Mott-Schottky plot of the BAC CdS NPs. ....	38
Figure 14: The CV curves and the energy band structure of BAC CdS. ....	40
Figure 15: Transient current measurements. ....	42
Figure 16: Comparison of FT-IR spectra of BAC CdS and CBD CdS NPs. ....	42
Figure 17: The schematics showing the multi-layer structures and band diagrams of the hybrid electrode and the simple electrode. ....	45

Figure 18: The transient current generated by the CdS-PVA-RGO hybrid electrode and by a BAC CdS NP electrode without PVA and RGO. ....	46
Figure 19: The Mott-Schottky plot of the CdS-PVA-RGO hybrid electrode.....	47
Figure 20: CV curves of the simple electrode and hybrid electrode.....	48
Figure 21: the OCP measurement of the hybrid and simple electrode. ....	50
Figure 22: Structural and compositional characterization of chemically synthesized CdS NPs.....	56
Figure 23: Fluorescence effect and optical measurements of cysteine capped CdS NPs..	57
Figure 24: Mott-Schottky (MS) plot of CdS NPs presented in Table 2. ....	59
Figure 25: Open circuit potential of CdS NP thin films.....	61
Figure 26: Photoluminescence measurements of the BAC CdS NPs and BAC(-cys) CdS NPs.....	62
Figure 27: TRPL spectra Cys CdS (blue) and CBD CdS (red) measurements at 670 nm emission wavelength. ....	63
Figure 28: Nyquist plots of CdS from EIS measurements.....	64
Figure 29: Biosynthetic CdS NP synthesis protocols. ....	67
Figure 30: HR-TEM images of biosynthetic CdS NPs modified with different ligands. ..	69
Figure 31: Region scan of XPS spectra of biosynthetic CdS modified with different ligands. ....	71
Figure 32: The mass of precipitation. ....	73
Figure 33: Cell viability testing. ....	74
Figure 34: AFM images of biosynthetic ligand modified CdS NPs. ....	77
Figure 35: Work function of different CdS NPs.....	77

Figure 36: Band edge tuning of biosynthetic CdS NPs precipitated with ligands and chemically synthesized CdS. .... 80

Figure 37: Schematic showing the proposed ligand passivation effect of the EALD CdS thin film. .... 86

## Acknowledgements

I want to heartily thank the following organizations and individuals on the path of getting my doctorate degree:

The Office of Naval Research, who funded the research.

The Zauscher Lab, (P.I., Prof. Stefan Zauscher),

The Nanomaterials and Thin Film Lab (P.I., Prof. Jeffrey Glass),

The Laboratory of Biological Networks (P.I., Prof. Lingchong You),

and the Mikkelsen Lab (P.I., Prof. Maiken Mikkelsen).

Furthermore, I would like to thank Prof. David Mitzi, Prof. Volker Blum, Dr. Katherine Marusak, Dr. Edgard Ngaboyamaniha, Dr. Jiani Huang, Dr. Carolyn Zhang, Dr. Isvar Cordova, Dr. Yangxiaolu Cao, Prof. Maria Luisa Sartorelli for fruitful discussions.

And finally I would like to thank the people helped me in this period of life: my mom Fen Xu, my dad Yongguo Feng, Prof. Stefan Zauscher, Prof. Jeffrey Glass, Prof. Lingchong You, my labmates Katherine Marusak, Luis Navarro, Daniel French, Lei Tang, Qing Tu, Rempeng Gu, Tejank Shah, Yicheng Zhao, Yunqi Yang, my roommates Yunchen Pu and Qiongcheng Xu, my supportive friends Nicholas Czarneck, Manu Lakshmanan, Zhiping Mao, Matthew Tedesco, Serene Hu, Favio Osorio, Anthony Gregorio, Vishwa Nellore, Weston Ross, Joshua Waite, Elisa Peterson, Jordan Churchill,

Joseph Lidowski, Ryan Hurley, Cory Nanni, Kevin Campell, Maxine Lee, Huijuan Li  
and Wenyuan Wang.

# 1. Introduction

Transition metals (TM), such as cadmium, lead, zinc, and manganese, form chalcogenide compounds with oxides, sulfides, selenides, and tellurides. Among these, TM chalcogenide nanoparticles (NPs) are intensively studied due to their promising optoelectronic and catalytic properties, namely their adjustable, direct bandgap arising from quantum confinement effects, and their adjustable electron transport properties that can be manipulated through doping.[1-3] Thus, TM chalcogenide NPs can be found in many applications in the chemical industry, environmental remediation, and in energy conversion. [4-6]

The myriad of applications of TM chalcogenide NPs also entail a range of methods for their synthesis. Chemical syntheses are traditional methods to fabricate TM chalcogenide NPs and offer good control over material structure and optoelectronic properties, resulting in excellent performance characteristics. [7, 8] However, as the benefits of “green fabrication,” such as low energy consumption and low toxic waste burden, become increasingly more important, the precipitation of TM chalcogenides using microorganisms or enzymes under ambient conditions is gaining increasing attention.

## **1.1 Current State of Knowledge<sup>1</sup>**

Since cadmium sulfide (CdS) was first precipitated by yeast in 1989, many different microorganisms have been harnessed for the synthesis of a broad range of TM chalcogenides. [9-16] However, to date a comprehensive comparison of NP size and distribution, NP properties, and NP applications across the various biosynthetic approaches is missing. In this section we briefly review the precipitation of TM chalcogenides by yeast, bacteria, fungi, and plant extracts, and focus on the control and optimization of these precipitation processes (Figure 1). Furthermore, we provide a critical discussion of the applications of the resulting TM chalcogenide materials.

---

<sup>1</sup> The following content is adapted from an article “Y. Feng, K. Marusak, L. You, S. Zauscher, “Biosynthetic Transition Metal Chalcogenide Semiconductor Nanoparticles: Progress in Synthesis, Property Control and Applications”, *Current Opinion in Colloid & Interface Science*, 2018, 38, 190” Yaying Feng structured the paper, wrote the manuscript, and was involved in revision.

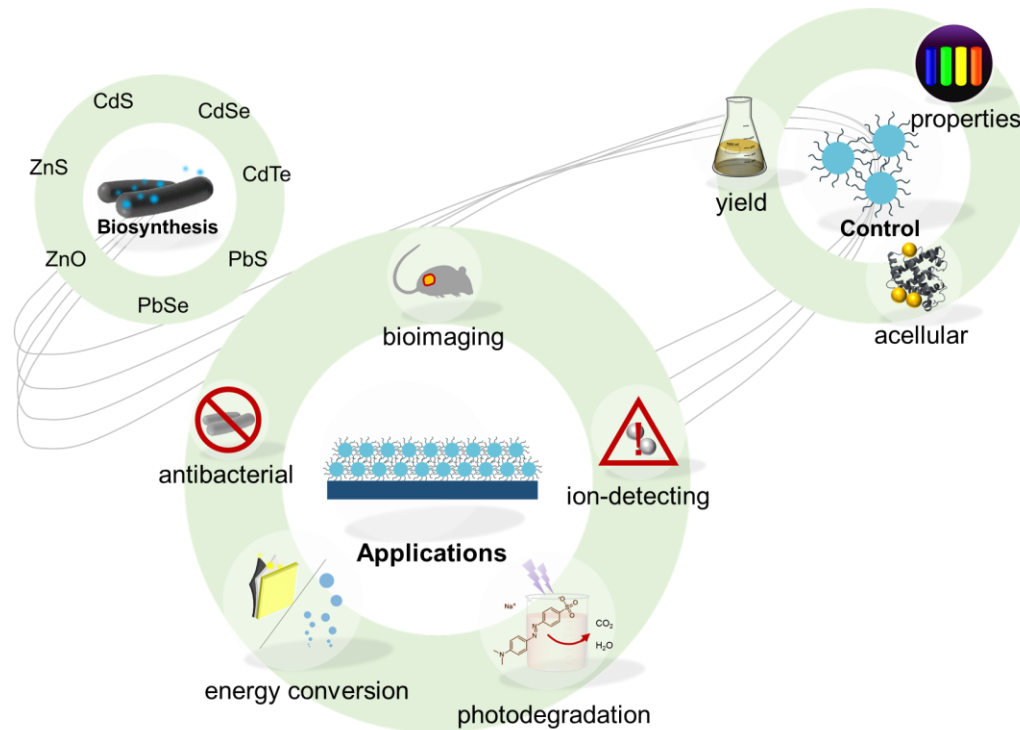


**Figure 1:** Overview of the three main research areas for biosynthetic TM chalcogenide NPs discussed in this review: biosynthesis, control over precipitation and material properties, and applications.

### 1.1.1 Biosynthesis of TM chalcogenide nanoparticles

In this section, we briefly discuss some of the milestone biosynthetic approaches for the fabrication of TM chalcogenide semiconductors, including cadmium sulfide (CdS), cadmium telluride (CdTe), zinc sulfide (ZnS), and silver sulfide (Ag<sub>2</sub>S), by yeasts, bacteria, fungi, algae, worms, and by plant extracts and enzymes. In-depth reviews on the biosynthesis of TM chalcogenide NPs are available in the literature. [9-18]

### **Yeast, worms and fungi**

The biosynthesis of semiconducting quantum dots (QDs) using yeast was first reported by Dameron *et al.* in 1989. [19] In 2012, Stürzenbaum *et al.* reported that an earthworm's metal detoxification pathway could be used to produce CdTe QDs. Additionally, they found that these QDs can be used in cell imaging applications. [20] In 2013, Syed *et al.*, produced CdTe QDs by using fungi by suspending the mycelium in a solution containing CdCl<sub>2</sub> and TeCl<sub>4</sub>. [21]

### **Bacteria**

In 2001, Wang *et al.*, engineered *Escherichia coli* (*E. coli*) to express cysteine desulfhydrase which enabled the bacteria to generate hydrogen sulfide aerobically. They then used these bacteria for heavy metal remediation by precipitating CdS from Cd<sup>2+</sup> contaminated water. [22] In 2004, Sweeney *et al.* discovered that natural bacteria have the capacity to precipitate CdS quantum dots in the range of 2–5 nm. To this end they added Cd<sup>2+</sup> to *E.coli* cultures which bound the toxic Cd<sup>2+</sup> into a Cd-thiolate complex, thus neutralizing Cd's toxicity. The Cd complex then reacted with added sulfide ions (Na<sub>2</sub>S) to form intracellular CdS NPs. [23]

Another transition metal semiconductor is Ag<sub>2</sub>S, which has a narrow bandgap (~1 eV) and good chemical stability. In 2011, Suresh *et al.*, reported the first case of biosynthesis of Ag<sub>2</sub>S NPs (4–14 nm) using *Shewanella oneidensis* (*S. oneidensis*). [24] In 2018, Choi *et al.* demonstrated the power of genetically engineered bacteria (*E. coli*) for

the biosynthesis of a broad range single and multi-element nanomaterials, including TM chalcogenide NPs.[25] Compared with other microorganisms, bacteria offer a versatile precipitation platform due to the intensive study of bacterial engineering.[25] Thus, here we harness bacterial precipitation systems for the production of CdS NPs.

### **1.1.2 Control over NP precipitation and properties**

With the emergence of biosynthetic TM chalcogenide precipitation approaches, research focus has recently shifted towards optimization and control over these processes to improve NP yield, to tune NP properties, and to increase NP purity. In the following, we address each of these areas in more detail.

#### **Improving NP yield**

Low NP yield is a major obstacle that limits the biosynthetic production of TM chalcogenide NPs. To improve yield, researchers have mainly applied three strategies: i) choosing/engineering efficient microorganisms, ii) inducing precipitation at an optimal growth stage, and iii) using phosphates to enhance metal ion uptake.

The mechanisms by which different, natural bacterial strains (*i.e.*, not genetically modified) affect TM chalcogenide NP precipitation are still largely unclear. However, recent studies on bacterial CdS biosynthesis [23, 26] showed that it is critical to select the correct bacterial strain to precipitate CdS NPs at appreciable yields (Figure 2a). Here, synthetic biology provides an exciting means to increase TM NP yield and to exert control over the precipitation reaction. For example, in 2007, Kang *et al.*, inserted the

phytochelatin synthase (SpPCS) gene from the yeast *S.pombe* into *E. coli* to promote CdCl<sub>2</sub> precursor intake and to thus increase NP yield. [27]

Sweeney *et al.*, studied CdS NP precipitation at different phases of bacterial growth and showed that the stationary phase of bacterial growth was the most productive in terms of CdS NP precipitation. [23] They attributed the increased yield to the large amount of reduced thiols available during the stationary growth phase. In another study, Al-Shalabi *et al.* used cells extracted from hairy tomato roots to study Cd<sup>2+</sup> uptake at different stages of cell growth and its effect on CdS precipitation. They found that while the addition of Cd<sup>2+</sup> in the early growth stage hinders cell growth, addition during mid and late growth stages does not significantly affect cell growth. Furthermore, they showed that changing the medium during the mid-growth phase increases Cd<sup>2+</sup> uptake 2-fold (Figure 2b). [28]

As for phosphate's influence on precipitation, Venegas *et al.*, reported in 2017 that the addition of inorganic phosphate to *E. coli* can increase H<sub>2</sub>S generation, thus increasing CdS yield. [29] In 2018 Ulloa *et al.* also reported that judicious phosphate addition increase CdS yield. They proposed that increased, extracellular concentration of PO<sub>4</sub><sup>2-</sup> leads to the formation of CdPO<sub>4</sub>, which is better tolerated by the bacterial cells and thus effectively increases Cd uptake. (Figure 2c) [30] Similarly, Liu *et al.*, reported in 2015 that the concentration of PO<sub>4</sub><sup>3-</sup> influences the formation of MnS. However, high PO<sub>4</sub><sup>3-</sup> concentrations will also trigger a reaction that forms undesirable Mn<sub>3</sub>(PO<sub>4</sub>)<sub>2</sub>

precipitation. Thus, the authors determined an optimum  $\text{PO}_4^{3-}$  concentration in their system to maximize MnS NP yield. [31]

In summary, to improve the particle yield is still an important area of research as it is one of the major barriers to for production scale-up and for particle purification. In Chapter 3 (Specific Aim 2.2) we investigated a new method that improves the bacterial precipitation yield of CdS NPs.

### **Controlling NP properties**

With the emergence of a broad range of biosynthetic NP precipitation approaches, there also has been a growing interest in controlling these approaches to affect NP properties. Most strategies to date focus on controlling the particle size, which has large impact on the photoelectronic properties of TM NPs. Already in 1989, when Dameron *et al.* first precipitated CdS with yeast, they influenced particle size by using different peptide-Cd complexes as precursors, which effectively limited CdS crystallite growth. [19] Recently, Kaviya *et al.* reported that dimethyl sulfoxide (DMSO), an aprotic solvent, can be used to disrupt NP aggregation and growth, which was detected by a blue shift in the fluorescence spectrum. [32] Perhaps the simplest way to influence NP size is to control precipitation or incubation time. In 2010, Bao *et al.* showed that the size of extracellularly precipitated CdTe NPs increased predictably with increasing incubation time. [33] In 2013, Fellowes *et al.* showed a similar behavior for CdSe NPs when prolonging the refluxing time. [34] Gallardo *et al.* in 2014, [35] and Yang *et al.* in

2015, [36] reported that the NP size and thus the CdS fluorescence emission wavelength could be tuned by controlling the precipitation time when using bacterial precipitation systems (Figure 2d).

The size-induced quantum confinement effect of biosynthetic CdS QDs was studied in 2016 in our lab. [37] Specifically, we studied the effect of reactant concentrations on the size and thus bandgap of bacterially precipitated CdS NPs. Transmission electron microscopy and UV-visible absorption measurements showed that the average particle size could be tuned from 3.5–15 nm by controlling the concentrations of the CdCl<sub>2</sub> and cysteine precursors (Figure 2e). Since the range of crystallite dimensions fell in the range of sizes of QDs, the bandgap of the crystallites changed correspondingly. Furthermore, by timing the CdCl<sub>2</sub> addition in the bacterial growth process we were able to control the precipitation location (intra-/pericellular *vs.* extracellular). Specifically we found that adding CdCl<sub>2</sub> at the early stage of bacterial growth leads to predominantly intracellular precipitation, while adding CdCl<sub>2</sub> close to the end of the logarithmic growth stage resulted in extracellular precipitation. [37]

In addition to tuning NP size, controlling the particle size distribution is important. Already in 2007, Kang *et al.* showed that CdS NPs had a narrow size distribution when they were precipitated by *E. coli* that were genetically engineered to express phytochelatins (PCs). It is thought that the PCs trap Cd<sup>2+</sup> in form of a PC-Cd complex which is less toxic to bacteria, leading to more uniform NP sizes. [27] CdTe

QDs produced by Bao *et al.* in 2010 using an extra cellular method, had a narrower size distribution than that of hydrothermally synthesized CdTe QDs. [33]

To further improve precipitation control and particle size distribution, extra cellular and cell free biosynthesis approaches are emerging. For example, in 2010, Bao *et al.* reported an extracellular method for the one-step preparation of CdTe QDs with tunable fluorescence properties. This approach relied on the presence of proteins secreted by *E. coli*. [33] More recently, Dunleavy *et al.* in 2016 reported the cell-free CdS precipitation using an enzyme (Cystathionine  $\gamma$ -lyases (CSEs)) (Figure 2f). In this cell-free, enzymatic precipitation approach, Dunleavy *et al.* were able to control the particle size and the corresponding photoluminescence (PL) emission by controlling the incubation time and the H<sub>2</sub>S concentration. Notably they found an equivalency between reaction time and cysteine (H<sub>2</sub>S precursor) concentration; *i.e.*, NPs precipitated at high cysteine concentrations and short reaction times were of equal size as those precipitated at low cysteine concentrations and long reaction times. [38] In 2017, Ansary *et al.* used the NADPH dependent-Nitrate reductase, expressed by the fungus *Fusarium oxysporum* (*F. oxysporum*), to precipitate narrowly size dispersed CdSe NPs. Furthermore, they showed that the precipitated NPs are capped by ( $\gamma$ -Glu-Cys-Glu-Cys)-Gly, a synthetic peptide that was added to the reaction mixture. The presence of this peptide facilitated the conjugation of the NPs with other biomolecules. [39] In an alternate approach Murray *et al.* showed in 2017 that ZnS NPs could be produced by reacting Zn<sup>2+</sup> with

biogenerated H<sub>2</sub>S gas. In this approach, sulfate-reducing bacteria (*Desulfovibrio desulfuricans*, NCIMB 8307) were grown to produce H<sub>2</sub>S gas, which was then collected from the top of the culture container, and finally injected into a Zn<sup>2+</sup>-containing solution to form ZnS NPs. These NPs had a diameter of ~2.4 nm with a cubic crystal structure. [40]

Other than controlling the particle size and the corresponding fluorescence properties, scientists also attempt to control NP crystal structure. For example, Moon *et al.* reported in 2013 that by using two different sulfur sources (*i.e.*, thiosulfate and cysteine) in an extra cellular bacterial precipitation system, two different crystal structures (hexagonal and cubic, respectively) form. Furthermore, they discovered as the NPs begin to recrystallize and grow in size with increasing incubation time that the crystal structure changes from cubic to a more stable cubic/hexagonal mixture. [41] In 2015, Rangel-Chavez *et al.* used a bacterial precipitation system (*Desulfovibrio alaskensis* 6SR bacteria) to study the relationship between the cadmium concentration and crystal structure. They found that the higher the Cd<sup>2+</sup> concentration the higher was the percentage of cubic crystal structure in the mixture. [42] Finally, in 2016 Fuku *et al.* reported that thermal annealing improves the crystallinity and changes the electron kinetics of bacterially precipitated ZnO NPs without changing their size. Furthermore, using PL measurements showed that after annealing the emission peak of the ZnO particles blue-shifted by 70 nm, indicating an increase in the bandgap. [43]

As seen from this summary, a growing number of strategies is becoming available to optimize biosynthetic precipitation methods and to control NP properties. In Chapter 4 (Section 4.3) we investigate a new approach to control the properties of CdS NPs, specifically, we use thiolate ligands to tune the band structure of biosynthetic CdS NPs.

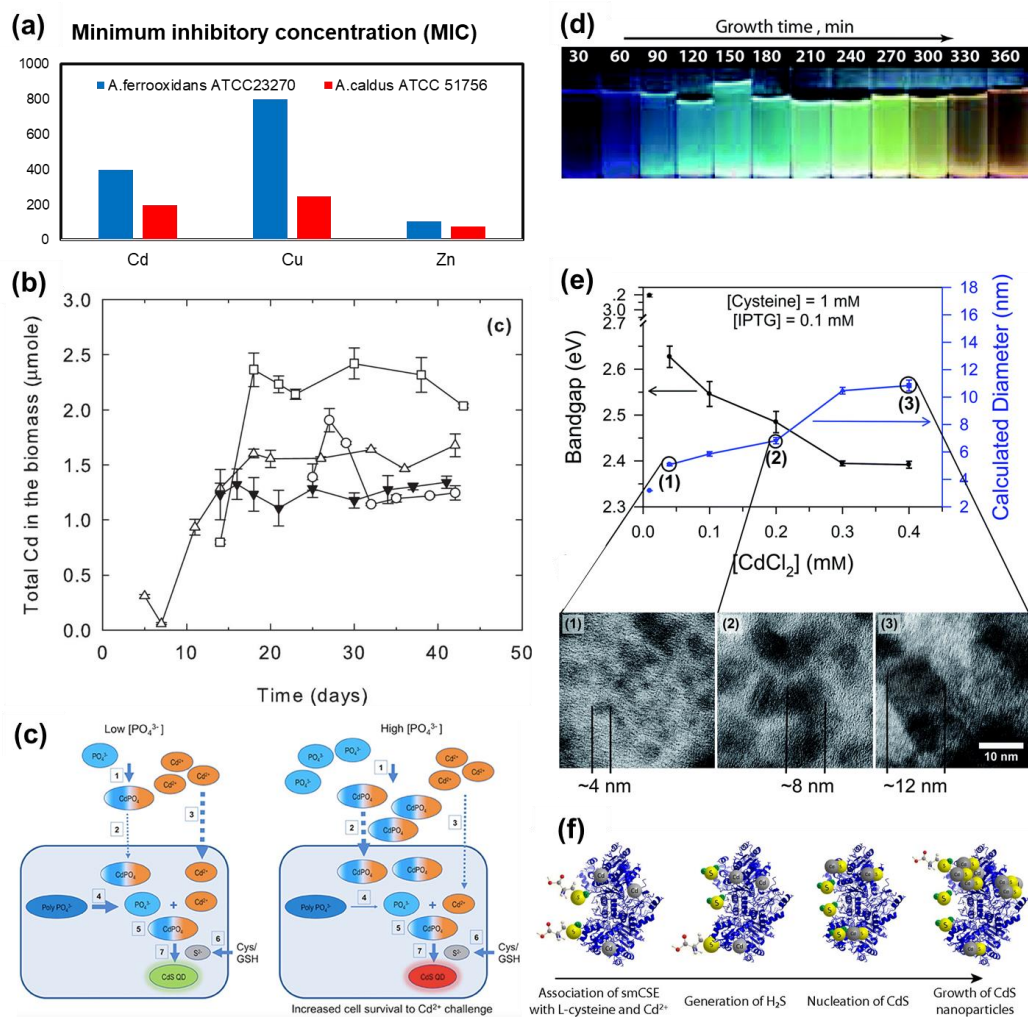


**Figure 2:** Biosynthesis optimization and control. (a) Difference in ion tolerance (Cd, Cu, and Zn) between *A. ferrooxidans* and *A. caldus*. (b) Cd uptake by tomato hairy root at different growth stages.  $\Delta$ : Cd added 5 days after inoculation;  $\blacktriangledown$ : Cd added 14 days after inoculation;  $\square$ : Cd added 14 days after inoculation and replaced the medium;  $\circ$ : Cd added 25 days after inoculation. (c) Schematic of  $\text{PO}_4^{3-}$  enhancing  $\text{Cd}^{2+}$  uptake by bacteria. (d) Wide wavelength range of fluorescence emission of bacterially precipitated CdS NPs that are incubated for different times. (e) Bacterially precipitated CdS NP size and corresponding bandgap are controlled by adjusting  $\text{CdCl}_2$  precursor concentration in the cell culture. (f) Schematic of enzymatic precipitation of CdS NPs. Images are adapted or reprinted with permission for Figure 2(a) [26], Figure 2(b) [28], Figure 2(c) [30], Figure 2(d) [36], Figure 2(e) [37], and Figure 2(f) [38], copyright 2016 Elsevier, 2014 Elsevier, © 2018 Ulloa, Quezada, Araneda, Escobar, Fuentes, Álvarez, Castro, Bruna, Espinoza-González, Bravo and Pérez-Donoso (Frontiers in Microbiology), 2015 Royal

Society of Chemistry, 2016 Royal Society of Chemistry, and 2016 National Academy of Sciences, respectively.

### 1.1.3 Energy applications of biosynthetic transition metal NPs

TM chalcogenide NPs are wide bandgap semiconductors and their photoexcitation creates electron-hole pairs that can be collected to generate photocurrent or that can be used to trigger hydrogen and oxygen evolution reactions. Thus, these biosynthetic materials offer exciting opportunities for photovoltaic (PV) and hydrogen/oxygen evolution (HER/OER).

The first example of a PV application using biosynthetic TM NPs was reported in 2016 by Spangler *et al.*, who used an engineered strain of *Stenotrophomonas maltophilia* to precipitate PbS-CdS core shell NPs. [44] They then fabricated a prototype dye-sensitized solar cell in which they used these NPs to sensitize the TiO<sub>2</sub> absorber layer (Figure 3a).

Wang *et al.*, in 2017, harnessed bacterially precipitated CdS nanoparticles for a HER application. Specifically, they constructed a whole cell *E.coli*-CdS hybrid system and used the endogenous bacterial [Ni-Fe]-hydrogenase to enhance hydrogen production. By comparing the hydrogen evolution efficiency of bacterial cells, of the isolated biosynthetic CdS NPs, and of the whole cell hybrid system, the authors found that the hybrid system generated the largest amount of hydrogen. They attributed the enhanced performance to both the higher performance of the biosynthesized CdS and the efficient electron transfer between CdS and the cells. Additionally, the authors proposed a mechanism in which photogenerated electrons from CdS catalyze intracellular hydrogen generation. In this mechanism, intracellular glucose serves as the energy source, producing pyruvate, a key reactant for intracellular hydrogen generation, (Figure 3b). [45] In 2018, Wei *et al.*, used bacterially precipitated CdS and *E.coli* bacteria

to build another hybrid hydrogen generation system. The authors used genetically engineered *E.coli* cells to display the OmpA-PbrR protein on their surfaces, and then used this protein to bind CdS to the outer cell surfaces. To generate hydrogen, ascorbic acid was added as the electron donor to reduce oxidized CdS, while methylviologen ( $MV^{2+}$ ), a redox dye, was added as the electron mediator. [46] In 2016, Sakimoto *et al.* harnessed bacteria (*M. thermoacetica*) to synthesize CdS NPs and then used the bacteria-cell hybrid system to photosynthesize acetic acid and oxygen by reducing carbon dioxide. This example shows the potential of biosynthetic NPs to enhance solar to chemical conversion that can be applied in fuel cells. [47, 48]

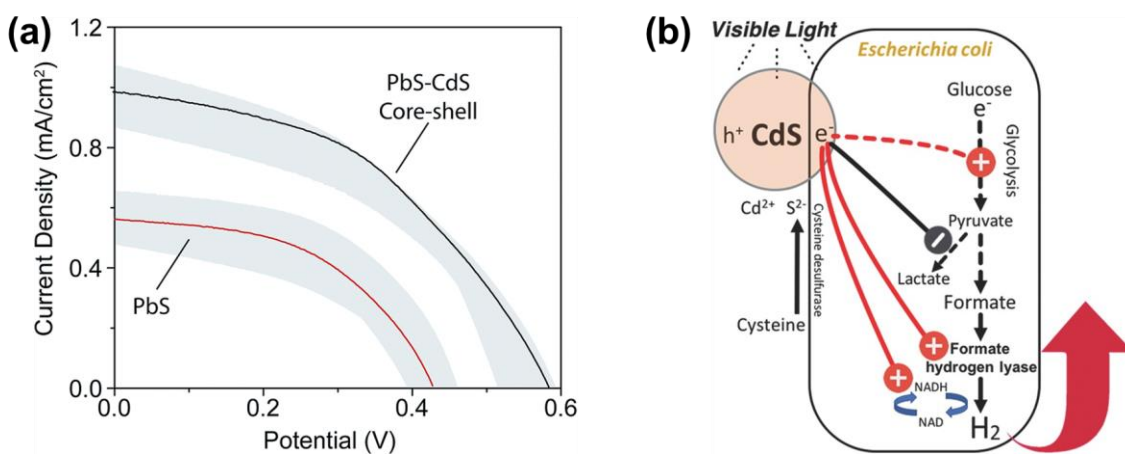


**Figure 3:** Energy applications of biosynthetic TM chalcogenide NPs. **(a)** I-V curves show that biosynthetic PbS-CdS core-shell NPs outperform biosynthetic PbS NPs in a prototype dye sensitized solar cell. **(b)** Schematic showing the hydrogen evolution pathway of a CdS-*E.coli* hybrid system. Images are reprinted with permission for Figure 4(a), [44] Figure 4(b), [45] copyright 2016 Royal Society of Chemistry, and 2017 John Wiley and Sons, respectively.

As biosynthetic CdS NPs promise interesting opportunities for energy conversion applications, we investigated the photoelectrochemical properties and application of bacterially precipitated CdS NPs in Chapter 2 (Section 2.3).

At the current stage, biosynthetic methods still need to overcome several limitations. Such as restrictive precipitation environments that are compatible with growth of microorganisms and can sustain enzymatic reactions. Furthermore, biosynthetic methods are typically slow and produce particles of low purity compared with chemical bath deposition methods. While the purity of TM chalcogenide NPs is crucial for some applications, biosynthetic NPs can outperform their pure, chemically synthesized counterparts in other applications. For example, due to the natural presence of organic capping ligands, biosynthetic NPs can bind dye molecules or can bind to other materials, including cells and graphene. This makes them useful as efficient photocatalysts, as natural bioimaging tracers, and as photoabsorbers in energy devices. Furthermore, NP-cell hybrid systems can enhance the performance by combining functions of NPs and cell membranes to detect metal ions, or by combining NP function with intracellular metabolic pathways to enhance hydrogen evolution efficiency and photo-to-chemical conversion efficiency. Finally, advances in synthetic biology harness the programmable nature of bacteria to combine biosynthetic approaches with device fabrication, as recently demonstrated by insertion and expression of autonomous, pattern-forming gene circuits, leading to patterned devices. [49]

## **1.2 Significance**

The widespread use of CdS also entails a range of methods for the synthesis of CdS NPs and continuous films, including chemical bath deposition (CBD),[50-56] electrodeposition,[57-60] infrared pulsed laser deposition,[61-63] and a variety of physical deposition methods such as magnetron sputtering.[64-68] Among these synthesis methods, CBD is widely used because of its simplicity and controllability. However, CBD requires 60 °C to 80 °C precipitation temperature and generates byproducts that contain high concentrations of Cd<sup>2+</sup>, creating a negative impact on the environment.[69-73] Magnetron sputtering is a method particularly suitable to fabricate CdS thin films.[74-76] Although this method can produce high quality CdS thin films, the need for high vacuum and the magnetic field control increase the energy consumption during the fabrication process.[67] Compared with these traditional synthesis methods, biosynthetic methods for the precipitation of inorganic NPs are relatively new. Compared to CBD, the biosynthesis of CdS produces byproducts with lower [Cd<sup>2+</sup>], requires low (37 °C) temperatures, and ambient pressure (Table 1).[67, 69, 72, 77]

**Table 1: Synthesis methods for CdS**

	<b>Biosynthesis</b>	<b>Chemical Bathed Deposition</b>	<b>Magnetron Sputtering</b>
Temperature	~37 °C	60 °C – 80 °C	30 °C
Pressure	Atmosphere	Atmosphere	Vacuum
Toxic waste concentration	Potentially low	High	Low
Cost	Low	Low	High
Simple synthesis	No	Yes	No
Purification method	Hard	Easy	Easy

Research in our group has shown that genetically engineered *Escherichia coli* (*E. coli*) can be used to precipitate CdS NPs with tunable, photoelectronic properties, by overexpression of the cysteine desulfhydrase gene (Figure 4). Desulfhydrase degrades cysteine and aids in the production of hydrogen sulfide (H<sub>2</sub>S). H<sub>2</sub>S reacts with Cd<sup>2+</sup> added to the culture media which leads to the precipitation of CdS NPs.[78] We discovered that we can control the location of the precipitation (intracellularly *vs.* extracellularly), by timing the addition of the CdCl<sub>2</sub> precursor. Through manipulation of the precursor concentration we were able to control the CdS NP size which directly affects the band gap.[79]

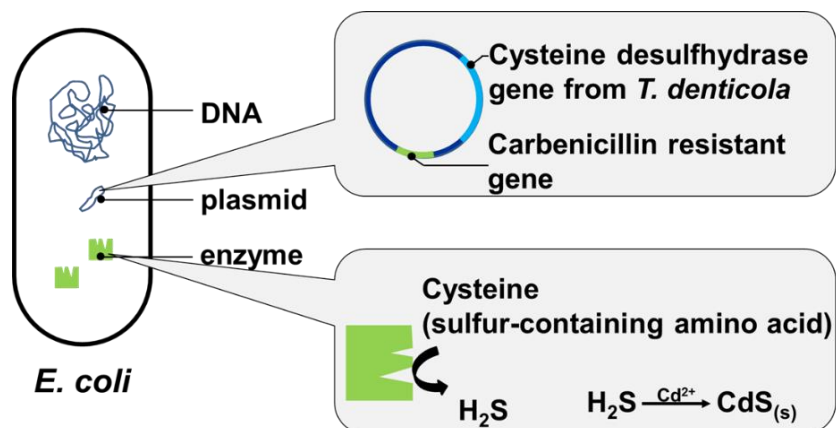


**Figure 4:** Schematic showing the mechanism of CdS precipitation using *E. coli*. By overexpressing the cysteine desulfhydrase gene in *E. coli*, a type of enzyme can be generated that break down cysteine and generate  $H_2S$ . The  $H_2S$  can react with  $Cd^{2+}$  to precipitate CdS NPs.

Although there is an abundance of research that studied the biosynthetic TM NP precipitation, there are surprisingly few studies that investigate the compositional, structural, optical, and electrochemical properties of these NPs. Deeper understanding of these properties is crucial for developing applications that involve biosynthetic TM semiconductor NPs.

Here, we systematically studied the compositional, structural, optical, and electrochemical properties of our bacterially precipitated CdS NPs and their performance in PEC applications. This work opens a new application direction of biosynthesized inorganic materials as building blocks for energy conversion and storage devices and proves the concept that the biosynthesized organic/inorganic hybrid materials have potential advantages in building energy devices because of the intimate

connection between inorganic crystallites and organic functional groups at material surfaces.

Furthermore, we build on the discovery that films of bacterially precipitated CdS nanoparticles exhibit i) carrier lifetimes that are substantially longer and exhibit ii) photocurrent densities that are higher compared to those in films prepared from unpassivated, chemically synthesized CdS nanoparticles. We hypothesize that these properties arise from passivation through cysteine which was added as the sulfur source in the bacterial precipitation process. Based on this hypothesis, we studied the effect of chemical ligands on the energy band structure of CdS NPs. By capping bacterially precipitated CdS NPs with different ligands, we showed that band edge position can be tuned, thus opening up a new method to control the electronic properties of biosynthetic CdS NPs.

### ***1.3 Specific Aims Summary***

**Specific Aim 1: Characterization of biosynthetic cadmium sulfide nanoparticles for PEC applications**

Specific Aim 1.1: Characterize the elemental composition, morphology, and optical activity of bacterially precipitated CdS NPs.

Rationale: The PEC performance of bacterially precipitated CdS NPs is determined by many factors, such as the NPs' morphology, crystal structure and size, and bandgap. Furthermore, the chemical environment may affect the NPs' surface

chemistry, and thus electron transport mechanisms and the charge carrier life time. This data has not been available to date.

Specific Aim 1.2: PEC properties of bacterially precipitated CdS NPs.

Rationale: As a semiconductor with a direct band gap of  $\sim 2.4$  eV, one important application of CdS is PEC hydrogen evolution. However, little is known about the PEC properties of bacterially precipitated CdS. Exploring the PEC properties of bac CdS NPs, will provide a deeper understanding of their energy band structure and thus be useful to guide the design of devices that use this material.

Specific Aim 1.3: Building a proof of concept PEC/energy storage device that uses BAC CdS NPs.

Rationale: Having completed a systematic study of the bacterially precipitated CdS NPs (SA1.1) and their PEC performance (SA1.2), we will explore the integration of CdS into an energy conversion and storage device to demonstrate the value of these biosynthetic materials for PEC applications. We recently discovered that compared to CBD CdS NPs, bacterially precipitated CdS NPs are more compatible with oxide glass substrates and poly-vinyl alcohol hydrogels. Harnessing the large surface area of graphene sheets, we propose to build an integrated energy-conversion and storage device that converts photoenergy with CdS and stores the energy with graphene. This is the first case study that applies the biosynthetic materials into a proof of concept energy

device, and it paves the way to further apply this material to other applications (Figure 5).[80]

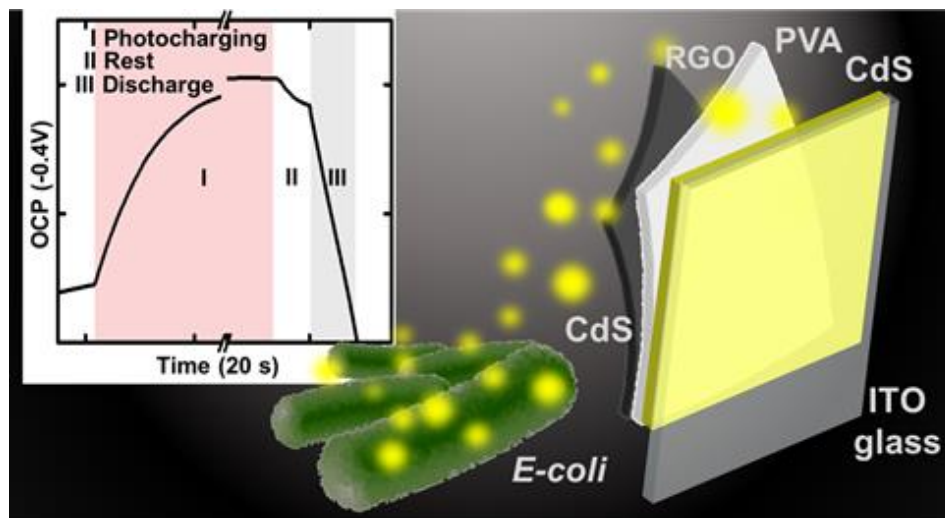


**Figure 5:** The schematics of the PEC/energy storage device that is made of bacterially precipitated CdS NPs. The inset shows its ability to be photocharged and store the electricity.

### **Specific Aim 2: Cysteine passivation effect of the BAC CdS and CBD CdS**

#### **Specific Aim 2.1: Chemical synthesis of cysteine capped CdS NPs**

Rationale: We hypothesized that BAC CdS NPs are likely capped by cysteine, *i.e.*, thiolate amino acids that are added to the cell culture as a precursor. To study the influence of the organic matrix, here cysteine, on BAC CdS NPs PEC performance, we study chemically precipitated cysteine capped CdS NPs as a model system. Thus, the first step is to confirm that we precipitated cysteine capped CdS NPs chemically.

Specific Aim 2.2: Effect of cysteine on charge carrier transport

Rationale: To understand the biosynthetic CdS NPs' PEC application, a better understanding of charge transport inside the material is necessary. This study will give us insights about how organic ligands change the carrier transport behavior, so that we can better control the electrochemical properties of the BAC CdS NPs for PEC applications.

**Specific Aim 3: Thiolate ligand modification of biosynthetic CdS NPs and control of their band structure**

Specific Aim 3.1: Demonstrate the bacterial biosynthesis of CdS NPs modified with different ligands

Rationale: To further improve the bacterial precipitation system's capability, we hypothesized that biosynthetic CdS NPs electronic properties can be tuned by modifying with different organic ligands. This is the first attempt of modifying biosynthetic transition metal chalcogenide NPs with ligands. First, we demonstrate that the bacterial precipitation system can produce CdS NPs modified with different ligands.

Specific Aim 3.2: Demonstrate that cysteine used as an organic ligand improves the biosynthetic CdS yield

Rationale: Since we modified the bacterial precipitation protocol, the precipitation process might be changed. As a result, we hypothesized that the yield of

CdS production is changed when precipitating with ligands. The change of yield provides economic effect of using biosystem for CdS production. In this section, we study cysteine's effect on improving CdS's yield.

Specific Aim 3.3: Demonstrate that organic ligands tune the band structure of biosynthesized CdS NPs

Rationale: We hypothesized that the energy band edge of biosynthetic CdS NPs is changed when modified with different organic ligands. The capability of band edge tuning will improve biosynthetic CdS NPs' compatibility to form desired heterojunction when partnering with other materials and thus improving photo to electric energy conversion efficiency. It is reported that ligand-modified PbS NPs are used to improve solar cells' efficiency due to the band edge tuning effect. Thus, we demonstrate that we can tune the band edge of biosynthetic CdS NPs for the first time.

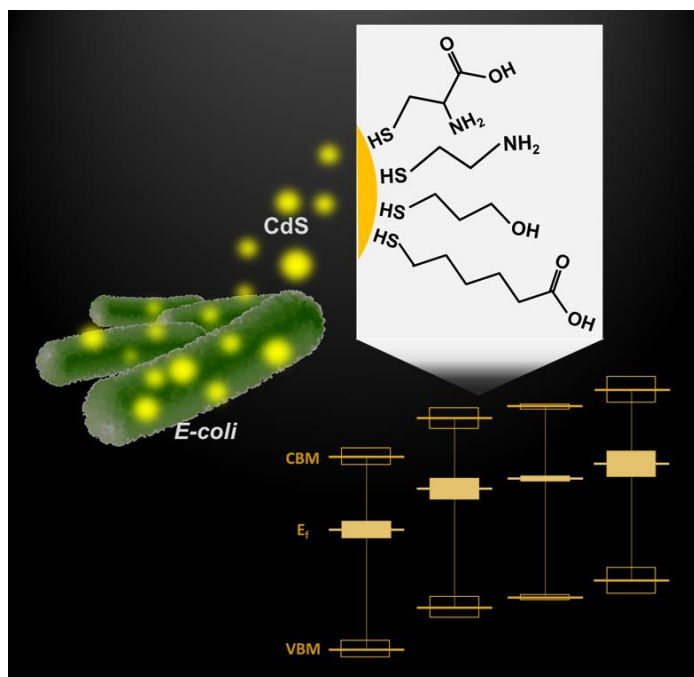


**Figure 6:** Schematic showing biosynthetic CdS NPs modified by a series of ligands and the effect of ligands on the band edges.

## 2. Characterization of biosynthetic cadmium sulfide nanoparticles and their photoelectrochemical (PEC) applications<sup>1</sup>

Although the biosynthesis of transition metal nanoparticles has been studied for about 20 years, the use of the bio-precipitated NPs for energy conversion/storage application, especially photoelectrochemical (PEC) devices, has rarely been studied due to a lack of systematic knowledge about the opto-electronic properties of these materials.[79, 80]

As a semiconductor material with direct band gap, cadmium sulfide (CdS) is widely used in photovoltaic (PV), photocatalytic, and PEC applications. Many factors influence the PEC performance of biosynthetic CdS nanoparticles (NPs). Internal factors such as composition, morphology (crystal structure), and external factors such as the particles' chemical environment, the NP thin film thickness, and the thin film substrate change the NPs' solar energy conversion efficiency. The objective of this specific aim is to i) quantitatively understand the compositional, morphological, and photoelectrochemical properties of bacterially precipitated CdS NPs (section 2.1), ii) prove the photoactivity of these biosynthetic nanoparticles (section 2.2), and iii) further

---

<sup>1</sup> The following content is adapted from an article "Y. Feng, E. Egaboyamahina, K. Marusak, Y. Cao, L. You, J. Glass, S. Zauscher, "Hybrid (organic/inorganic) electrode from bacterially precipitated CdS for PEC/storage applications", *The Journal of Physical Chemistry C*, 2017, 121, 7, 3734" Yaying Feng conducted experiments, wrote the manuscript, and was involved in designing experiments and manuscript revision.

apply them into a hybrid organic-inorganic energy conversion and storage device (section 2.3).

## **2.1 Characterize the elemental composition, morphology, and optical activity of the bacterially precipitated CdS**

Since bacterially precipitated CdS (BAC CdS) NPs are isolated from bacterial culture media, the composition, morphology, and properties of these NPs are likely different from those synthesized with traditional chemical methods, and likely will affect their PEC performance. As a semiconductor, CdS absorbs light and converts the photon energy into electric energy or chemical potential energy. Since the energy conversion properties of a semiconductor are mainly determined by the bandgap, the bandgap of the *E. coli* precipitated CdS NPs is investigated. Furthermore, to directly prove the photoactivity of these NPs, especially their potential for water decontamination applications, photodegradation studies of MO molecules are conducted, and the results are compared with CBD CdS.

We used Scanning Electronic Microscopy (SEM), Energy-dispersive X-ray spectroscopy (EDS), Transmission Electronic Microscopy (TEM), and X-ray diffraction measurements (XRD) to obtain the compositional and morphological, and crystal information. Furthermore, we use UV-vis spectroscopy to determine the bandgap of BAC CdS. Finally, we explore the BAC CdS catalyzed degradation rate of methyl orange (MO) in solution, using UV-vis spectroscopy.

### 2.1.1 Compositional and morphological properties characterizations

The SEM image of the cross-section of BAC CdS NPs on a silicon (Si) substrate shows that the film thickness is  $\sim 7$   $\mu\text{m}$  with a smooth surface (Figure 7a). The EDS elemental mappings of Cd, S, Si and carbon (C) indicate a homogeneous distribution of CdS and C throughout the thickness of the thin film (Figure 7b and c). The high C concentration might be caused by the organic compounds surrounding the CdS NPs.

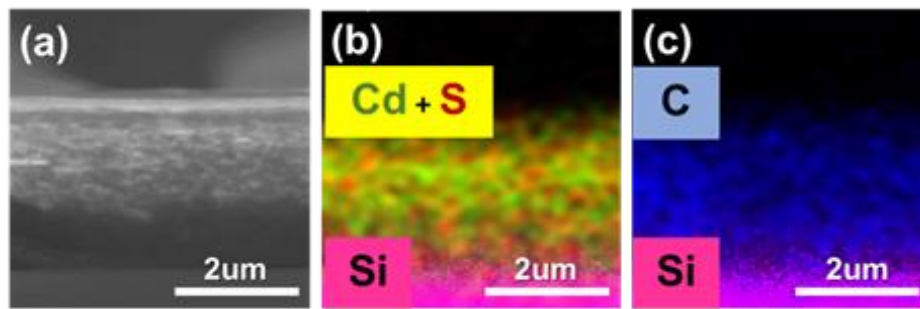


**Figure 7:** SEM and EDS mapping results of the BAC CdS NPs cross section. **(a)** SEM image of the cross section. **(b)** Cd, S, Si mapping result of the cross section. Red, green, and pink dots represent Cd, S, and Si, respectively. **(c)** C, Si mapping results of the cross section. Blue and pink dots represent C and Si respectively.

TEM images of the BAC CdS NPs are shown in Figure 8. Some CdS NPs are precipitated around *E.coli*, and some are outside of *E.Coli* (Figure 8a). The extracellularly precipitated NPs are embedded in an organic matrix (Figure 8b). A further zoomed in image shows that each NP is actually composed of smaller nanocrystals (Figure 8c), with a diameter of  $\sim 7$  nm (Figure 8d).

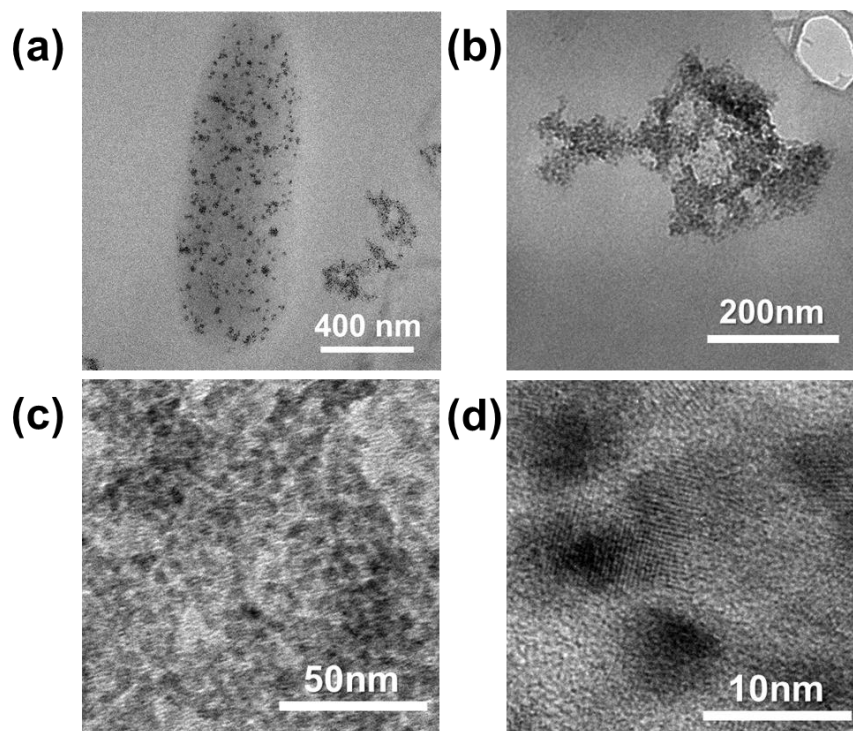


**Figure 8:** TEM images of BAC CdS NPs under different magnifications. **(a)** *E.coli* and CdS NPs. **(b)** CdS NPs are embedded into organic matrix. **(c)** CdS NPs are composed of smaller nanocrystals. **(d)** High resolution TEM image showing the crystal lattice of CdS nanocrystals. (Images credit: Dr. Katherine Marusak).

The XRD spectrum of BAC CdS NPs is shown in Figure 9, and can be fitted by four, distinct peaks. We found that the BAC CdS NPs consist of a mixture of face centered cubic (FCC) and hexagonal closed pack (HCP) crystal structures. The relatively large widths of the peaks in the spectrum are indicative of small crystal sizes,[81] in good agreement with the observations from the TEM images.

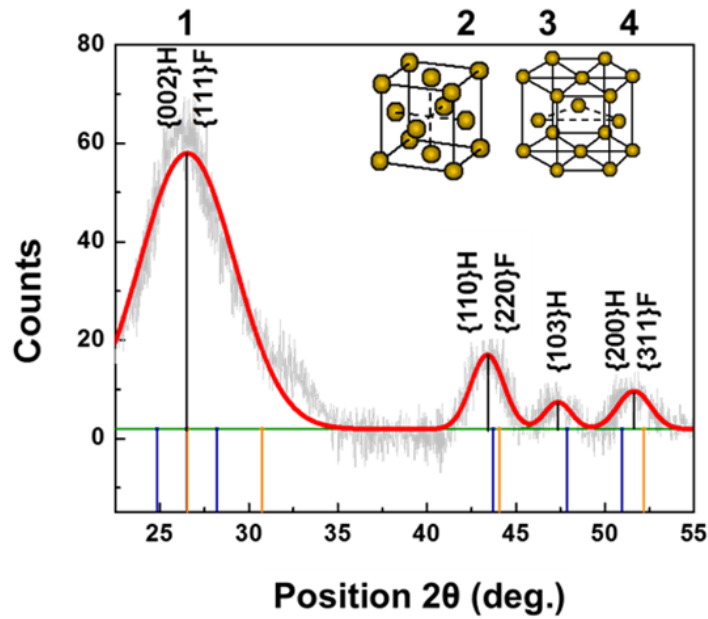


**Figure 9:** XRD spectrum (light gray curve) and its fitting curve (red) by the Origin Lab. Four peaks 1, 2, 3, and 4 are corresponding to CdS HCP and FCC feature signals in this range. Below the average line, the blue lines represent reference HCP 2θ positions (ref: 01-074-9663), while the yellow lines represent reference FCC 2θ positions (ref: 01-075-0581).

### 2.1.2 Optical properties characterizations

We measured UV-vis spectra to determine the band gap of BAC CdS NPs. The onset of the absorption is determined by linear extrapolation of the baseline and the absorption edge (Figure 10a). The intercept is then used in Planck's relation:

$$E_g = \frac{hc}{\lambda} , \quad \text{Equation 1}$$

where  $E_g$  is the band gap,  $h$  is Planck's constant,  $c$  is the speed of light in vacuum, and  $\lambda$  is the absorption edge's wavelength, which is used to determine the average band

gap energy. This band gap energy is then also used to calculate the crystallite size. Figure 10b shows that the absorption edge of the CdS NPs is around 483 nm, which, by the Planck relation, translates to a band gap of ~2.57 eV. This band gap value is close to the upper limit of ideal PEC materials.[82] It also agrees with the band gap that is calculated using the Tauc relation (Figure B.1). Furthermore, the crystalline size calculated from the band gap value is around 7 nm, using the following equation[83-85]:

$$E_g^* \cong E_g^{bulk} + \frac{\hbar^2 \pi^2}{2er^2} \left( \frac{1}{m_e m_0} + \frac{1}{m_h m_0} \right) - \frac{1.8e}{4\pi\epsilon\epsilon_0 r}, \quad \text{Equation 2}$$

where  $E_g^*$  is the measured bandgap of the nanocrystallites,  $E_g^{bulk}$  is the bandgap of the bulk material (for CdS it is 2.42 eV),  $m_e$  and  $m_h$  are 0.18 and 0.53, respectively, and  $\epsilon$  is 5.23.[86] The calculated crystal diameter is in good agreement with the TEM measurements shown in Figure 8d.

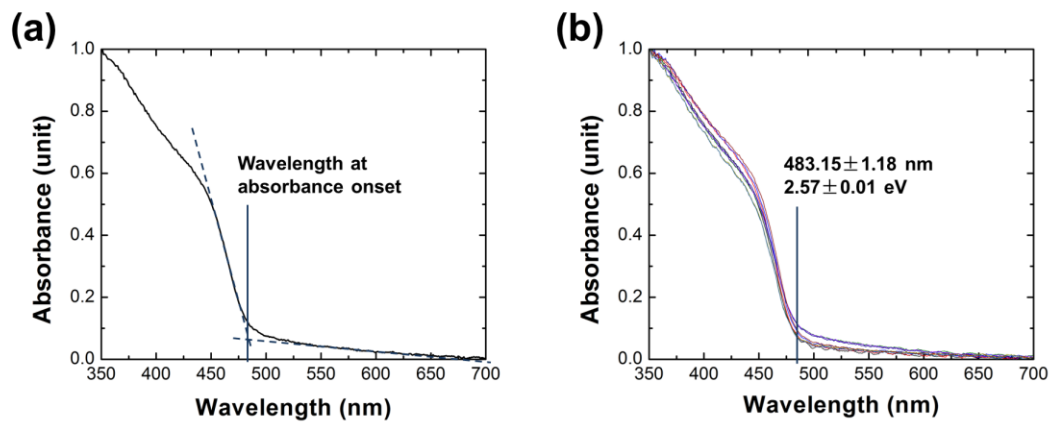


**Figure 10:** UV-vis absorbance result of bacterially precipitated CdS NPs. **(a)** The schematic of the determination method of the absorbance wavelength. **(b)** The average absorbance wavelength of such prepared CdS from multiple tests, and the corresponding bandgap calculated from the absorbance wavelength.

As pointed out in the Introduction section, CdS NPs could be applied in water and air decontamination. To demonstrate the functionality of the bacterially precipitated CdS NPs, their degradation performance for MO in water under sun light irradiation was characterized. The photodegradation experiment shows that the bacterially precipitated CdS NPs are photocatalytically active. Figure 11a shows the remaining MO concentration as a function of reaction time. The reaction was triggered by irradiation with simulated sun light. The blue, dotted-line shows the degradation rate of MO, catalyzed by the bacterially precipitated CdS NPs. The red diamond-line shows the degradation rate of MO catalyzed by same amount of CBD CdS NPs, and the black square-line, as control, shows the degradation rate of MO without any catalyst. It can be

seen that i) both the bacterially precipitated CdS and CBD CdS have photocatalytic property, and ii) the CBD CdS degraded MO faster than the bacterially precipitated CdS. This may be caused by the organic matrix embedding the CdS crystals, thus isolating the CdS NPs from the MO molecules and shielding them from the light and MO molecules. Thus one can assume by further purifying these NPs, the degrading rate of MO molecules in water solution might be improved. In summary, the photodegradation characterization proved the photoactivity of the bacterially precipitated CdS NPs. Although these particles degraded MO molecules slower than the corresponding CBD CdS particles, particle purification may improve their catalytic performance.

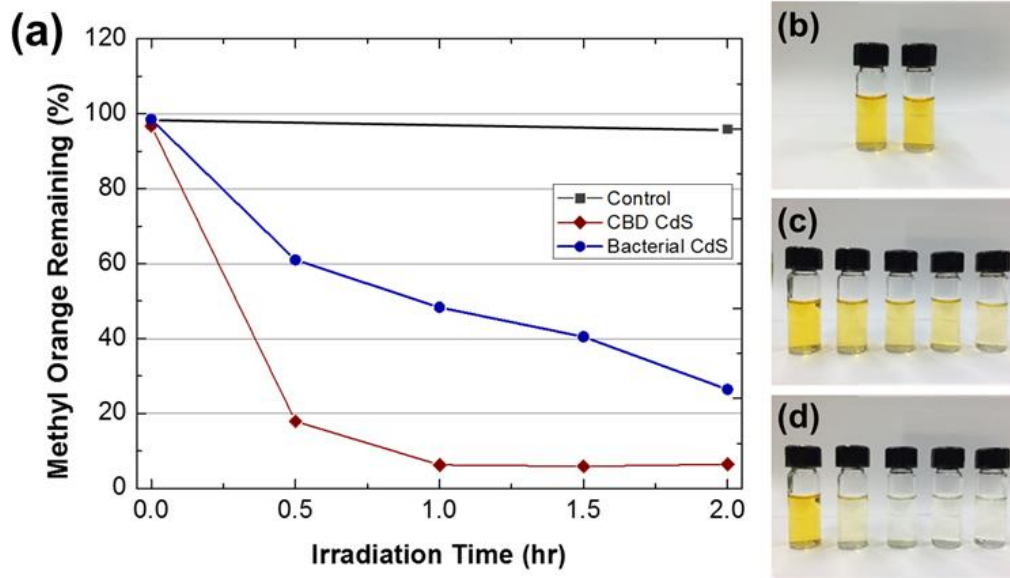


**Figure 11:** Photocatalytic degradations of MO for CdS NPs. (a) Plot of photocatalytic degradation of MO for control group (black squares), *E. coli* precipitated CdS (blue line with round dot), and CBD CdS (red line with diamonds). (b)-(d) are corresponding sample pictures of control group (no CdS), bacterially precipitated CdS group, and CBD CdS group.

## 2.2 Photoelectrochemical properties of the BAC CdS NPs

As a semiconductor material with a direct band-gap of 2.42 eV, one important application of CdS is water splitting.[87-90] When irradiated with light, electrons in the valence band will absorb the photo energy and be excited to the conductive band, forming electron-hole charge carrier pairs.[91] When the electrons and holes are collected before their recombination, a photo-current will be generated.[91] In addition, the band edges of the valence band and the conduction band makes CdS generate high

enough potential to reduce the hydrogen and oxidize oxygen of water, splitting water molecules into hydrogen and oxygen.[92] In PEC application, CdS functions as the photo-anode, supplying electrons to the cathode for hydrogen evolution by reducing water molecules.[91] Usually, a low external potential needs to apply to the system to drive the reaction.

To study the PEC performance of BAC CdS NPs, doping type and doping density, defect type, energy band bending, and the band structure at the electrode/electrolyte interface need to be studied. In addition, the overall PEC performance such as photocurrent density and hydrogen evolution onset potential are characterized.

To understand the doping type, doping density and energy band bending, electrochemical impedance spectrometry (EIS) were measured. To characterize the photocurrent density and the hydrogen evolution onset potential, transient photocurrent response and cyclic voltammetry (CV) were measured.

Electrochemistry measurement setup: To study the technological potential of our bacterially precipitated CdS NPs, we built a prototypical device by depositing CdS NPs onto a conducting, ITO thin film, and then measuring the photocurrent produced by this device in an aqueous electrolyte. CdS is a direct, wide-bandgap semiconductor, making it a photoactive material. When irradiated with visible light, CdS generates charge carriers which can be accumulated at electrodes before recombination. This

accumulation creates a voltage that can drive chemical reactions such as water splitting.[91] The transient photocurrent reflects both the photoactivity of the CdS and the internal series-resistance of the PEC cell. Briefly, a three-electrode system was used (Figure 12). The working electrode was connected to the electro-chemical workstation via a copper wire, which was isolated from the electrolyte by a glass tube and epoxy (not shown). The counter electrode (CE) was a 2.5 cm long platinum wire with a diameter of 0.5 mm, the reference electrode (RE) was Ag/AgCl, and the electrolyte was 0.5 M sodium sulfate ( $\text{Na}_2\text{SO}_4$ ) aqueous solution.

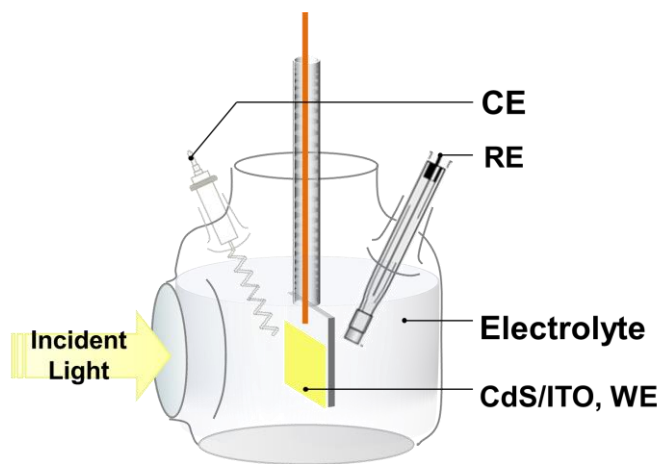


**Figure 12:** Experimental set-up used for measuring the transient photocurrent response of bacterially synthesized CdS NPs. The three-electrode electrochemistry cell was connected to an electrochemistry work station to detect the photoactivity of CdS NP thin films coated onto ITO covered glass slides. The incident light enters the cell through a planar quartz window. CE stands for counter electrode and RE stands for reference electrode.

EIS: EIS is a technique using Faraday's Law to measure the impedance at electrode/electrolyte interface.[93] Because of the reactant diffusion, reduction/oxidation reaction, and surface adsorption, etc.[93] the interface can be considered as a combination of resistor and capacitor in parallel or in series. the deconvolution of the resistance and capacitance under different radio frequency and different potential can provide an understanding of the EC properties of the interface. These EC properties are valuable to determine the BAC CdS NPs thin film's doping type, doping density, and band bending, etc.

In EIS, the impedance of the electrode/electrolyte interface will be measured with low potential perturbation with different frequencies. The result will be plotted as the Nyquist Plot, with x axis representing resistance (R) and the y axis representing  $1/(\omega C)$ , where  $\omega$  is the angular velocity of the frequency and C is the capacitance. With  $1/C^2$  values calculated from Nyquist Plots as a function of different potentials, one can obtain the Mott-Schottky plot, where the semiconductor's properties can be extracted.[93]

CV: Cyclic voltammetry is a common measurement to see the reduction and oxidation reaction under different potentials. In addition, surface states and other defects can also be seen due to the high sensitivity of CV.

Transient photocurrent response: Transient photocurrent response gives a direct evidence of the PEC performance of a device by measuring its photo incident current

that is generated by the WE. The higher the photocurrent density, the higher the energy conversion efficiency.

### 2.2.1 EIS measurements

From electrochemical impedance spectroscopy (EIS) measurements, values of the semiconductor space charge layer capacitance were extracted as a function of the applied voltage and plotted in the form of a Mott-Schottky plot (the equivalent circuit is shown in B.2). The slope of the Mott-Schottky plot (Figure 13) indicates that BAC CdS NPs are an n-type material, with a charge carrier density of  $\sim 5.6 \times 10^{16}/\text{cm}^3$ , in agreement with reported values for semiconductors used in photovoltaic applications.[94] Additionally, the intercept of the sloped line with the horizontal line at  $1/C^2 = 0$ , indicates a flat band potential of  $-0.58 \text{ V}$  (*vs.* Ag/AgCl at pH = 7).[95] While lower values have been reported elsewhere,[96, 97] a direct comparison cannot be performed, because the observed difference in flat band potentials may arise from differences at the semiconductor-electrolyte interface caused by different preparation and measurement conditions. For example, we used an organic-inorganic CdS compound surface instead of freshly cleaved single crystal surface (surface chemistry),[97] and we used an aqueous  $\text{Na}_2\text{SO}_4$  solution as the electrolyte instead of a sodium sulfide ( $\text{Na}_2\text{S}$ ) solution (composition of the electrolyte).[96] These factors can have a strong influence on the ion adsorption and hence the value of the flat band potential. Compared to oxide or III-V

semiconductor materials, these effects are likely more pronounced with BAC CdS NPs as their surface is a mixture of crystalline CdS surfaces and organic matrix materials.[98]

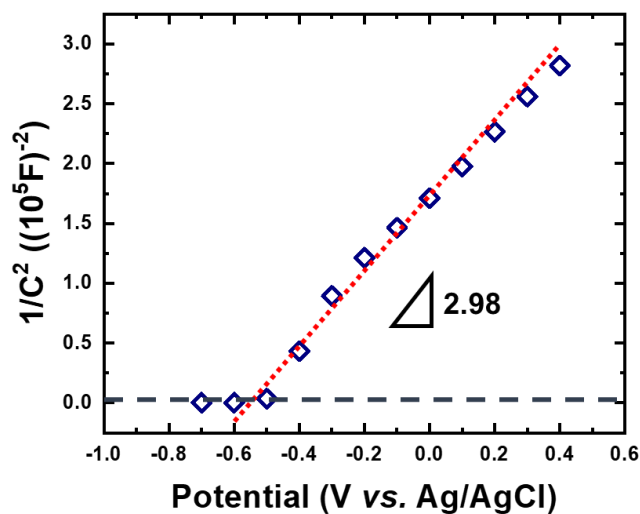


**Figure 13:** the Mott-Schottky plot of the BAC CdS NPs

### 2.2.2 CV measurements

The electron transport performance, which is influenced by surface states and the onset potential, was characterized by cyclic voltammetry (CV) measurements.[99] CV measurements performed in the dark (Figure 14a), show a cathodic current with a bias voltage lower than -0.7 V, which is likely related to hydrogen evolution.[91, 100] The small shoulder in the measured data at ~ -0.9 V likely is associated with  $Cd^{2+}$  reduction, while the anodic peak at ~ -0.7 V may arise from either adsorbed  $H_2$  or  $S^{2-}$

oxidation.[101] When the sample is illuminated, the CV curve shows a higher cathodic current for voltages below -0.7 V, which suggests that this potential is close to the Fermi level. This value also agrees with the flat band potential value obtained from EIS measurements. For voltages higher than -0.3 V, the CV curve under illumination starts to separate from that obtained in the dark. The difference between the onset potential and the flat-band potential indicates the presence of shallow surface states lying just below the conduction band.[99] Surface states are usually attributed to impurities or abrupt terminations in the crystal that trap electrons and holes, and thus reduce the charge transport efficiency inside the material. As a result, this implies that the band structure at the interface of the BAC CdS and the electrolyte has the form illustrated schematically in Figure 14b. (The relationship between flat band potential, Fermi energy level at the interface, and the reference electrode is shown in B.3.)

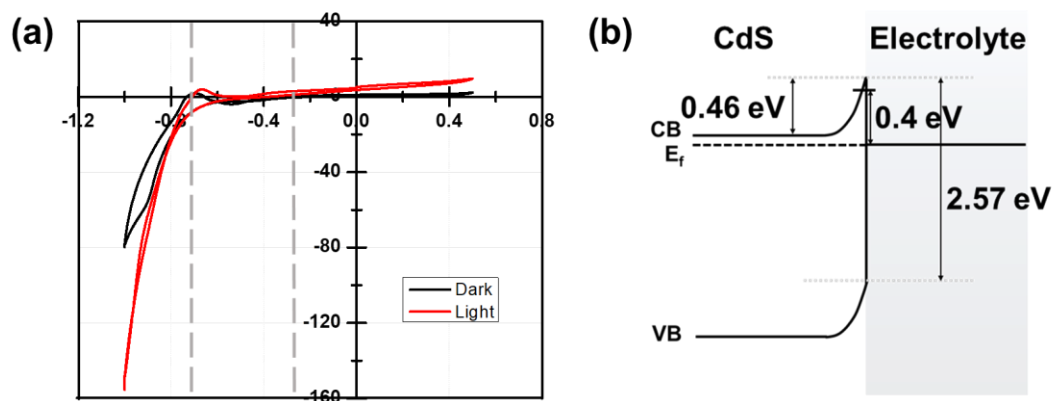


**Figure 14:** The CV curves and the energy band structure of BAC CdS. **(a)** CV curves of BAC CdS in the dark (black) and under illumination (red). **(b)** Schematic representation of the band structure of the CdS at the interface of the electrolyte.

### 2.2.3 Transient photocurrent and the energy band structure

To show the functionality of the BAC CdS, the transient current of these NPs was measured and compared to that of chemical bath deposited (CBD) CdS NPs. The transient currents were measured at open circuit potential (OCP) to evaluate the charge separation induced by illumination. Figure 15a shows that BAC CdS displays a photocurrent (8 mA/g) that is over 2× higher than that of CBD CdS (3 mA/g). We attribute this higher specific photocurrent to the presence of an organic matrix associated with BAC CdS, which likely gives a better contact to the indium tin oxide (ITO) glass substrate. Fourier Transform Infrared (FT-IR) photospectroscopy of BAC CdS reveals signals we attribute to carboxyl (-COOH) and amine (-NH<sub>2</sub>) functional

groups (Figure 16). These functional groups are present in the proteins that are part of the organic matrix, and render the NPs hydrophilic.[102, 103] We surmise that these functional groups are ionized in aqueous environments and thus give rise to electrostatic repulsion between the NPs when drop-casting from aqueous suspension. This effect contributes to the formation of uniform films. On the contrary, CBD CdS NPs tend to sediment in aqueous suspension, and when drop-casted on the ITO substrate, they do not form a uniform film. However, successive photocurrent measurements of BAC CdS NPs exhibit an exponential decay as depicted in Figure 15b. The likely explanation for this behavior is the loss of particles from the substrate surface. This is reasonable because after drop-casting the aqueous CdS particle suspensions onto the substrates, they were simply air-dried without any further heat treatment, or chemical bonding. Despite the obvious stability problems, the unique chemical composition, and, when compared to CBD CdS, enhanced electrochemical properties, make BAC CdS an interesting candidate for integration with other electronic materials.

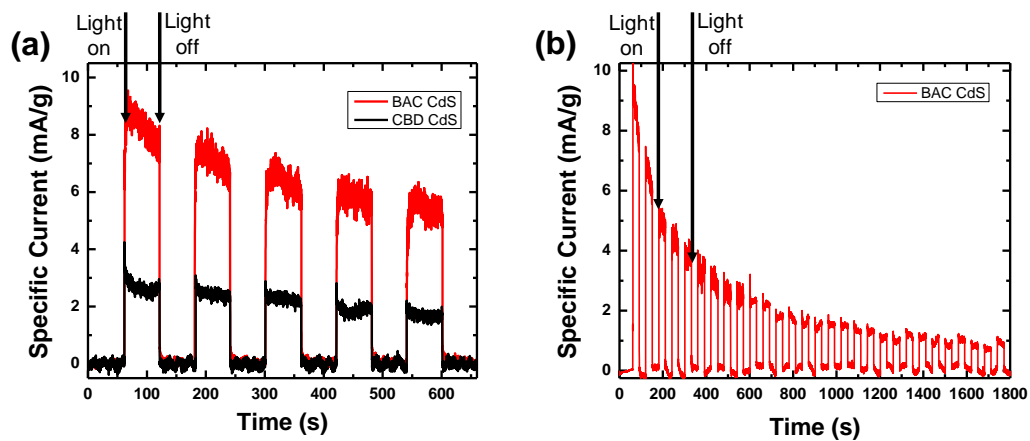


**Figure 15:** Transient current measurements. (a) Transient current of the BAC CdS (red) at OCP, compared to the transient current of same concentration of CBD CdS (black). (b) Transient current of BAC CdS at OCP for 30 min.

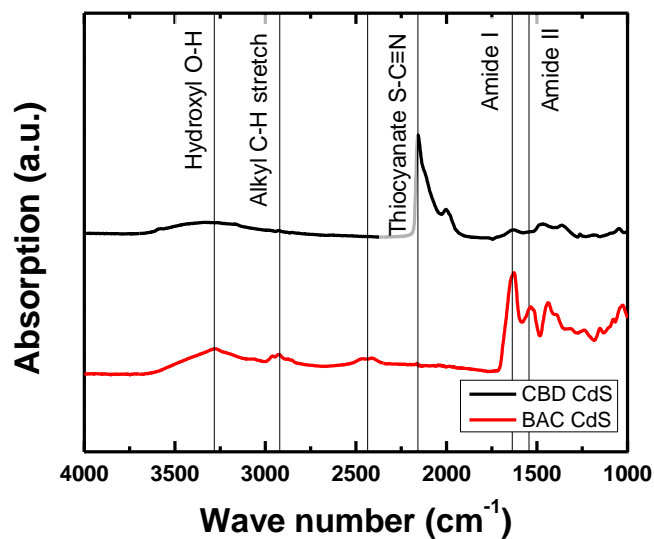


**Figure 16:** Comparison of FT-IR spectra of BAC CdS and CBD CdS NPs. The BAC CdS spectrum (red) shows signals of carboxylic acid, amine, and thiol groups.

### **2.3 PEC applications of BAC CdS with reduced graphene oxide**

With a basic understanding of the BAC CdS NPs, we took another step forward conceptually demonstrating that these biosynthetic NPs have potential to be applied in energy devices. Due to the existence of the organic compounds, the contact of BAC CdS NPs to substrate materials is better than CBD CdS.[80] Taking this advantage, we combine CdS with graphene sheets, to build a photo-charged capacitor. This is the first case to apply biosynthetic CdS NPs into energy device application.

Energy conversion devices have received intensive research attention during the past few decades.[104] Solar energy is a green and reusable energy source. Unlike other energy resources such as water, wind, thermal, etc, solar energy can be converted by comparably small sized devices, making it possible to be installed in personal electronic devices.[105] Energy storage is another intensively studied area, and electricity is the most commonly used media for small and personal devices.[106] For electricity storage, electrochemical batteries and electrochemical capacitors are two major studied areas.[106] In comparison with batteries, capacitors have advantage in storing and releasing energy quickly with simple device structures.[107] In this section, we plan to combine solar energy conversion and energy storage functions into one device: the photo-charge capacitor. The combined device has several advantages such as miniature device size compared to two different devices, high efficiency without extra contact resistance, and high reliability.[108, 109]

Approach: In previous sections, the solar energy conversion properties of BAC CdS NPs were studied. In this section, we combine the BAC CdS NPs with graphene to make the photo-charged capacitor. We note, that we cannot build such a device using uncapped chemically synthesized CdS NPs due to their tendency to agglomerate which prohibits formation of a thin film (B.4).

Hybrid (organic-inorganic) CdS electrode for PEC/storage application: We sandwiched BAC CdS NPs as a photo-active layer between an ITO top layer and a hydrogel electrolyte layer, supported on reduced graphene oxide (RGO) (Figure 17a). We used a polyvinyl alcohol (PVA) hydrogel layer,[110, 111] swollen with an aqueous sodium chloride (NaCl) electrolyte, to integrate the CdS layer with the RGO sheet.[110] To collect the current we attached a copper wire to the ITO layer. The edges of the electrode as well as the copper wire were covered with Epoxy resin (not shown in the figure) to prevent direct contact with the electrolyte when in operation. As a control sample, we coated BAC CdS NPs on ITO glass (Figure 17a).

We hypothesized that this layered hybrid electrode is able to convert solar energy into electricity and to store it for later use; *i.e.*, when light transmits through the ITO layer, electrons will be excited to the conduction band in the CdS layer, and the resulting holes will polarize the RGO sheet, which subsequently will store charges at the RGO/electrolyte interface. Figure 17b shows the energy diagrams of the hybrid electrode and the control electrode.

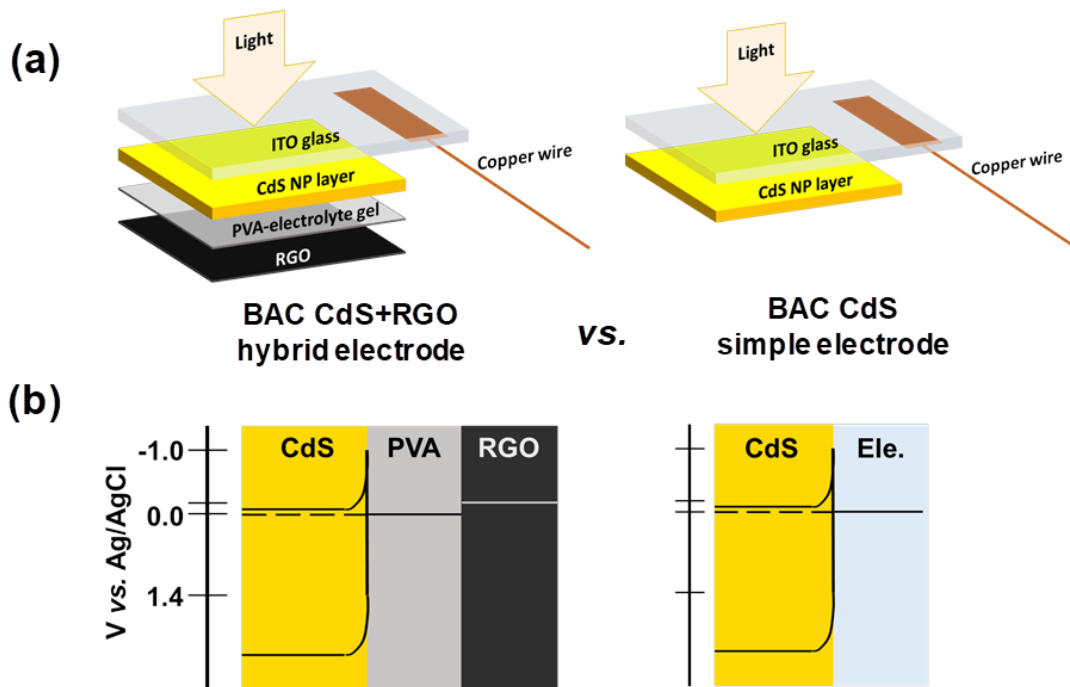
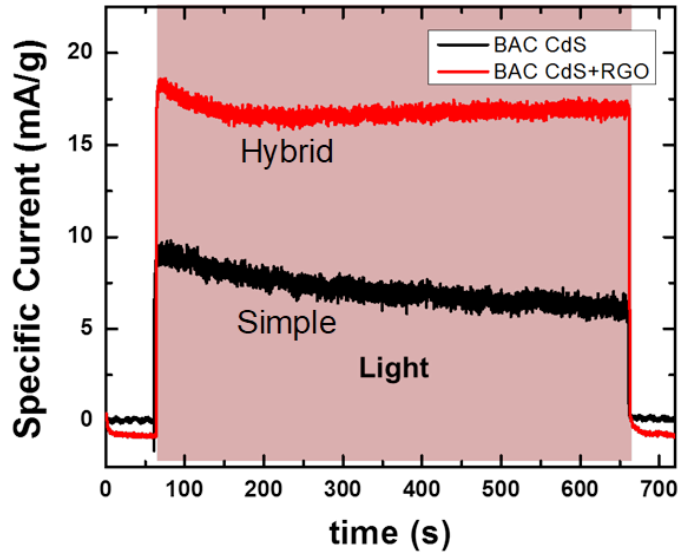


**Figure 17:** The schematics showing the multi-layer structures and band diagrams of the hybrid electrode and the simple electrode. **(a)** The multi-layer structure of the hybrid electrode (left) and the simple electrode (right). **(b)** The energy diagram of the hybrid electrode (left) and the simple electrode (right).

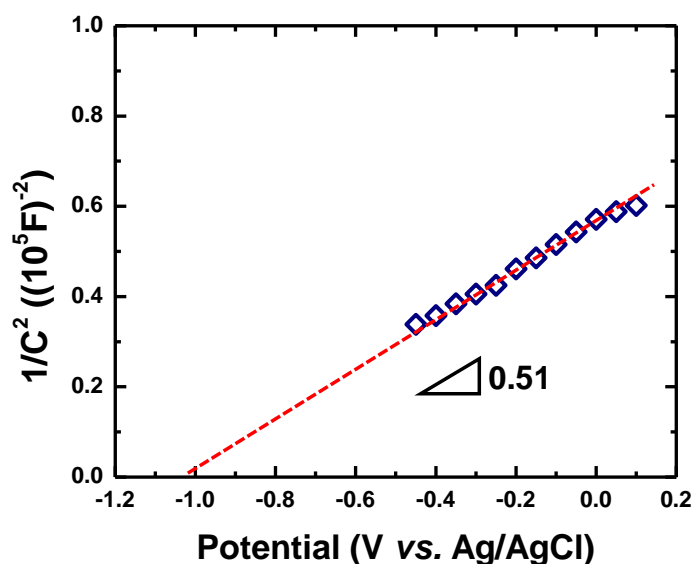
### 2.3.1 Organic/inorganic photocharged capacitor electrode

Figure 18 shows the transient current generated by the hybrid electrode when exposed continuously to light for 10 min at OCP. The hybrid electrode exhibits a higher and more stable photocurrent compared to that produced by a bare BAC CdS layer containing the same amount of CdS (simple electrode). Given the good mechanical properties of polymer gel electrolytes,[112] the PVA-electrolyte gel is believed to act as a buffer layer leading to a better stability of the hybrid electrode compared to the

configuration without the polymer. To further investigate the performance of the hybrid electrode, we performed EIS measurements and compared the results to those obtained on bare BAC CdS NP electrode. From the Mott-Schottky plots, we estimate the apparent flat-band potential to be  $\sim -1.09$  V (Figure 19), and the corresponding charge carrier density to be  $\sim 3.3 \times 10^{17}/\text{cm}^3$ . Compared with BAC CdS NP electrode, we attribute the negative shift of the flat band potential to charge injection and the blocking of surface states following the deposition of PVA. Consequently, the charge carrier density increased by one order of magnitude.



**Figure 18:** The transient current generated by the CdS-PVA-RGO hybrid electrode and by a BAC CdS NP electrode without PVA and RGO.



**Figure 19:** The Mott-Schottky plot of the CdS-PVA-RGO hybrid electrode. The intercept is -1.09 V with a slope of  $0.51 \times 10^{-10} \text{ F}^{-2}/\text{V}$ .

To show the ability of the hybrid electrode to store charges, we performed CV measurements in the dark and under illumination, and compared these to those of a bare BAC CdS NP layer. As seen in Figures 20a and b, and in contrast to the BAC CdS NP electrode, the hybrid electrode exhibits an obvious capacitive behavior, which is enhanced under illumination. We hypothesize that the improved capacitance (*i.e.* charge storage properties) results from an enhanced dielectric constant of the hybrid structure following RGO deposition.[113] Additionally, the photo-current generated by the hybrid electrode is higher than that of the BAC CdS NP electrode. This difference arises from the negative shift of the flat-band potential which allows a greater band bending and thus a better photo-generated charge separation.

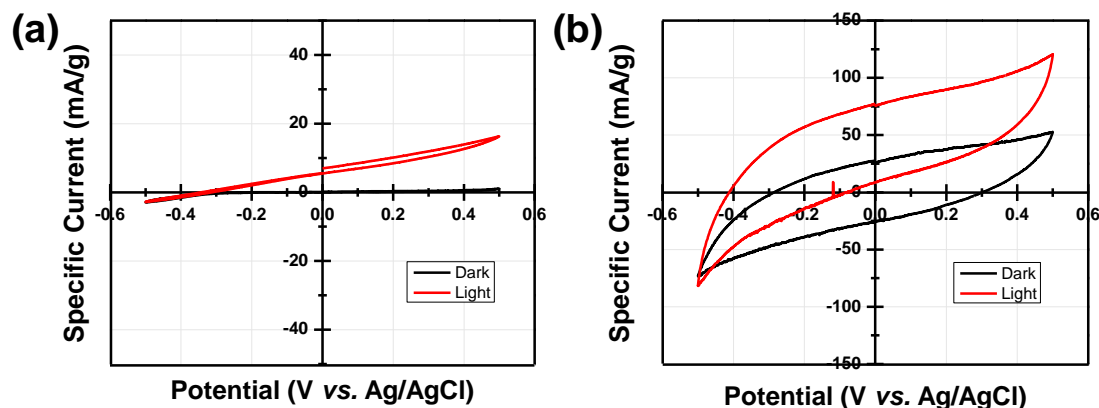


**Figure 20:** CV curves of the simple electrode and hybrid electrode. (a) CV curves of simple electrode in the dark and light. (b) CV curves of the hybrid electrode in the dark and light.

To show the possibility of storing the photo-generated charges in the hybrid electrode, we performed photo-charge/galvanostatic discharge measurements at open circuit (Figure 21a). The process is divided into four steps as marked in the figure. First, the OCP is measured in the dark. Second, the light is switched on for 90 seconds until the OCP reaches a steady value. At this point, the electrode generates a photo-voltage of  $\sim 600$  mV, which is higher than that for the BAC CdS NP electrode (Figure 21a) and comparable to values found in the literature.[114, 115] Third, after switching the light off the OCP was measured in the dark for 10 seconds. The only small potential drop, which is common for capacitors, suggests that the hybrid electrode can store the charges that were generated during the photo charging step. Finally, the electrode is discharged at a constant specific current of 10 mA/g in the dark. The discharge process lasted longer than that for the BAC CdS NP electrode (Figure 21b), and shows that the energy stored

in this electrode can be extracted by connection to an external circuit. During the galvanostatic discharge process, the slope of the voltage-current curve is proportional to the capacitance according to **Equation 3**:

$$C = I \frac{dV}{dt} , \quad \text{Equation 3}$$

From the inset of Figure 21b, it is determined that in our conditions, the hybrid electrode is capable of storing approximately two times more charge than the pristine BAC CdS layer.

This experiment proves the concept that our hybrid electrode can convert photon energy into electric charge and store it. To further improve the device performance, the BAC CdS particle size and the film thickness, as well as the electrolyte composition, all need to be optimized.

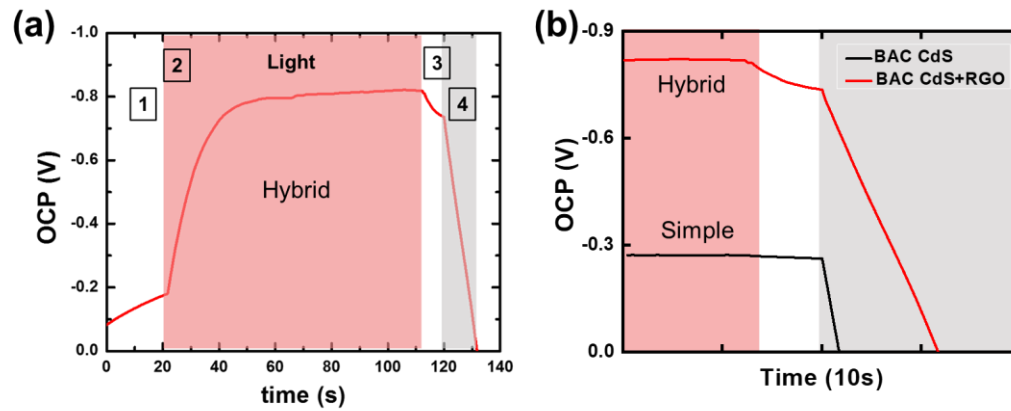


**Figure 21:** the OCP measurement of the hybrid and simple electrode. **(a)** OCP test of the hybrid electrode. The four areas indicated in the figure represent four steps: 1) stabilization, 2) photo-charging, 3) charge storage, and 4) discharge. **(b)** The comparison of the photo-voltage and discharge performance at the same discharge rate for the BAC CdS NP electrode (black) and the hybrid electrode (red).

### **3. Effect of cysteine passivation on the charge transport properties of BAC CdS and CBD CdS<sup>2</sup>**

Transition metal (TM) sulfides are promising materials for photocatalytic applications where they convert solar energy to generate hydrogen fuel. However, these materials are still in their early stages of development compared with their widespread use in photovoltaic applications.[116] Two major hurdles for the photocatalytic function of these materials are their low energy conversion efficiency[117] and low photostability.[118] Many TM nanoparticles (NPs) are high efficiency photocatalytic materials and are thus widely studied.[119, 120] These NPs have interesting properties compared with those in the bulk. For example, these materials are highly catalytical because of their large surface to volume ratio.[119] In addition, due to the quantum confinement effect, the NPs' size not only influences their optical properties (light absorbance), but also their electron transport properties.[121] Previous studies showed that NPs can absorb more light with a lower electron-hole recombination rate in comparison to the same materials in bulk.[121] Meanwhile, the stability and the energy conversion efficiency of nanoparticles can be tuned and improved by surface modification using (organic) ligands.[122-124]

---

<sup>2</sup>The following content is adapted from an abstract "Y. Feng, J. Huang, E. Ngaboyamahina, K Marusak, J Glass, M Mikkelsen, S. Zauscher, "Organic ligands enhance the recombination lifetime and photoelectrochemical performance of biosynthesized CdS nanoparticle thin films", (Talk) American Chemical Society 256, 2018" Yaying Feng conducted experiments, wrote the manuscript, and was involved in designing experiments and manuscript revision.

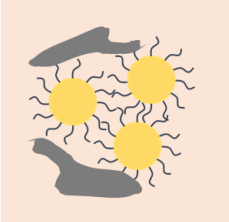
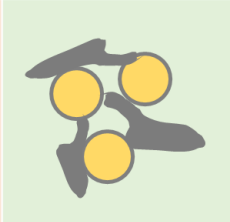
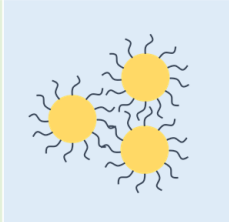
In Chapter 2, we showed that bacteria can precipitate cadmium sulfide (CdS) nanoparticles with useful photocatalytic properties.[79] In this enzymatically driven precipitation process, we added cysteine as the sulfur source, and discovered that films of these bacterially precipitated CdS nanoparticles exhibit (i) carrier lifetimes that are substantially longer and exhibit (ii) photocurrent densities that are higher compared to those in films prepared from unpassivated, chemically synthesized CdS nanoparticles. We attribute the higher photocurrent to the presence of cysteine, which passivated the NPs' surface and prolonged their charge carrier lifetime.

Although the biosynthesis of CdS and other TM chalcogenide NPs is widely studied and PEC applications of BAC CdS have been reported, little is known about the effect of the chemical environment in which biosynthetic NPs are precipitated on the NPs' PEC properties. Considering the compositional analysis (FTIR) of BAC CdS particles and the synthesis process, we hypothesize that organic compounds, especially cysteine, added to the bacterial culture play a critical role for the properties of BAC CdS NPs and account for their improved photocurrent generation. This motivates a more systematic exploration of the effect of organic ligands on the PEC properties of BAC CdS, with a view to optimize or apply these properties.

To test the influence of cysteine on optical and electrical properties of BAC CdS NPs, we prepared four sets of samples (see Table 2): bacterially precipitated CdS (BAC CdS, group 1), BAC CdS without cysteine (BAC(-Cys) CdS, group 2), chemically

precipitated CdS that that is passivated by cysteine (Cys CdS, group 3), and chemically precipitated CdS without passivation (CBD CdS, group 4). By comparing the measurement results of sample groups 1 and 2, we evaluated the influence of cysteine on the optical and electrical performance. We note that although *E.coli* produces cysteine, this amount is significantly smaller than that exogenously added. By comparing the measurement results of sample groups 3 and 4, we evaluated the influence of cysteine on the optical and electrical performance of chemically precipitated CdS NPs.

**Table 2: Four CdS NP groups prepared to study the effect of cysteine as the capping ligand**

	<b>BAC CdS (group 1)</b>	<b>BAC –Cys CdS (- Ctrl, group 2)</b>	<b>Cys CdS (+ Ctrl, group 3)</b>	<b>CBD CdS (- Ctrl, group 4)</b>
Environment	Cell culture	Cell culture	DI water	DI water
Cd source	CdCl <sub>2</sub>	CdCl <sub>2</sub>	CdCl <sub>2</sub>	CdCl <sub>2</sub>
S source	<b>Cysteine</b>	Na <sub>2</sub> S	Na <sub>2</sub> S	Na <sub>2</sub> S
Additional cysteine	<b>Yes</b>	No	<b>Yes</b>	No
Expected sample configuration				

We use photoluminescence (PL) and time-resolved PL (TRPL) to characterize the influence of cysteine on the opto-electronic properties of CdS nanoparticles. There are two types of recombination mechanisms involved in the relaxation of excitons in

semiconductors: one is radiative recombination, and the other is non-radiative recombination. PL measures the radiative recombination emissions at different wavelengths and reveals different energy levels of excitons. Therefore, PL is used to obtain information on shallow and deep energy states. The non-radiative recombination involves “vibrational relaxation” (VR) and “internal conversion” (IC). Vibrational relaxation describes the process in which excitons drop to a lower energy state in the same energy level via vibration; and internal conversion describes the process in which excitons drop from the lowest energy state in a higher energy level to the highest energy state in a lower energy level. The combination of VR and IC can transport excitons from an excited to the ground state without light emission. The time scale of this process is usually shorter than  $10^{-12}$  s. On the other hand, the radiative recombination refers to a process in which excitons drop from one energy level to another no matter which energy state they start in or end up with. The time scale of radiative recombination is usually  $10^{-5}$  to  $10^{-8}$  s.[125] Although there is a third recombination mechanism, called “triplet recombination” ( $10^{-4}$  to  $10^4$  s), it is generally not considered in PV/PEC applications. Thus, in PV/PEC applications, the radiative recombination effect is preferred, given that all excitons will recombine ultimately. In addition, a longer radiative recombination time scale generally indicates a longer lifetime of excited charge carriers. TRPL directly provides information about the lifetime of the photo-excited charge carriers.

### **3.1 Chemical synthesis of cysteine capped CdS NPs**

In this section we describe the precipitation of cysteine capped CdS NPs. The precipitation method we used was adapted from a previously reported method.[126] Briefly, in this method the CdCl<sub>2</sub> precursor is incubated with cysteine in aqueous solution to form a cysteine-Cd complex. Next, for chemical bath deposited NPs, Na<sub>2</sub>S is added to the solution to ultimately yield cysteine capped CdS NPs. For further details, see Appendix: Experimental Details.

#### **3.1.1 Structural and compositional characterization of chemically synthesized cysteine capped CdS**

To assess the structure and composition of chemically precipitated CdS NPs, we used TEM and XPS to analyze the particle core, while we used FT-IR to analyze the organic ligands. Figure 22a shows a high resolution TEM image with d-spacing analysis of chemically synthesized CdS NPs, fabricated using the method described above. As shown, CdS nanocrystallites predominately form a FCC structure, with the {111} and {200} planes resolved, and a particle size of ~6 nm in diameter. Although we cannot rule out the possibility that there are HCP crystals that we did not capture, the FCC lattice spacings obtained by TEM are consistent with published values for CdS. Figure 22b shows the XPS region scan showing the characteristic energy split of the Cd 3d<sub>3/2</sub> (405.0 eV) and Cd 3d<sub>5/2</sub> (411.8 eV) characteristic peaks.[127] By peak de-evolution we find that about 50% of the Cd ions on the surface of the NPs are bound to oxygen, which we

attribute to surface oxidation during drop-casting the as prepared CdS NPs to substrates in the ambient environment. Together these results confirm the precipitation of CdS.

To assess the presence of a capping ligand, here cysteine, in the chemically precipitated CdS NPs, we used FTIR spectroscopy. Figure 22c shows the characteristic peaks of N-H, C-O, and S-H from the cysteine capped CdS sample and cysteine ligand sample. The N-H and C-O peaks prove the existence of cysteine, and the missing S-H peak suggests that cysteine likely has reacted with CdS by forming a Cd-S bond. Together with TEM and XPS characterization, we thus confirm the precipitation of cysteine capped CdS NP using the chemical synthesis method.

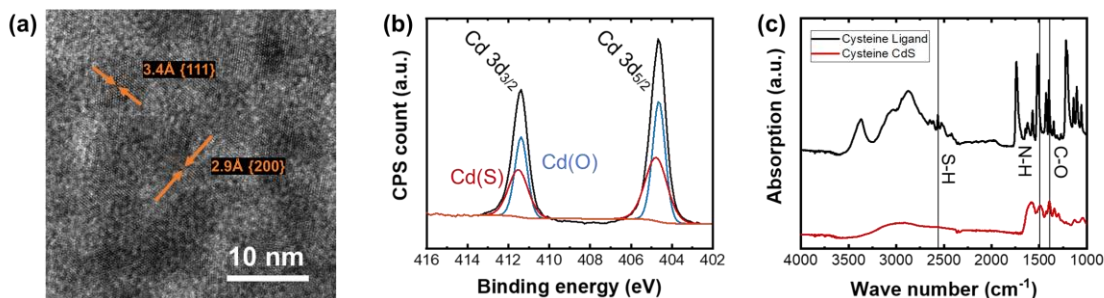


**Figure 22:** Structural and compositional characterization of chemically synthesized CdS NPs. **(a)** High resolution TEM image with d-spacing measurements; **(b)** XPS region scan spectrum showing the characteristic binding energy split of the Cd 3d peak. **(c)** FTIR spectrum showing the existence of cysteine in chemically synthesized cysteine modified CdS NPs.

### 3.1.2 Optical properties of chemically synthesized cysteine capped CdS

We characterized the optical properties by UV-vis absorption spectroscopy and photoluminescence spectroscopy. Figure 23a shows the fluorescence response of differently sized cys-CdS nanoparticles. From left to right, the particle size increases, and the fluorescence color changes from blue-green to orange-red. An increasing NP size was realized by increasing the molar ratio of S to Cd in the reaction mixture. The difference in NP fluorescence arises from the quantum confinement effect, which is directly linked to NP size. UV-vis and PL spectra show that as the particle size increases, the absorption onset and the emission peak are red-shifted (Figure 23b and c). This result shows that we are able to precipitate size controlled, cysteine-passivated CdS NPs, using chemical synthesis methods.

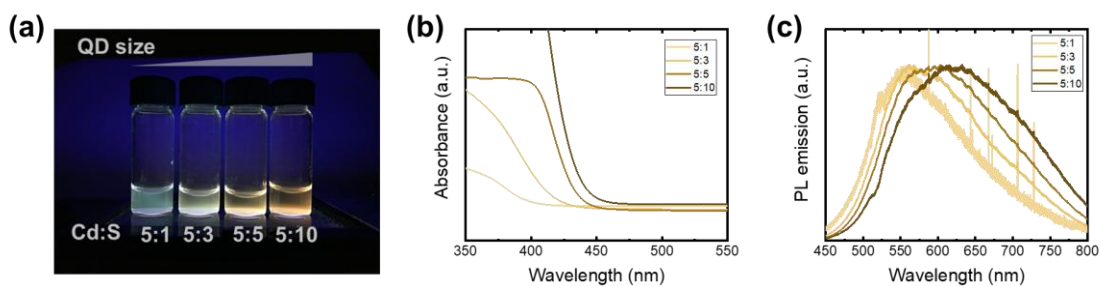


**Figure 23:** Fluorescence effect and optical measurements of cysteine capped CdS NPs. (a) Photograph of the chemically synthesized cysteine capped CdS NPs solution under UV lamp. (b) UV-vis absorption onset for the CdS NPs shown in (a). (c) Photoluminescence emission spectra for the CdS NPs shown in (a).

### 3.2 Effect of cysteine on charge carrier transport

In this section we illuminate cysteine's effect on carrier transport by comparing BAC CdS with BAC-Cys CdS (*i.e.*, group 1 *vs.* group 2), and Cys CdS with CBD CdS (*i.e.*, group 3 *vs.* group 4). In semiconductor materials, charge carrier transport is determined by three major factors: (i) the energy band bending that influences the magnitude of carrier transport, (ii) the carrier lifetime and carrier mobility that influence the kinetics of carrier transport processes, and (iii) the contact resistance at the CdS-ITO substrate interface that influences the carrier collection. To obtain information about CdS's energy band bending, we characterized the flat band potential by electrochemical impedance spectroscopy (EIS) measurements. Next, we measured the photovoltage generated by CdS NPs under illumination to qualitatively understand how ligands affect charge carrier transport.

Figures 24a and b show the Mott-Schottky plot of the four CdS samples obtained from EIS measurements. The flat band potential is determined by the intercept of the fitted straight line (dashed) and the x axis.[128]

**Table 3: The flat band potential and photovoltage measurement results**

	BAC CdS	BAC -Cys CdS	Cys CdS	CBD CdS
Flat band potential	-0.6 V	-0.9 V	-0.6 V	-1.1 V
MS plot slope	1.0	0.9	0.8	0.9

Photovoltage	0.71 V	0.65 V	0.71 V	0.60 V
--------------	--------	--------	--------	--------

The data in Table 3 show that the flat band potential shifts in the anodic direction when cysteine is present. For an n-type semiconductor a more anodic flat band potential indicates smaller band bending, and thus a weaker electric field in the depletion region, which in turn weakens the extent of excited electron separation.

The charge carrier density can be read from the slope of the fitted line in Figure 24.[129] Although it is hard to obtain absolute values of charge carrier density — due to a lack of knowledge of the samples’ actual surface area— our result shows that the presence of cysteine does not change charge carrier density significantly since the slopes of the fitted lines are similar. Thus, the presence of cysteine is less favored for charge separation due to the less intensive band bending.

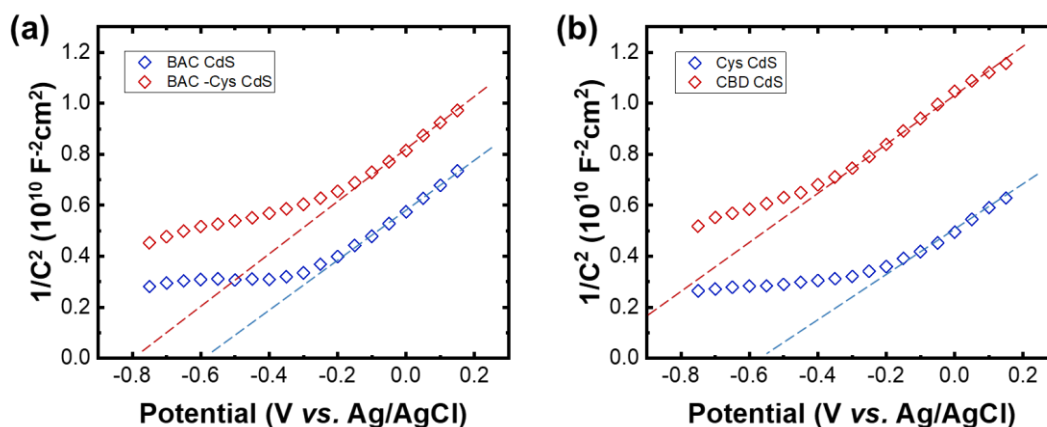


**Figure 24:** Mott-Schottky (MS) plot of CdS NPs presented in Table 2. (a) MS plot of BAC CdS and BAC -Cys CdS. (b) MS plot of Cys CdS and CBD CdS.

Under illumination, most electrons are excited from the VB to the CB at the electrolyte-CdS interface,[130] then, these charge carriers travel to the CdS-ITO substrate interface, and finally to the counter electrode through wires. The flat band potential thus describes the strength of the electric field at the electrolyte-CdS interface (space charge layer of the semiconductor thin film). During charge carrier transport, the actual electric field across the entire CdS thin film might drop due to a loss of carriers.[130] To see this effect, we measured the open circuit potential (OCP) in the dark and under illumination (Figure 25). We took the difference of the most anodic value in the dark and the most cathodic value under illumination to determine the photovoltage these CdS NPs can generate. By comparing the photovoltage (Table 3), we found for both biosynthetic and chemically synthesized CdS NPs, that NPs precipitated with added cysteine generated higher photovoltages than NPs without added cysteine. This suggests that additional cysteine improves carrier transport kinetics.

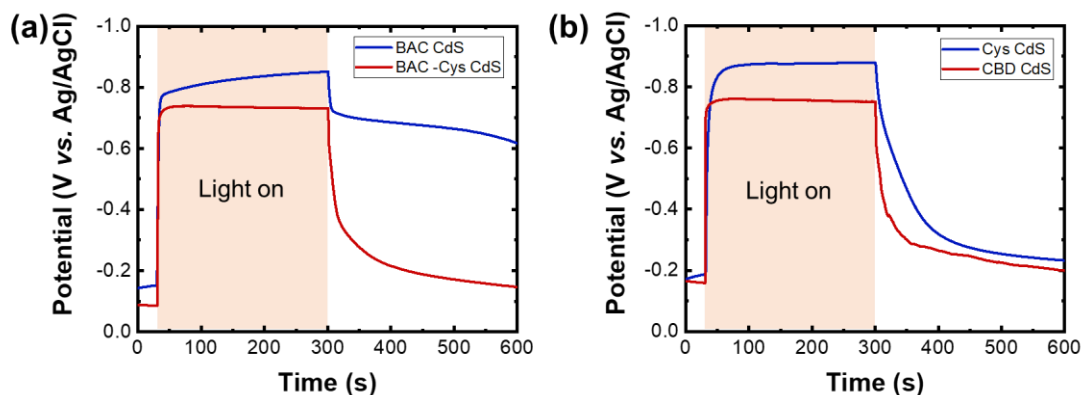


**Figure 25:** Open circuit potential of CdS NP thin films. **(a)** Open circuit potential of BAC CdS and BAC -Cys CdS NPs in the dark and under illumination. **(b)** Open circuit potential of Cys CdS and CBD CdS in the dark and under illumination.

To verify an improved charge carrier kinetics, we measured the light emission properties of CdS NPs by PL and TRPL. Figure 26a shows the PL spectra of BAC CdS (group 1) and BAC(-Cys) CdS (group 2). The intrinsic emission wavelengths of BAC CdS and BAC(-Cys) CdS are both at 480 nm ( $\sim 2.6$  eV), which means both sample groups contain similarly sized QD nanoparticles. The emission peak at 700 nm ( $\sim 2.0$  eV) of both samples indicates that carrier recombination in deep states is likely caused by sulfur vacancies.[131] Since the major recombination appears at 600-700 nm, we measured the TRPL in this range to study carrier kinetics. The normalized emission decay plots (Figure 26b) show that at deep states, the lifetime of BAC CdS NPs is much longer than that of BAC(-Cys) CdS NPs. This suggests that cysteine in the BAC CdS increases electron transport by slowing carrier recombination.

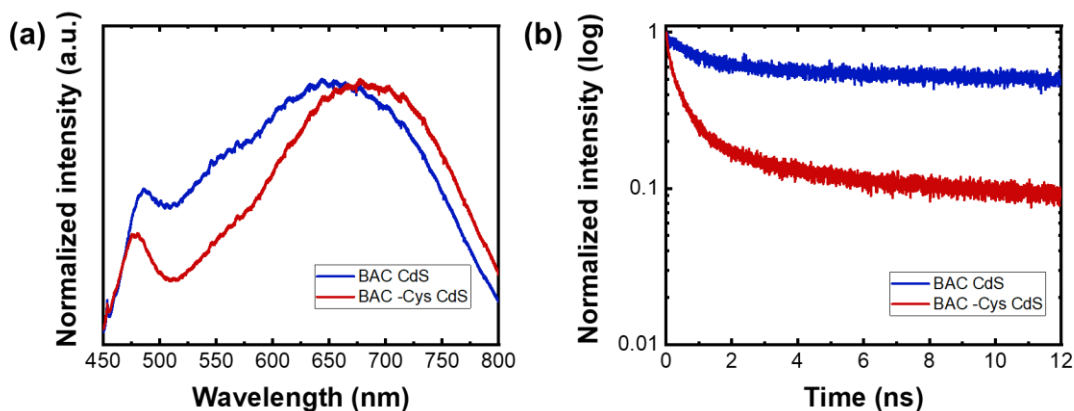


**Figure 26:** Photoluminescence measurements of the BAC CdS NPs and BAC(-cys) CdS NPs. **(a)** PL spectra of the BAC CdS (blue) and BAC(-cys) CdS (red) NPs. **(b)** TRPL of the BAC CdS and BAC(-cys) CdS NPs in the 600-700 nm emission range.

To further explore the impact of cysteine on the electron transport process in CdS NPs, we compared the TRPL of Cys CdS (group 3) and CBD CdS (group 4) NPs. Figure 27 shows that at 670 nm, Cys CdS NPs have a longer carrier lifetime than CBD CdS NPs. Taken together, these experiments suggest that added cysteine during chemical and bacterial CdS NP precipitation has a profound effect on the exciton recombination process, and more specifically, prolonging the carrier lifetime. This validates our hypothesis that additional cysteine improves carrier transport kinetics.

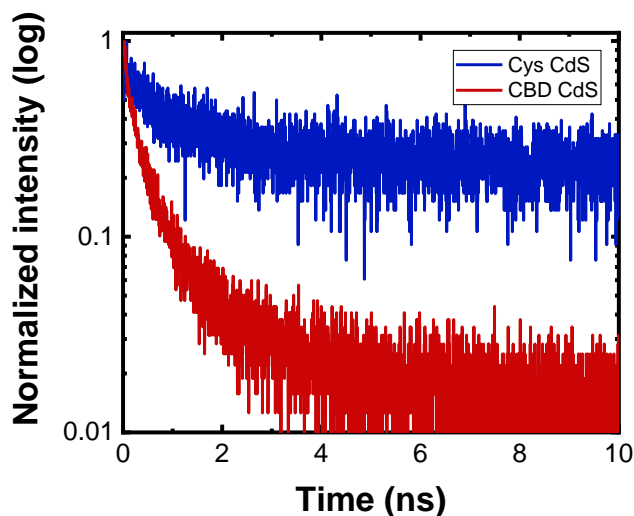


**Figure 27:** TRPL spectra Cys CdS (blue) and CBD CdS (red) measurements at 670 nm emission wavelength.

At the CdS-ITO substrate interface, the presence of cysteine likely reduces the contact resistance. This notion is supported by the differences observed in the Nyquist plots from EIS measurement of biosynthetic CdS and chemically synthesized CdS (Figure 28). A Nyquist plot shows the real part (x axis) and imaginary part (y axis) of the impedance for a range of frequencies. The real part of the impedance that is associated with the lowest point of the imaginary part of the impedance represents the resistance of the system (Figure 28). This includes the resistance of the electrolyte and the contact resistance at the CdS-ITO substrate interface. Given that the resistance of the electrolyte is very low due to a high ion concentration (0.5 M Na<sub>2</sub>SO<sub>4</sub>), we attribute the observed resistance mainly to the contact resistance. By comparing results from BAC CdS (group 1) with BAC -Cys CdS (group 2), we saw a consistently lower contact resistance for a

range of applied bias voltages. The same trend is seen when comparing results from Cys CdS (group 3) with CBD CdS (group 4). The reduced contact resistance facilitates charge carrier collection at the interface and thus contributes to the higher photovoltages observed in Figure 25.

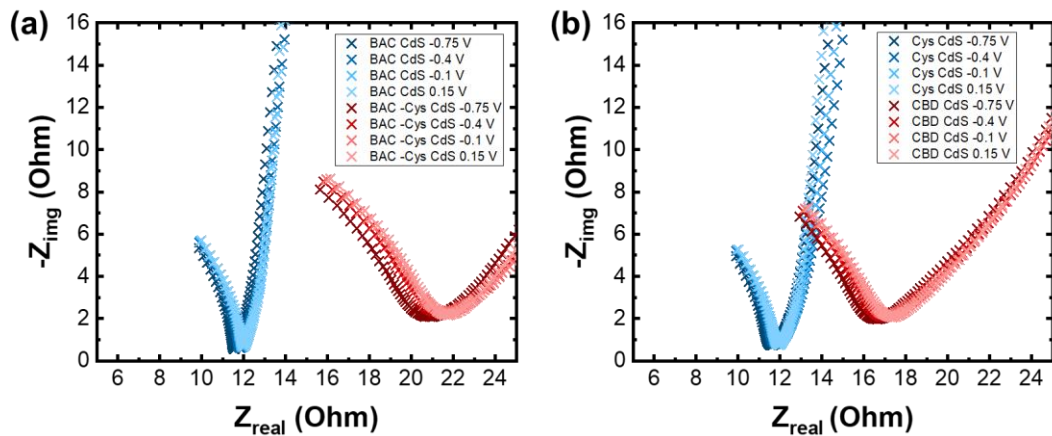


**Figure 28:** Nyquist plots of CdS from EIS measurements. (a) Biosynthetic CdS under different applied bias, including BAC CdS (blue) and BAC -Cys CdS (red). (b) Chemically synthesized CdS under different applied bias, including Cys CdS (blue) and CBD CdS (red).

In conclusion, we showed that organic ligands, here cysteine, added to a bacterial precipitation system, affect the PEC performance by improving charge carrier kinetics (carrier transport and collection at the interface) even though they shift the flat band potential at the electrolyte-CdS interface to the anodic direction (*i.e.*, weaker band bending). This study gives us an understanding of how cysteine affect the PEC performance and how BAC CdS NPs benefit from the chemical environment (organic

matrix) to generate higher photo current comparing with non-passivated, chemically synthesized CdS NPs. From this understanding, we are motivated to control the chemical environment of BAC CdS NPs to further control their electronic properties, and thus potentially their PEC performance.

## **4. Thiolate ligand modification of biosynthetic CdS NPs and control of their band structure<sup>1</sup>**

In Chapter 3 we showed that Cys affects PEC performance. This observation motivated us to explore the use of other organic ligands to exert control over the electronic properties of biosynthetic CdS NPs.

We previously showed that by changing the amount of cysteine added into bacterial cell culture, we can control the size and thus the bandgap of biosynthetic CdS NPs.[37] Here, we show that by changing the chemical environment around biosynthetic CdS NPs, specifically, by using preincubated X-Cd (X = different organic ligands) complex precursors, we can change the band edges and potentially the photoelectrochemical properties of biosynthetic CdS NPs.

### ***4.1 Biosynthesis of CdS NPs modified with different ligands using bacterial precipitation***

In this section, we demonstrate that bacteria systems can be manipulated to precipitate CdS NPs that are modified with different ligands.

---

<sup>1</sup> The following content is adapted from a paper in preparation "Y. Feng, C. M. Zhang, C. Han, M. L. Sartorelli, V. Blum, J. T. Glass, L. You, S. Zauscher, "Biosynthesis of cadmium sulfide nanoparticles: Effect of organic ligands on electronic properties." Yaying Feng conducted experiments, wrote the manuscript, and was involved in designing experiments and manuscript revision.

### 4.1.1 Approach

Briefly, instead of directly adding the aqueous  $\text{CdCl}_2$  precursor solution to the bacterial cell culture, we preincubate the  $\text{CdCl}_2$  precursor with different organic ligands (*i.e.*, cysteine, cysteamine, 3-mercaptopropanol, and 6-mercaptohexanoic acid) prior to adding it to the bacterial cell culture (Figure 29). Details of the synthesis process can be found in Appendix: Experimental Details.

The rationale of choosing these thiolate ligands is that they are all water soluble, have short carbon chain lengths, and reflect a range of polarities and charges. As such, these ligands are thought to change the electronic properties of the bacterially precipitated CdS NPs, and thus their photoelectrochemical properties.

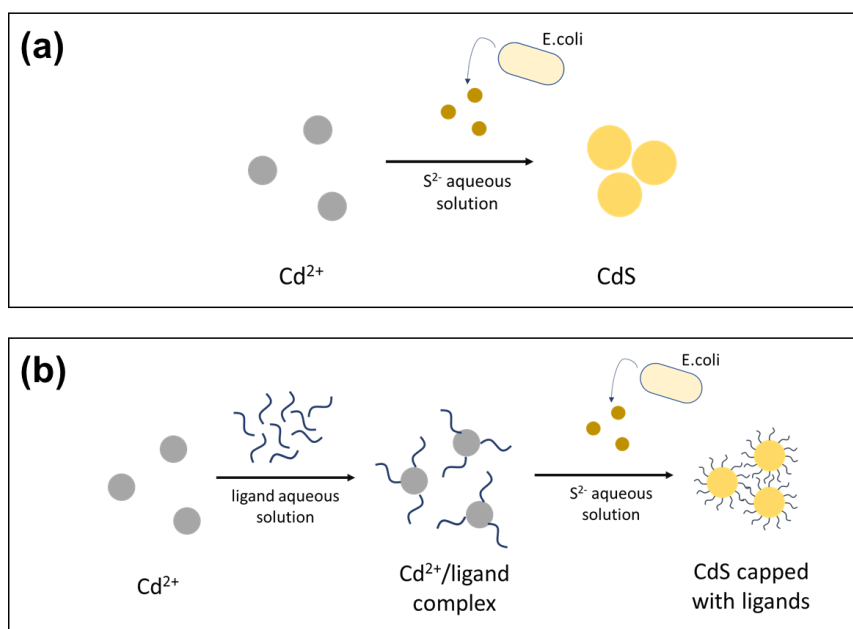


**Figure 29:** Biosynthetic CdS NP synthesis protocols. **(a)** Traditional protocol, published in our earlier work. **(b)** The new synthesis protocol.

We used high resolution TEM (HRTEM) and XPS characterizations to show CdS NPs are precipitated. The detailed measurement method can be found in Appendix: Experimental details.

#### **4.1.2 Results**

We characterized the NP precipitates from the cell culture using high resolution transmission electron microscopy (HR-TEM) and X-ray photoelectron spectroscopy (XPS). The d-spacing obtained by analysis of TEM images matched in many cases the hexagonal {101} ( $d = 3.18 \text{ \AA}$ ) and cubic {111} ( $d = 3.37 \text{ \AA}$ ) planes of CdS (Figure 30, Table 4). These results agree with our previous observations,[37, 80] and suggest that bacterially precipitated CdS crystallites are likely polymorphous. Furthermore, the analysis of TEM images revealed a uniform crystallite size of about 8 - 10 nm. (Figure 30)

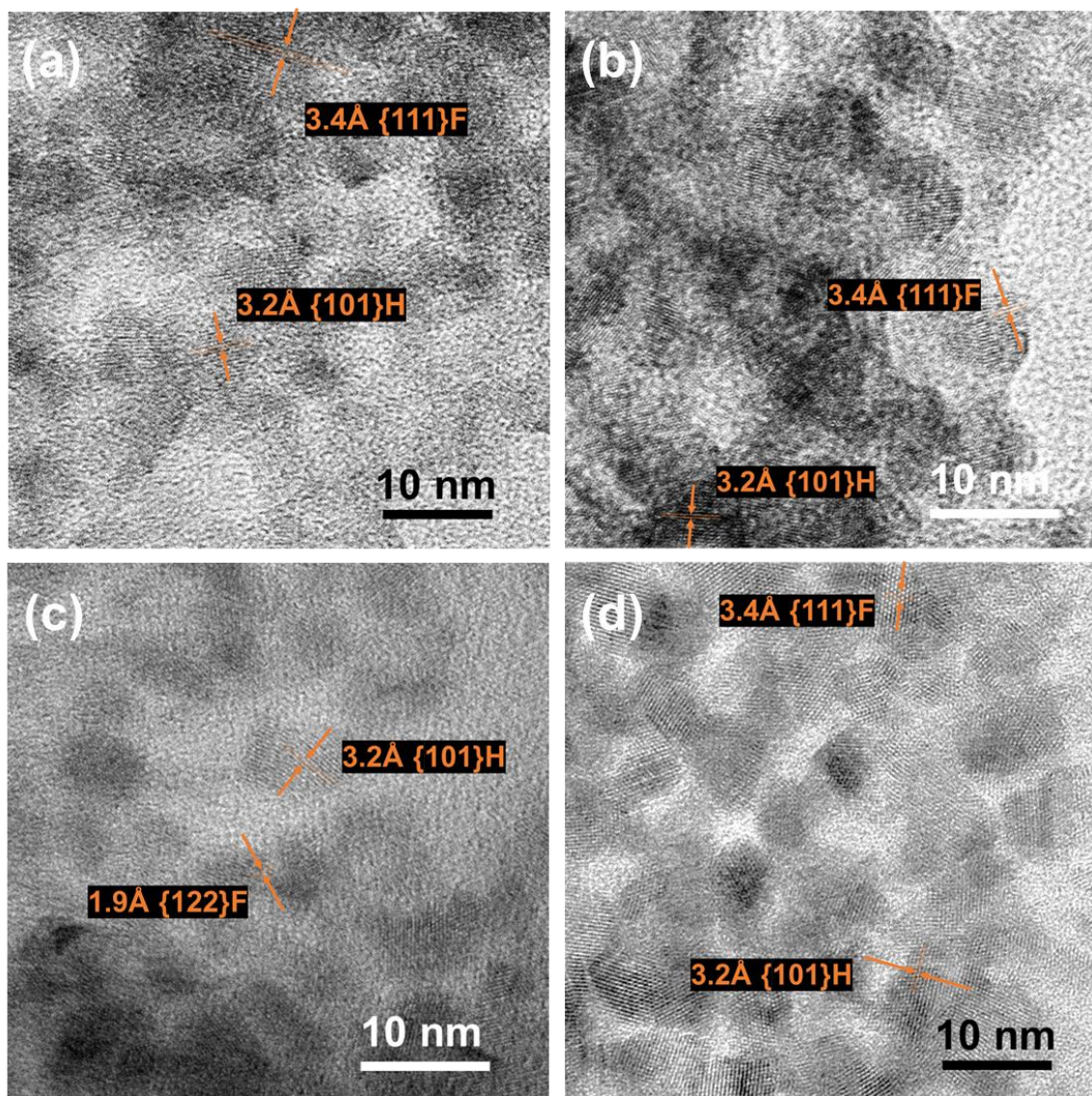


**Figure 30:** HR-TEM images of biosynthetic CdS NPs modified with different ligands: Cys (a), CysM (b), MP (c), and MHA (d). The measured d-spacing and corresponding lattice planes are marked.

**Table 4: d-spacing measured from HRTEM images in comparison with calculated values<sup>2</sup>**

<b>FCC</b>	d-spacing (calculated)	d-spacing (measured)	<b>HCP</b>	D-spacing (calculated)	D-spacing (measured)
{111}	3.37 Å	3.4 Å	{101}	3.18 Å	3.2 Å
{122}	1.94 Å	1.9 Å			

The chemical identity of the NP precipitates was further established by XPS. (Figure 31) High resolution XPS spectra in the binding energy region from 402 eV to 416 eV revealed the presence of the characteristic Cd 3d<sub>3/2</sub> (411.8 eV) and Cd 3d<sub>5/2</sub> (405.0 eV) peaks.[127] Since we used aerobic cell cultures, 22% - 75% of surface Cd ions from the sample bind with O. Together, these measurements confirm the presence of CdS NPs in all our precipitates.

---

<sup>2</sup> Lattice parameters used to calculate d-spacing are: a = 5.832 Å for FCC structure; a = 4.160 Å and c = 6.756 Å for HCP structure.[132] Joswig J-O, Springborg M, Seifert G. Structural and Electronic Properties of Cadmium Sulfide Clusters. The Journal of Physical Chemistry B. 2000;104:2617-22.

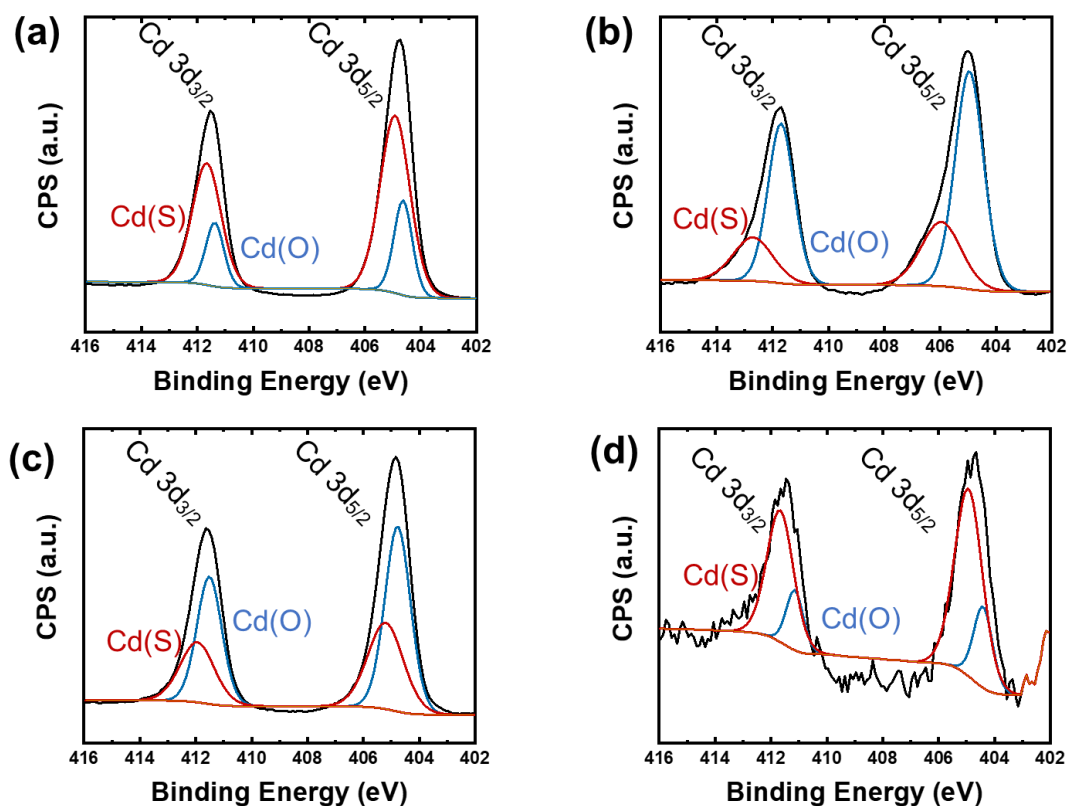


**Figure 31:** Region scan of XPS spectra of biosynthetic CdS modified with different ligands: Cys (a), CysM (b), MP (c), and MHA (d).

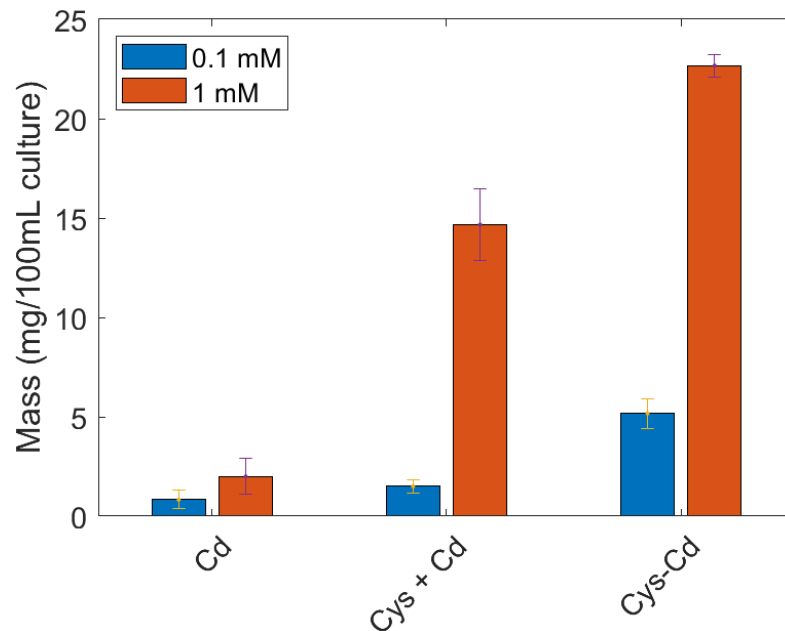
Since we used a biosynthetic approach to precipitate CdS nanocrystals, a direct identification of the capping ligands was difficult. For example, in FTIR spectra the ligand characteristic signals are buried in the signals arising from the organic matrix in which the particles are embedded.

## ***4.2 Cysteine used as an organic ligand improves the biosynthetic CdS yield***

In this section we show that our modified bioprecipitation protocol can improve CdS NP yield compared to the yield observed in our previous approach, in which we did not incubate the CdCl<sub>2</sub> precursor prior to addition to the bacterial precipitation system.

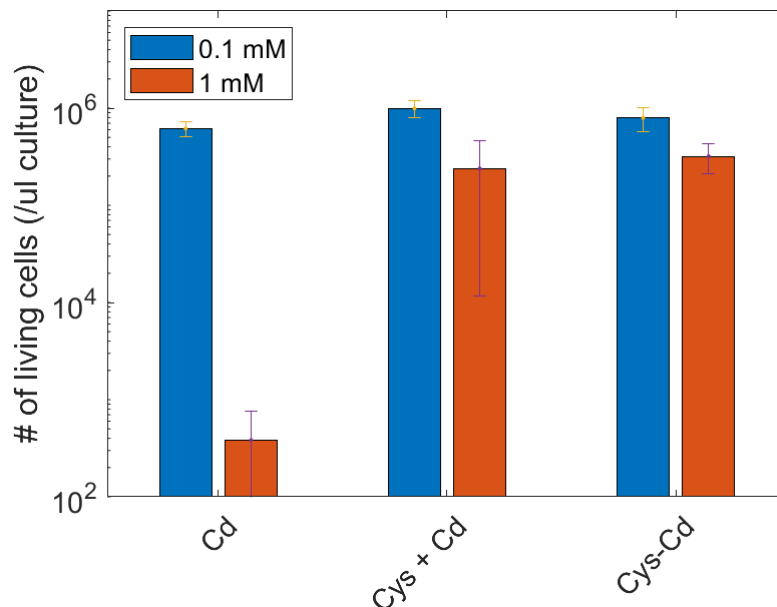
Specifically, we compared the mass of the biosynthetic precipitates prepared with ligand pre-incubated Cd complexes to that obtained with unmodified CdCl<sub>2</sub> precursors, under otherwise identical culture conditions. The detailed method of this measurement is described in Appendix: Experimental details.

Figure 32 shows the precipitated NP mass for different precipitation methods at two different Cd precursor concentrations. Specifically, we observe that by preincubating the CdCl<sub>2</sub> precursor with cysteine ligands, the precipitated CdS NP mass increases substantially (tripled at 0.1 mM CdCl<sub>2</sub>, and over 50% increase for 1mM CdCl<sub>2</sub>), maintaining the overall cysteine concentration the same (compare Cys + Cd with Cys-Cd group). For comparison we also show the CdS NP yield resulting from our previously published protocol.



**Figure 32:** The mass of precipitation. Cd group represents that the Cd precursor is CdCl<sub>2</sub> aqueous solution; Cys + Cd group represents that the Cd precursor is CdCl<sub>2</sub> aqueous solution, added separately with additional cysteine; Cys-Cd group represents that the Cd precursor is preincubated cys-Cd<sup>2+</sup> complex aqueous solution.

One reason for the improved yield is simply the additional amount of cysteine introduced into the cell culture by the Cys-Cd<sup>2+</sup> complex, which yields higher precipitated amounts, particularly when also the CdCl<sub>2</sub> precursor concentration is increased. Furthermore, a study of the cytotoxic effect of the new precipitation method suggests that the improved yield likely arises from the reduced cytotoxicity of the Cys-Cd<sup>2+</sup> complex, which keeps the bacterial culture at a higher metabolic level at high Cd precursor concentrations (Figure 32). Specifically, Figure 33 shows that introducing a high Cd<sup>2+</sup> concentration (1 mM), 100 times more bacteria survived in the Cys-Cd<sup>2+</sup> group than the Cd group.



**Figure 33:** Cell viability testing. The number of living cells in the culture after precipitation is measured and compared between Cd group and Cys-Cd group.

These observations are of considerable economic importance as they show that the use of organic ligands to complex the toxic transition metal precursors can dramatically increase the precipitation yield by allowing higher TM precursor concentrations.

### **4.3 Organic ligands tune the band structure of biosynthesized CdS**

CdS is a direct bandgap semiconductor which finds broad application in energy conversion applications. In this section we show that different thiolate ligands can change the band edges of biosynthetic CdS NPs by up to 0.8 eV. By changing and

controlling the band edge position, we can tune the band structure of biosynthetic CdS to engineer heterojunctions when combining with other p-type semiconductor materials. For example, researchers showed the effect of band edge tuning of PbS NPs and demonstrated higher solar cell efficiency using ligand-modified PbS NPs.[133, 134] We thus suggest that by tuning the band edges we can improve the photo to electric energy conversion efficiency of devices built using biosynthetic CdS NPs.

We used three techniques to reconstruct the energy band structure: i) Kelvin-Probe Force Microscopy (KPFM) for work function measurements, ii) X-ray Photoelectronic Spectroscopy (XPS) cut-off energy measurements to determine the energy difference between  $E_F$  and the valance band maximum ( $E_{VBM}$ ),[134] and iii) UV-visible absorption spectroscopy for band gap ( $E_g$ ) measurement.

KPFM measures the local contact potential difference ( $V_{CPD}$ ) between the conductive AFM tip and the sample surface.  $V_{CPD}$  is related to the work functions ( $E_\phi$ ) of the AFM tip and sample (Equation 4).[135]

$$V_{CPD} = [E_\phi(sample) - E_\phi(tip)]/e. \quad \text{Equation 4}$$

The  $E_\phi$  of the AFM tip was calibrated with freshly cleaned silicon, which has a known work function of 4.85 eV.[136] With this information, the work function of CdS NPs and the corresponding Fermi level position ( $E_F$ ) can be calculated. The height profile and potential profile of biosynthetic CdS containing Cys, CysM, MP, and MHA ligands are shown in Figure 33. The measured work function of thin films (including a

controlled CdS sample that is chemically precipitated with no ligand modification) are summarized in Figure 34. The difference in the  $E_{\phi}$  indicates the differences in the amount of energy required to extract electrons from the material surface. The work function is sensitive to a crystal's orientation and its surface chemical state (*e.g.*, surface oxidation, adsorbed species).[137] In our case, we deal with a polycrystalline sample with random orientation of the crystallites, thus our measured work function should be considered an average. For chemically synthesized CdS NPs, surface oxidation reduces the work function of Cd-terminated surfaces and increases the work function of S-terminated surfaces, which can lead to a compensation of the effect as shown by Sasaki.[137] In the case of biosynthetic CdS NPs it is likely that the CdS core is more stable to oxidation under atmospheric conditions because of the presence of capping ligands and other organic compounds. Additionally, we conducted work function measurements in a nitrogen environment with low humidity (<10% HR) to minimize surface oxidation. When comparing the extent of surface oxidation of biosynthesized CdS with different ligands (measured by XPS, Figure 31) with the work function (measured by AFM), we did not observe a correlation. These observations lead us to conclude that the measured differences of the work function among biosynthesized CdS with different ligands is largely due to the characteristics of the ligand and not surface oxidation.

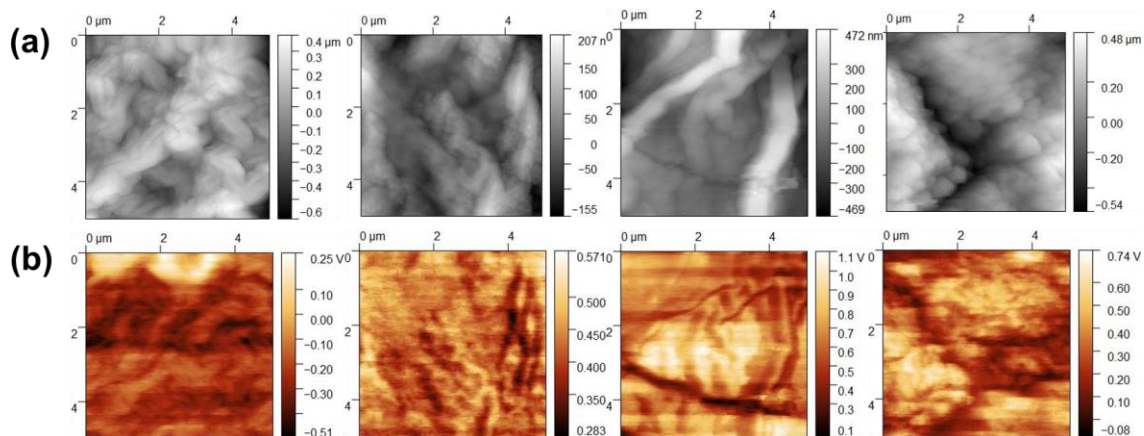


**Figure 34:** AFM images of biosynthetic ligand modified CdS NPs. **(a)** The height profile of the NP particles drop-casted on silicon substrates. From left to the right, the CdS NPs are modified with Cys, CysM, MP, and MHA. **(b)** The potential profile of the CdS NPs modified with Cys, CysM, MP, and MHA, from left to right.

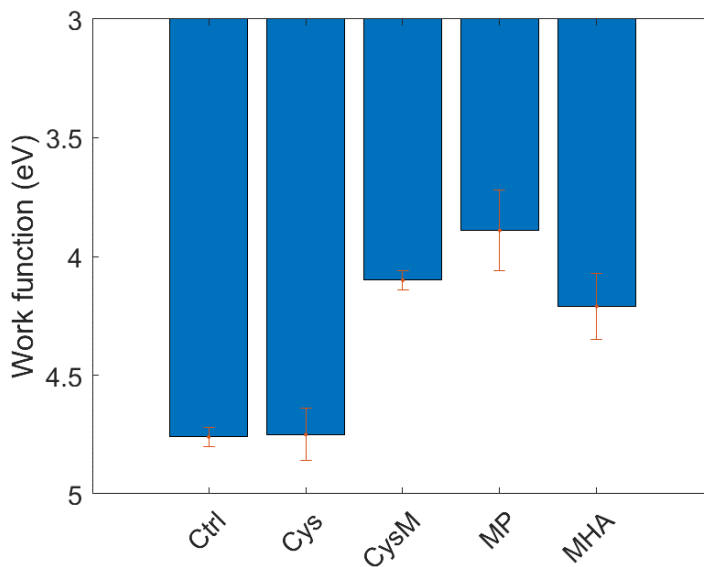


**Figure 35:** Work function of different CdS NPs. Ctrl represents chemically precipitated CdS NPs with no ligand modification; Cys, CysM, MP, and MHA represents biosynthetic NPs precipitated with Cys, CysM, MP, and MHA, respectively.

The positions of the valence band edge, *i.e.*, ( $E_F - E_{VBM}$ ) for CdS modified with Cys, CysM, MP, and MHA ligands were determined by XPS (Figure 35a) and are listed in Table 4. As seen, the position of the Fermi energy level between the valence and conduction band edges indicates that the biosynthetic CdS NPs are n-type semiconductors, in agreement with the molar ratio of Cd:S obtained from XPS measurement (Table B5).[138] The ionization energy ( $E_{IE}$ ) is determined by [134]

$$E_{IE} = E_{\phi} + (E_F - E_{VBM}), \quad \text{Equation 5}$$

and is shown in Table 4. The observed differences in  $E_{IE}$  are likely caused by differences in charge and polarizability of the different ligands. When comparing the ionization energy of two CdS NPs modified with polar ligands (Cys and MP) with that of unmodified CdS, one can see that  $E_{IE}$  decreases as the polarity increases (calculated:  $\mu_{Cys} = 1.95$  Debye,  $\mu_{MP} = 2.95$  Debye, Figure B6). This trend observed for polar ligands agrees with reports in the literature.[134]

Since XPS is a surface sensitive measurement technique, the state of surface oxidation may influence the measured ionization energy. Systematic experiments are needed to firmly establish the impact of oxidation on the valence band maximum. However, when comparing the extent of surface oxidation of biosynthesized CdS with different ligands with the ionization energy (both measured by XPS, Figure 36a), we did not observe a correlation. This leads us to conclude that the effect of surface oxidation on the ionization energy is likely small.

Finally, the conduction band edge was calculated using the relation:

$$E_{\text{CBM}} = E_{\text{VBM}} + E_{\text{g}}, \quad \text{Equation 6}$$

where  $E_{\text{g}}$  is the bandgap, measured using UV-vis absorption microscopy (Figure 35b). The bandgap is extracted from Tauc plots (Figure B7). By comparing  $E_{\text{g}}$  among the CdS NPs, we don't see a significant change (Table 4). This is due to the fact that  $E_{\text{g}}$  is mainly determined by NP size, which in turn is controlled by the concentration of the Cd and S precursors added to the bacterial culture.[139]

In summary, we have demonstrated that using a biosynthetic precipitation system, we can control the electronic structure, specifically the band edges, of the CdS NPs by preincubating the  $\text{Cd}^{2+}$  precursors with different thiolate organic ligands (Figure 35c).

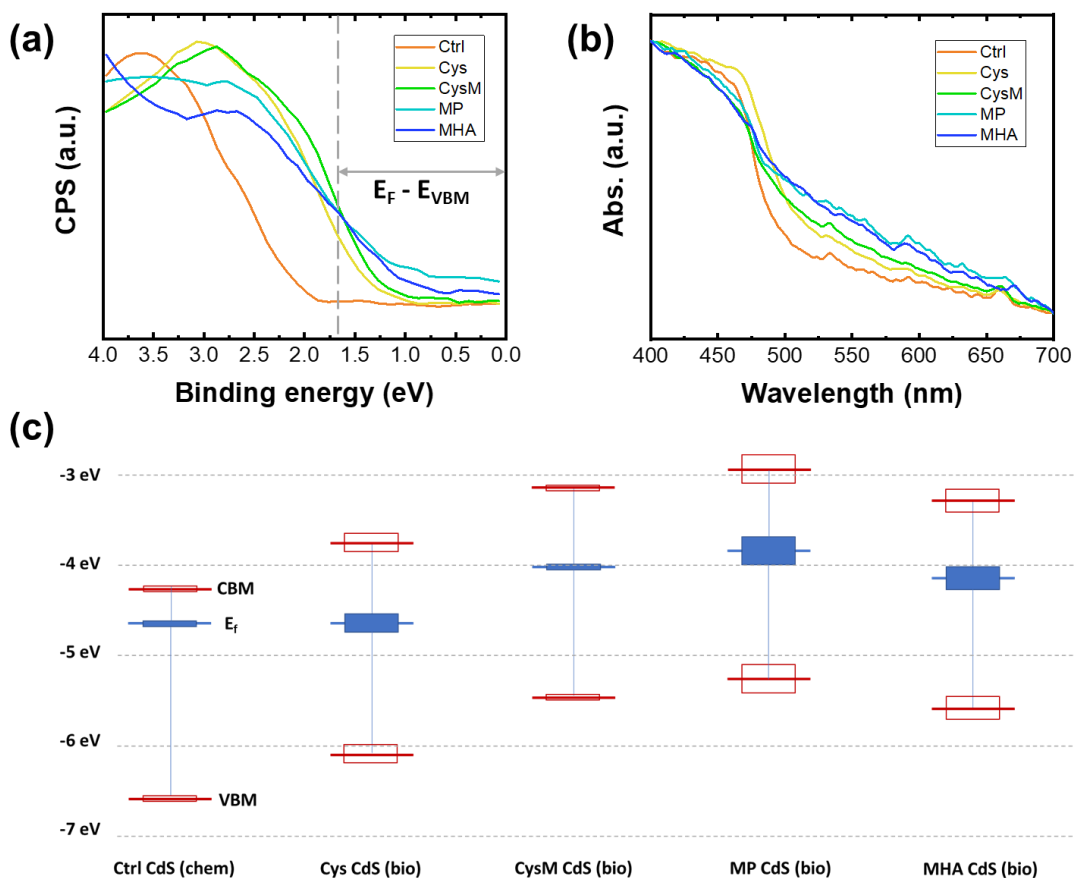


**Figure 36:** Band edge tuning of biosynthetic CdS NPs precipitated with ligands and chemically synthesized CdS. **(a)** XPS cut-off energy measurement of the Ctrl, Cys, CysM, MP, and MHA CdS samples. **(b)** UV-vis absorption measurement of the Ctrl, Cys, CysM, MP, and MHA CdS samples. **(c)** The band edge positions of the Ctrl, Cys, Cysm, MP, and MHA CdS samples.

**Table 5: Work function, Fermi level to VBM energy difference, and bandgap of Ctrl, Cys, CysM, MP, and MHA CdS samples**

	Ctrl	Cys	CysM	MP	MHA
$E_{\phi}$	$4.76 \pm 0.04$ eV	$4.74 \pm 0.11$ eV	$4.10 \pm 0.04$ eV	$3.88 \pm 0.17$ eV	$4.21 \pm 0.14$ eV
$E_F - E_{VBM}$	2.0 eV	1.5 eV	1.4 eV	1.4 eV	1.3 eV
$E_g$	2.5 eV	2.5 eV	2.5 eV	2.5 eV	2.4 eV

## 5. Conclusions

### 5.1 Summary

In this work, we studied bacterially precipitated CdS NPs and their (photoelectrochemical) PEC applications. Specifically, (i) we studied their PEC characteristics to understand their energy band structure and also demonstrated a PEC application; (ii) we studied the charge carrier transport dynamics and kinetics to understand the effect of organic ligands on the CdS NPs' PEC performance; and (iii) we precipitated biosynthetic CdS NPs with different ligands to tune their energy band edge.

Together, the results from these studies provide an understanding of the unique properties of biosynthetic CdS NPs and their potential for energy conversion and storage applications, thus advancing bio-precipitation technology and use of these materials for engineering applications.

From the PEC characterization and application study we learned that bacterially precipitated CdS NPs are clusters of nanocrystallites (quantum dots, ~7 nm) with mixed FCC and HCP crystal structures, embedded in an organic matrix. These NPs are photoactive (bandgap ~2.57 eV), are able to degrade methyl orange under solar illumination, and can generate higher photocurrent than chemically precipitated CdS NPs. Using 0.5M Na<sub>2</sub>SO<sub>4</sub> aqueous solution as electrolyte, these NPs form a Schottky junction at the electrolyte-CdS interface, with a flat band potential of ~0.6 V. Furthermore, we demonstrated that these NPs can be used to fabricate photo-charged

capacitors when forming a layer by layer structure with graphene. This device structure harnesses the high affinity of the organic matrix to graphene, and allowed, for the first time, to demonstrate a PEC energy conversion/storage application of biosynthetic CdS NPs.

To study the effect of cysteine, a necessary precursor for biosynthesis and also a potential ligand, on charge carrier transport dynamics, we used chemically precipitated CdS NPs as comparison, as they are not affected by the presence on a organic matrix. We first hypothesized that the NPs are likely capped by cysteine, a thiolate amino acid that has high affinity to  $\text{Cd}^{2+}$  ions. By comparing the PEC properties of both chemically synthesized and biosynthetic CdS NPs we found that cysteine and the organic matrix adversely affect the charge transport dynamics by pushing the flat band potential to the anodic side. However, cysteine improves the charge transport characteristics of CdS NPs, which is supported by their higher photovoltage and substantially longer charge carrier lifetimes. This study thus helped us to understand key factors that influence the PEC performance of bacterially precipitated CdS NPs and motivated us to study how to further control the electronic properties of bacterially precipitated CdS NPs.

We expanded the capability of the bacterial precipitation system by using different organic ligands to (i) improve the CdS yield and (ii) tune the band edge position by controlling the chemical environment of the biosynthetic CdS NPs.

Together, our results guide the way toward efficient biosynthetic system for the precipitation of transition metal chalcogenide NPs with engineered properties for future energy applications.

## **5.2 Future work**

Future work should address two directions: (i) it should focus on further developing biosynthetic precipitation technology, such as cell-free precipitation, to efficiently produce transition metal chalcogenide NPs with even better PEC properties, and (ii) it should focus on combining the advantages of organic ligands on PEC properties with established materials fabrication processes, such as EALD, to fabricate even higher performing transition metal chalcogenide materials.

To further develop biosynthetic technology, we suggest to explore cell-free synthesis with PEC property control. With increasing desire to control the size and purity of biosynthetic TM chalcogenide NPs, researchers have started to use cell-free precipitation methods, harnessing enzymes isolated from bacterial precipitation systems. In 2016, Dunleavy *et al.* used a single enzyme to both catalyze and template the formation of CdS nanocrystals and obtained size controllable CdS NPs. [38] Specifically, they used media containing cystathionine  $\gamma$ -lyase smCSE from *Stenotrophomonas maltophilia* (*S. maltophilia*) to generate H<sub>2</sub>S by degrading L-cysteine. The H<sub>2</sub>S was then reacted with Cd<sup>2+</sup> to precipitate CdS NPs. Because the *S. maltophilia* was removed prior to NP precipitation, there was substantially less unnecessary biomass from the bacteria

(as compared to intercellular precipitation) allowing the production of NPs with high purity and small size dispersity. [38] In addition to this “clean” enzymatic approach, there has recently emerged a great number of approaches that utilize plant cell extracts for TM NP precipitation

To transfer the advantages of ligands, we propose to study electrochemical atomic layer deposition (EALD) of CdS with ligands. Atomic layer deposition (ALD) is widely applied for the fabrication of photovoltaic (PV) and PEC devices due to its capability to generate conformal thin films.[140] While most ALD technologies are used to produce metal oxide thin films, the number of studies that use ALD to produce metal chalcogenides thin films is limited because of a lack of appropriate precursors.[141] EALD is a relatively new, epitaxial deposition method with several advantages compared to traditional ALD, including (i) an ambient deposition environment, (ii) easy deposition control, (iii) easily made precursors, and (iv) low raw material waste.[142] EALD applies underpotential deposition (UPD) technology, which is less aggressive than the bulk reaction potential, to realize a self-limiting reaction (SLR). SLRs are reactions where only heterogeneous atoms can react with the material surface, and thus guarantees material growth on the atomic level.[143] To date, most studies are still investigating EALD CdS on Au or Ag substrates to obtain large, conformal surface areas.[143, 144] For actual applications, low cost substrates are, however, preferred. For example, fluorine-doped tin oxide (FTO) is such a substrate, it is a transparent,

conductive polycrystalline material that is widely used in the PV industry. This motivates a study of EALD CdS on FTO substrates. However, it is known that FTO substrates have several disadvantages compared to freshly cleaved Au and Ag substrates, such as a large surface roughness and random crystal orientations of the ITO surface. To overcome these limitations, a passivation strategy could be used to “fix” the defects in the EALD CdS thin film. We hypothesize that the ligands will “fill-in” the CdS domain borders, preventing voids and prolonging the carrier lifetime, and thus enhancing the PEC efficiency and improving the photo-stability (Figure 36).

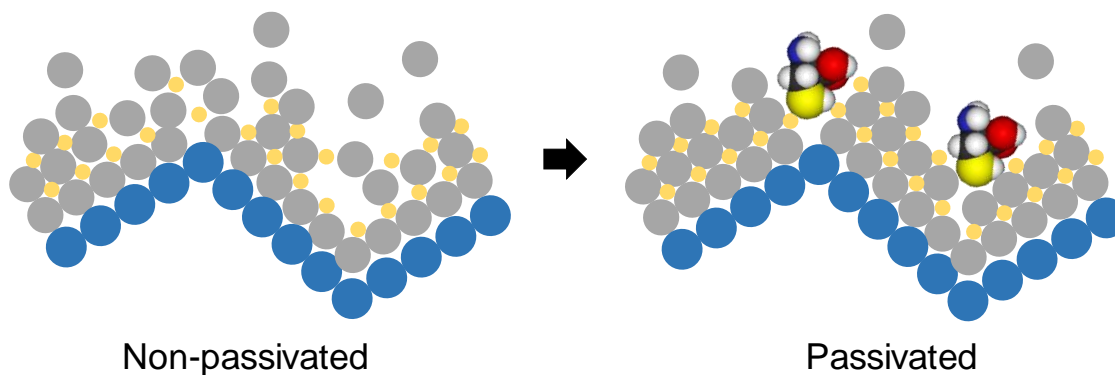


**Figure 37:** Schematic showing the proposed ligand passivation effect of the EALD CdS thin film. The blue dots represent tin (Sn) atoms, gray dots represent Cd atoms, and yellow dots represent S atoms. Cystein molecules are represented by molecular models. Without ligand passivation, voids will appear at the ridges (left).

## **Appendix A: Experimental Details**

### ***A.1 Sample preparation methods***

#### **A.1.1 CdS precipitation**

For a 500 ml culture (precipitating ~ 40 mg CdS), an isolated *E. coli* colony is taken from an agar plate and inserted into 5 ml of Miller's LB broth containing 75 mg/mL carbenicillin and shaken for 24 hours in a 37 °C incubator. After growth, the 5 ml bacterial suspension is mixed with 500 ml modified M9 medium containing 75 mg/mL carbenicillin, 0.2 mM K<sub>2</sub>SO<sub>4</sub>, 100 μM IPTG, and 1 mM cysteine. This 500 mL culture is subsequently shaken for a total of 24 hrs, however after 10 hrs of growth, CdCl<sub>2</sub> is added to the culture to a final concentration of 0.2 mM. After 24 hrs of growth yellow precipitate (CdS) is formed and falls out of solution.

To harvest the CdS, the medium with CdS is centrifuged at 2800 rpm for 20 min to isolate the solid material from the medium. The solid material is then suspended into 5 ml QIAGEN P2 buffer and 5 ml deionized (DI) water simultaneously. The new mixture is sonicated for 20 min to ensure a fully lysed bacterial culture. Then the bacterial debris (suspended in the buffer) is removed by centrifuging at 14000 rpm for 15 min. To further remove the buffer from the CdS NPs, we add DI water followed by another round of centrifugation. Finally, the CdS NPs are resuspended into DI water and stored in a plastic tube covered with foil to avoid light exposure, at 4 °C. Before use, the CdS NPs are resuspended by shaking for 1 min.

### **A.1.2 Bacterially precipitated CdS nanoparticle (BAC CdS NP) electrode preparation**

40  $\mu\text{l}$  of CdS (52.8  $\mu\text{g}$ ) suspension are drop casted on cleaned 1.27 cm  $\times$  1.27 cm ITO (703192 ALDRICH) glass slides and dried in the chemical hood overnight at room temperature ( $\sim 25$   $^{\circ}\text{C}$ ), while being covered with aluminum foil to avoid light exposure. The CdS covers only  $\sim 2/3$  of the total ITO glass area. After  $\sim 8$  hr drying in the chemical hood, the CdS/ITO sample is ready to be used in the assembly of the test electrode. To this end,  $1/3$  of the ITO that is not covered by CdS, is covered by an indium gallium (InGa, liquid metal) layer, and a flat-end copper (Cu) wire, connecting to the InGa layer, fixed in place with Epoxy resin. The copper wire is isolated from the electrolyte solution with a glass tube that is also connected to the Cu/InGa connection with Epoxy. For the CBD CdS control sample, an amount of CdS (52.8  $\mu\text{g}$ ) equivalent to that used in the preparation of the BAC CdS NP thin film is drop-casted onto a cleaned ITO glass substrate. After drying, the electrode preparation follows the procedure described above for the BAC CdS NPs.

### **A.1.3 Bacterially precipitated non-cysteine CdS NP preparation**

As described above in the CdS precipitation section, for a 100 ml culture, the process of growing *E. coli* culture is the same. 1 ml bacterial suspension is mixed with

100 ml modified M9 medium containing 75 mg/ml carbenicillin, 0.2 mM  $K_2SO_4$ , and 100  $\mu$ M IPTG. This 100 ml culture is shaken for a total of 24 hrs, and after 10 hrs of growth, 0.2 mM  $CdCl_2$  and 1mM  $Na_2S$ , which is the same amount of cysteine (molecular), is added to the culture. After 24 hrs of growth, yellow precipitate (CdS) is formed. The CdS NP harvest process is the same as that described above in the CdS precipitation section.

#### **A.1.4 Chemically synthesized cysteine capped CdS NP preparation**

To chemically synthesize cysteine capped CdS NPs, we followed a protocol from the literature.[126] The entire precipitation process is carried out in DI water degassed by argon (Ar) for 30 min. Then, 0.3 mmol of  $CdCl_2$  is mixed with 1 mM L-cysteine HCl aqueous solution to form the cysteine-Cd complex. Then, the pH value of the complex solution is tuned to 8 by adding Tris buffer. Later, the complex solution is mixed with 0.06 to 0.3 mmol  $Na_2S$  aqueous solution to obtain a Cd:S atomic ratio in the range of 5:1 to 1:1. The particles' size could be controlled by the amount of  $Na_2S$  added to the complex solution. The particles are harvested by adding cold ethanol (0 °C) into the solution. The precipitate is separated from the solution by centrifuging at 700 rpm for 5 min. Then, the particles are resuspended into water, and drop casted onto silicon (Si) substrates for future characterization.

### **A.1.5 Chemically synthesized non-cysteine CdS NP preparation**

The synthesis process is similar to that for chemically synthesized cysteine CdS NPs (A.1.5). A 0.3 mM CdCl<sub>2</sub> solution is prepared with degassed DI water. After tuning the pH value with Tris buffer, 0.06 mmol Na<sub>2</sub>S solution is added to precipitated CdS. Although CdS can precipitate from the aqueous solution, we used the same harvesting protocol as described in the the cysteine CdS NP section.

### **A.1.6 Bacterially precipitated CdS NPs with different ligands**

To prepare R-Cd (R = cysteine, cysteamine, 3-mercaptopropanol, or 6-mercaptohexanoic acid) complexes, 1.2 mmol R and 3.0 ml Tris buffer (1 M) are dissolved in 26.8 ml DI water with rigorous stirring at 90 °C using a mineral oil bath. Then, 0.2 ml CdCl<sub>2</sub> (1M) aqueous solution is slowly added into the reaction container. Keep stirring for an additional 30 min, then the R-Cd complex precursor is ready for further use.

For a 100 ml culture (precipitating ~ 5 mg CdS), an isolated *E. coli* colony is taken from an agar plate and inserted into 1 ml of Miller's LB broth containing 75 mg/mL carbenicillin and shaken for 24 hours in a 37 °C incubator. After growth, the 1 ml bacterial suspension is mixed with 100 ml modified M9 medium containing 100 µl 75 mg/mL carbenicillin, 0.2 mM K<sub>2</sub>SO<sub>4</sub>, 100 µM IPTG, and 1 mM cysteine. This 100 ml culture is subsequently shaken for a total of 24 hrs, however after 10 hrs of growth, add

3 ml prepared R-Cd complex into the culture (final concentration of Cd = 0.2 mM). After 24 hrs of growth yellow precipitate (CdS) is formed and falls out of solution.

To harvest the CdS, the medium with CdS is centrifuged at 2000 rcf for 20 min to isolate the solid material from the medium. The solid material is then suspended into 5 ml QIAGEN P2 buffer and 5 ml deionized (DI) water simultaneously. The new mixture is sonicated for 20 min to ensure a fully lysed bacterial culture. Then the bacterial debris (suspended in the buffer) is removed by centrifuging at 15000 rcf for 15 min. To further remove the buffer from the CdS NPs, we add DI water followed by another round of centrifugation. Finally, the CdS NPs are resuspended into DI water and stored in a plastic tube covered with foil to avoid light exposure, at 4 °C. Before use, the CdS NPs are resuspended by shaking for 1 min.

### **A.1.7 Hybrid electrode assembly**

For the fabrication of a photo-charged capacitor electrode, the BAC CdS is drop-casted onto a cleaned ITO glass substrate using the same procedure as described for PEC measurements (see section A.1.3).

**PVA-electrolyte gel preparation.** 3 g PVA powder (MW 146000 - 186000) (Sigma Aldrich, USA) is dissolved in 30 ml DI water and heated at 90 °C for 1 hr with vigorous stirring. After cooling the solution to room temperature (25 °C), the PVA crosslinked

into a hydrogel. A 1 M NaCl aqueous solution was prepared separately as the electrolyte.

**Preparation of a reduced graphene oxide (RGO) sheet.** We followed a previously published procedure.[145] 10 ml of highly concentrated graphene oxide (GO) solution (0.6 mg/ml) (Graphene Supermarket, USA) is transferred into 90 ml DI water. Then 0.2 ml hydrazine monohydrate (35% in aqueous solution) and 0.35 ml ammonia (27.5% wt. % in aqueous solution) are added to the suspension, and the mixture is heated to 95 °C for 2 hrs with vigorous stirring. After the mixture is air-cooled, the black RGO suspension is ready for deposition. 30 ml of the RGO suspension are mixed with 200 ml DI water, and filtered through a nitrocellulose filter membrane (0.05 µm pore size, 47 mm in diameter, EMD Millipore, USA). After the filtration, the RGO sheet formed on the filter membrane.

### **A.1.8 Chemically synthesized CdS NPs passivated with different ligands**

To prepare R-Cd (R = cysteine, cysteamine, 3-mercaptopropanol, or 6-mercaptophexanoic acid) complexes, 1.0 mmol R and 2.0 ml Tris buffer (1 M) are dissolved in 26.8 ml DI water (purged with N<sub>2</sub> to degas for 30 min before synthesis) with rigorous stirring at 90 °C using a mineral oil bath. Then, 0.33 ml CdCl<sub>2</sub> (1M) aqueous solution is slowly added into the reaction container. Keep stirring for 30 min, then add

0.66 ml, 1.98 ml, 3.3 ml, or 6.6 ml Na<sub>2</sub>S (0.1M) to precipitate CdS NPs with Cd:S atomic ratio of 5:1, 5:3, 5:5, and 5:10, respectively.

To harvest CdS NPs from aqueous solutions, add a large amount of ethanol (water to ethanol volume can be 1 to 4) and shake the solution. Keep the ethanol water solution in a 4°C fridge for overnight, centrifuge down the precipitate at 5000 rcf for 10 min, then lyophilize for 24 hrs to get dry particles. Note that 3-mercaptopropanol capped CdS NPs are very hard to precipitate even using ethanol. The only way to obtain the NP precipitation is to add excess amount of Na<sub>2</sub>S (Cd : S atomic ratio = 1 : 10).

### **A.1.9 Electrochemical atomic layer deposition (EALD) CdS thin film preparation**

The EALD CdS thin film is deposited on thoroughly cleaned FTO glass substrates. The cleaning procedure of the FTO glass involves sonication for 5 mins in each, acetone, ethanol, and DI water, and then oxygen plasma cleaning (HARRICK PLASMA PDC-32G) at medium level for 2 min. The EC electrode is prepared using the same procedure as described in section A.1.3, CdS EC/PEC measurement electrode preparation.

The precursor solutions are all made with degassed DI water (pH = 5.5, Ar degas for 30 min). 0.5 mM CdCl<sub>2</sub> and 1.0 mM Na<sub>2</sub>S solution are prepared before depositing. The EALD is conducted in two three-electrode-EC cells. First, the FTO electrode is immersed into the CdCl<sub>2</sub> solution, and we apply a -0.5 V (vs. Ag/AgCl) voltage for 60 s

to deposit a layer of Cd. Then, the electrode is taken out from the Cd solution and rinsed into pure water before being immersed into Na<sub>2</sub>S solution. While it is in the Na<sub>2</sub>S solution, we apply a -0.5 V (vs. Hg/HgO) voltage for 60 s to deposit a layer of S. Then, the electrode is taken out and rinsed into pure water to finish one cycle of deposition before immersing back into the CdCl<sub>2</sub> solution. By controlling the total cycle number the thickness of the EALD CdS thin films can be adjusted.

EALD cysteine passivated CdS thin film preparation. In preliminary study, the FTO electrode with 5 layers of EALD CdS is immersed in 0.5 mM L-cysteine HCl aqueous solution for 5 min to passivate the surface. In the future study, new CdS layers will be deposited after immersing into the cysteine solution. We currently plan to passivate the defect every 5 cycles.

## ***A.2 Characterization Methods***

### **A.2.1 Scanning electron microscopy (SEM)/Electron dispersive X-ray spectroscopy (EDX)**

For SEM/EDX analysis, 40 µl of the CdS suspension is drop casted onto a cleaned, 1.27 cm × 1.27 cm silicon wafer chip and dried in the chemical hood overnight at room temperature (~ 25 °C), covered with aluminum foil to avoid light exposure. A FEI XL30 SEM-FEG and a FEI XL30 ESEM with Bruker XFlash 4010 EDS detector are used for SEM/EDX characterization. For SEM imaging, the acceleration voltage is set to 20 kV and the working distance is set to 15 mm. For elemental composition

measurements using EDX, the working distance is set to 12 mm, with a magnification of 800×. To obtain representative values for the CdS concentration, we averaged the measurements from three randomly chosen points for each of the 5 different samples.

### **A.2.2 Transmission electron microscopy (TEM)**

For TEM imaging, the biosynthetic CdS samples are grown and purified as described above, however, the solution is diluted further in DI water (10-fold) and 2  $\mu$ l of the solution is drop casted onto Formvar-coated, Cu TEM grids. The samples are then covered in aluminum foil and allowed to air-dry overnight. TEM images are acquired on a FEI CM12 with 200 kV accelerating voltage. Particle diameters are determined by manual measurement on 10 TEM images using ImageJ.[72]

### **A.2.3 X-ray diffraction (XRD) analysis**

50  $\mu$ l of the CdS suspension are drop casted on a cleaned 1.27 cm  $\times$  2.54 cm glass slide and heat treated at 450 °C for 15 min in a tube furnace under ambient conditions. XRD measurements are performed on a Panalytical X'Pert PRO MRD HR X-Ray Diffraction System, with 1/2° divergence slit, a step size of 0.02°, and an acquisition time/step of 0.75 s. The pre-set count is 10000, and the scan angles ranged from 20° to 60° (2 $\theta$ ). The diffraction spectra are smoothed and peaks are fitted manually using OriginPro 8.5 software.

#### **A.2.4 UV-vis spectroscopy**

The samples used for UV-vis spectral analysis are identical to those for SEM and EDS experiments. A Shimadzu UV-3600 UV-Vis-NIR Spectrophotometer with a reflectance attachment is used to test the absorption performance of the BAC CdS NPs. During the measurement, a medium scan speed is used with a 1 nm sampling interval and a 0.5 nm slit width. After background subtraction, spectral intensities are normalized. The onset of the absorbance is determined via MATLAB, by fitting the spectrum to the left and right of the absorbance region by straight lines, and calculating the intercept of the lines.[79]

#### **A.2.5 Methyl orange (MO) molecule photodegradation.**

50  $\mu$ l condensed CdS (405  $\mu$ g), 3 ml MO DI water solution (0.01g/L), and 20  $\mu$ l Na<sub>2</sub>S (0.5 M) are mixed in 5 ml glass vials. Same amount of CBD CdS (405  $\mu$ g) is also mixed with same MO and Na<sub>2</sub>S solution. Five such vials of condensed CdS/MO and CBD CdS/MO mixture are prepared and wrapped with aluminum foil, as well as 2 vials of control sample without CdS. Started from 0 hr, the bacterial precipitated CdS/MO samples, the CBD CdS/MO samples and the control samples are irradiated with 450 W output solar simulator (Sol2A Class ABA), and every 0.5 hr one bacterial precipitated CdS/MO and one CBD CdS/MO sample are taken out from the solar simulator from 0 hr

to the end of 2 hr. After irradiation, all the samples are centrifuged at 8,000 rpm for 5 min to remove the residual sedimentary from the solution. Then the samples are objected to UV-vis test. The ratio of the absorbance peak height to the peak height of the original MO indicated the percentage of MO remained in the solution.

### **A.2.6 Electrochemical measurements**

**Photoelectrochemical (PEC) tests.** A Bio Logic SP-200 electrochemistry workstation is used for PEC testing. In these tests, a 150 W Xenon lamp (DRIEL-66001 with 68805 universal power supply) is used as the light source, with a wavelength filter simulating sunlight. The distance between the light source and the working electrode surface is around 15 cm to ensure a 100 mW/cm<sup>2</sup> light intensity (1 sun) in the electrochemical cell. A Platinum Counter Electrode (23 cm, by BAS Inc., Cat. No. 012961), Ag/AgCl reference electrode (012167 RE-1B Reference Electrode, by ALS Co., Ltd), and the CdS working electrode (or control ITO working electrode) are assembled as a three-electrode testing system. The electrolyte is 0.5 M Na<sub>2</sub>SO<sub>4</sub> dissolved in DI water with pH = 6.8. All PEC tests are carried out at room temperature. Before testing, the electrolyte is perfused with nitrogen (N<sub>2</sub>) gas for 20 min, and during testing N<sub>2</sub> is continually bubbled into the electrolyte to minimize dissolved oxygen.

**EIS measurements.** A potentiostat equipped with a frequency response analyzer (Bio-logic SP-200) is used under potentiostatic conditions over a frequency range from

0.1 Hz to 200 kHz, using a 10 mV sinusoidal potential modulation. The potential range is from 0.4 to -1.0 V vs. Ag/AgCl. The selected potential is applied for 2 minutes to reach a steady state before the EIS measurements. The impedance parameters involved in the selected EIS equivalent circuit model are obtained by fitting the experimental data with EC-Lab software (Bio-Logic).

**Cyclic Voltammetry (CV) measurements.** The measurement potential range is set from -1.0 V to +0.5 V vs. Ag/AgCl with a sweep rate of 1 mV/s. Measurements are taken in both, dark and illuminated conditions.

**Transient photocurrent responses.** The transient photocurrent is measured at 0 V vs. open circuit potential (OCP) bias. During the test, the sample is intermittently irradiated with light every 60 s for a total of 300 s, and the corresponding current is measured for a total of 11 min. The electrode working area is calculated from optical images using ImageJ software, and is used to convert the measured current into current density. In addition, the specific current generated by both bacterially-precipitated (BAC) CdS and chemical bath deposited (CBD) CdS samples is calculated by dividing the measured current by the total sample weight (180  $\mu\text{g}$  for the BAC CdS NPs, and 103  $\mu\text{g}$  for the CBD CdS NPs).

### **A.2.7 Electrochemical measurements of the hybrid electrode**

The transient current, CV and EIS tests follow the procedure described in section A.2.5. For the OCP tests, measurements are recorded at every 10 mV (or every 0.5 s) for the first three steps (stabilization, photo-charging, and charge storage). For the first step, the OCP of the electrode is measured until it reaches a steady value. Once a steady-state OCP is obtained, the electrode is charged by illumination by 1 sun. After 90 s of charging, the light is turned off, and the OCP is measured for another 10 s. As the fourth step, a 0.9  $\mu\text{A}$  discharge current is applied until the OCP dropped back to 0 V.

### **A.2.8 Photoluminescence (PL) spectra measurements**

To measure the PL spectra, we test CdS NPs as solid thin films drop casted on Si substrates, or as NPs solutions, using Raman/PL measurement equipment (HORIBA JOBIN YVON LabRAM). The excitation wavelength is 442 nm (Kimmon He-Cd laser), the detection range is set from 445 nm to 800 nm, the acquire time was set as 3 s, the accumulation number was set as 5, and the RTD time was set as 1 s. When measuring the solid sample, we use the 100 $\times$  objective lens, and set the grating as 1800, the filter as 50%, and the slit as 100. When measuring the liquid sample, no lens is needed, and we set the grating as 1800, filter as 50% filter, and slit as 100. The PL spectra are plot with MATLAB.

### **A.2.9 Time resolved PL (TRPL) measurements**

To measure TRPL, we used a coherent Ti laser source (Sapphire 80 Mhz, 150 fs), and an avalanche photodetector (PMD, Micro Photon Device) with a time-correlated single photon counting module (PicoHarp 300, PicoQuant). The excitation wavelength is 450 nm. The laser pulse period is 12 ns, and we measure TRPL under different emission wavelengths or wavelength ranges. The sample used in TRPL measurements are the same used in PL measurements.

### **A.2.10 X-ray Photoelectron Spectroscopy measurements (including the cut-off energy measurement)**

CdS NPs are drop-casted onto precleaned Si substrate and air dried. The Kratos Axis Ultra X-ray Photoemission Spectrometer at Duke's Shared Materials Instrumentation Facility (SMiF) is used to conduct the measurement. We do 5 sweeps for region scans, with a step size of 0.1 eV, dwell time is automatically set by the system, from 259.7 ms to 425.5 ms. Pass energy is set to 160 Depending on the working condition of the instrument, SMiF staff will set it before measurements. For survey scans, we do 2 sweeps with a step size 1 eV and dwell time 200 ms. Pass energy is set to 160. For cut-off energy measurement, we do 5 sweeps with instrumental set up the same as region scans. However, the pass energy is set to 10 in order to obtain high accuracy energy onset.

### **A.2.11 Bacterially precipitation of CdS yield measurement**

We measure the mass of the precipitation to characterize the yield. First, we use bacteria culture to precipitate CdS NPs with i) pure CdCl<sub>2</sub> precursor (final concentration 0.2 mM and 2.0 mM), ii) extra cysteine (1.2 mM and 12 mM higher than the concentration used to precipitate CdS) and CdCl<sub>2</sub> (0.2 mM and 2.0 mM) separately added to the cell culture, and iii) pre-incubated cysteine-Cd complex (0.2 mM and 2.0 mM) to add to the cell culture. After harvesting (method see section A.1.1), the precipitation is lyophilized for 24 hr and the mass is measured on an electric scale. Each group is repeated for three times to obtain a statistical distribution.

In addition, control groups using the same biosynthesis procedure but i) only add DI water to replace CdCl<sub>2</sub> precursor, and ii) only add extra cysteine (1.2 mM and 12 mM higher than the concentration used to precipitate CdS) are also made, and the biomass is harvested and measured. The final CdS mass is determined by the difference in the mass of the three CdS precipitation groups and the control groups.

### **A.2.12 Cell viability measurements**

We plate the dilution of cultures and count the resulting colonies, which is a proxy for viable cell count. The experiment groups and control groups are made as described in section A.2.10. After precipitation and before harvesting the particles, these cultures are plated on Lysogeny Broth (LB) Agar plates containing 75 µg/ml

Carbenicillin with a dilution rate of 1×, 10×, 100×, 1,000×, 10,000×, 100,000×, and 1,000,000×. Each group is plated in replicates of 4 and were incubated at 37 °C for 24 hr and the number of colonies of 100,000×, and 1,000,000× dilution rates for each condition are counted manually.

### **A.2.13 Kelvin-Probe Force Microscopy (KPFM) for work function measurement**

KPFM was used to measure the work function. Bacterially precipitated CdS NPs with different ligands and chemically precipitated CdS NPs with different ligands were drop-casted onto precleaned Si substrates and air dried. The samples were stored in the nitrogen box in SMiF.

KPFM was conducted using Asylum 3D MFP (Asylum Research) and PtIr coated conductive AFM probe (BRUKER, SCM-PIT-V2,  $k = 3 \text{ N/m}$ ), and the measurement was conducted in a nitrogen environment with humidity ~10% RH. AFM tapping mode and Nap mode were used to obtain the height profile and contact potential difference (CPD) profile at the same time. When measuring the height profile, the scan size was set to  $5 \mu\text{m} \times 5 \mu\text{m}$  with a scan rate of 0.5 Hz. When measuring the CPD profile, the distance between the AFM tip to the sample was set to 10 nm (delta height), and the tip bias was set to 3V. The scan size was also  $5 \mu\text{m} \times 5 \mu\text{m}$  and the scan rate was 0.5 Hz. The work function of the AFM tip was determined through measurement on a cleaned, n-doped silicon substrate.

## **A.3 Data analysis processes**

### **A.3.1 XRD data analysis**

We used the X'Pert Data Collector program to analyze XRD diffraction spectra. We first smooth the raw data a "Degree of smoothing" = 30; then subtract the background with "Peak base width" = 2; searching peaks with "Peak base width" = 10 using the "minimum 2<sup>nd</sup> derivative" method; searching and matching peaks with "allow pattern shift", "auto residue", "demote unmatched strong", "multiphase", "match intensity" and "identify" options checked.

Once pre-processed, we plot the spectra with OriginPro 8.5. The spectrum is smoothed by 30 degree, and is shifted up 0.15° along the 2θ axis to match published reference data. Peaks were fitted automatically by OriginPro 8.5.

### **A.3.2 EDS data analysis**

To obtain the elemental percentage, we subtracted the silicon (Si) component from the raw data and renormalized the atomic percentage. The reason for removing Si from the raw data is that our sample substrate is Si, so it does not represent any impurity.

### **A.3.3 UV-vis data analysis**

To analyze UV-vis data, we normalized the absorption spectra by re-defining the intensity of the lowest point as 0 and the highest point as 1. Then we used a MATLAB code to fit the data to both sides of the absorbance wavelength with straight lines, find the intercept to then find the absorbance onset. Additionally, we used the Tauc relation to plot the normalized data in form of a Tauc plot, and to fit the linear part of the curve and act the intercept of the straight line and x axis as the bandgap.

### **A.3.4 TEM data analysis**

TEM images were analyzed using Image J. We calibrated the measurement software by drawing a straight line of the same length as the scale bar and “set the scale”. When measuring d-spacing, we measured the distance across 10 crystal planes and calculated the average distance between lattice planes. By comparing the measured d-spacing to reported d-spacings of different lattice planes of CdS, we identify lattice planes.

### **A.3.5 XPS data analysis**

We analyzed XPS data using the Casa XPS program, adopting the procedure from our previous work.[37] Briefly, the raw binding energy data is shifted to match the C1s peak to a binding energy of 284.5 eV (binding energy). Then, the Cd doublet peaks

are fitted to Cd(S) and Cd(O) components. The fitting parameters used are: Cd(O) and Cd(S)  $3d_{5/2}$  peak positions are set to 404.62 eV and 405.18 eV, respectively; the  $3d_{3/2}$  peaks of Cd(O) and Cd(S) are set 6.74 eV higher than the  $3d_{5/2}$  peak; the area ratio between  $3d_{5/2}$  and  $3d_{3/2}$  is set to 3:2. The fitting process is iterated until the result converges.

### **A.3.6 Electrochemical data analysis**

Transient current data were interpreted by using the raw data divided by the amount of CdS (in weight) obtained from the EDS analysis. The amount of CdS was determined by weighing the amount of residual dry solid after deposition of 400  $\mu$ l of an aqueous CdS suspension. Then, we combine purity information obtained from the EDS analysis to know the CdS concentration from the aqueous suspension. We used this concentration to estimate the amount of CdS that is coated onto PEC samples.

Cyclic voltammetry data was analyzed by using the 2<sup>nd</sup> cycle of the CV measurements. An important reason for using the 2<sup>nd</sup> cycle is that the 1<sup>st</sup> cycle is conducted to stabilize the system.

EIS measurements are analyzed as follow: the raw data is presented as a series of Nyquist plots under different bias. Each Nyquist plots is fitted with the equivalent circuit shown in B.2 to obtain the space charge capacitance ( $C_{sc}$ ) using the quantitative analysis function in EC-Lab program.

### **A.3.7 PL/TRPL data analysis**

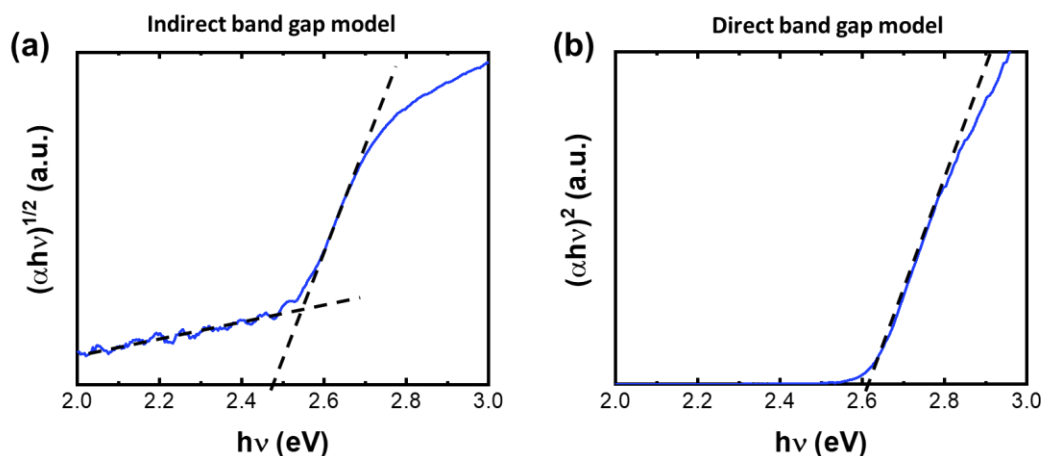
PL spectra were normalized following the same strategy as described in A3.3, UV-vis data analysis. Briefly, TRPL data were normalized and plotted within one 12 ns laser pulse cycle. The highest point of the intensity (at 0 ns after the laser pulse hits the sample) is defined as 1 and all following data points are normalized as a percentage of the value of the highest point, representing the proportion of luminescence that remains as a function of time.

### **A.3.8 KPFM data analysis**

The KPFM potential profile data were analyzed without modification. The mean and standard deviation of the entire image (each pixel value) were determined to obtain the contact potential difference (CPD) distribution.

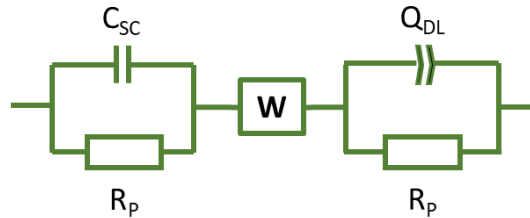
## Appendix B: Supplementary information

### B.1 Tauc plots for the determination of the CdS bandgap



In a Tauc plot the Tauc relation, *i.e.*,  $(\alpha h\nu)^{1/r}$  is plotted as a function of  $h\nu$ . The intercept of the fitted line with the x-axis is a measure of the bandgap. In this plot,  $\alpha$  is the normalized absorption value determined from UV-vis measurements,  $h\nu$  is the photon energy, and  $r$  is a coefficient depending on the nature of the material. For indirect bandgap semiconductors,  $r = 2$ , and for direct bandgap semiconductors,  $r = 0.5$ . Figure B.1 shows the Tauc plot of biosynthetic CdS NPs using the (a) indirect bandgap model and (b) the direct bandgap model. CdS is a direct bandgap semiconductor, and evaluating the bandgap using the direct bandgap Tauc model yields a value of 2.6 eV. This value is in good agreement with published bandgap values for CdS nanoparticles.

## B.2 equivalent circuit of the BAC CdS



$C_{SC}$ : Space charge layer capacitance

$R_P$ : Polarization resistance

$W$ : Warburg element

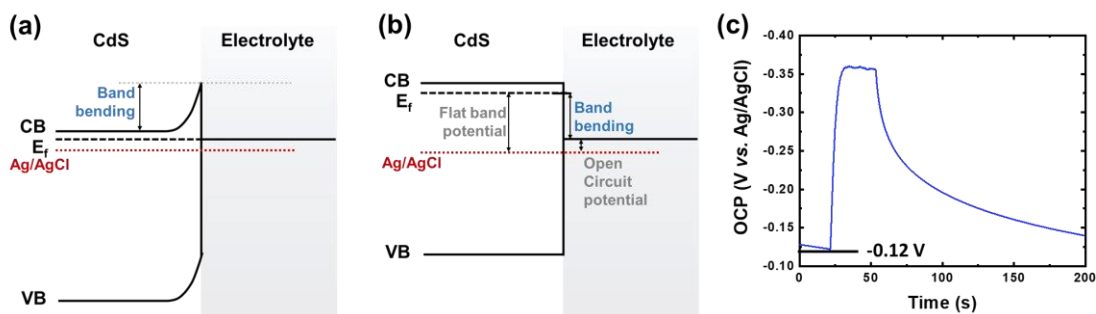
$Q_{DL}$ : Double layer constant phase element

Equivalent circuit modelling is commonly used to interpret results from EIS measurements. For biosynthetic CdS NPs, we model the CdS-electrolyte interface as a space charge layer capacitor ( $C_{SC}$ ) and a polarization resistance ( $R_P$ ) in parallel, connected in series with a Warburg element ( $W$ ) and a constant phase element for the electrolyte double layer ( $Q_{DL}$ ) connected in parallel with the polarization resistance ( $R_P$ ).

We model the interface as three components: i) the  $C_{SC} // R_P$  part represents the CdS space charge layer, ii) the  $W$  part represents the capping ligand and other organic compounds surrounding the CdS, which is considered as a diffusion affected charge transport element (Note that when modelling CdS NPs without ligand passivation (i.e., groups 2 and 4 in Chapter 3), the  $W$  part is removed from the equivalent circuit.) iii) the  $Q_{DL} // R_P$  part represents the electrolyte double layer that is closest to the CdS-electrolyte interface. Due to the diffusion and polarization effects from the passivating ligands, this

region cannot be modeled as an ideal capacitor. Thus, a Q element other than a C element is used for modeling.

### B.3 the estimation of band bending



In (photo)electrochemistry, the band bending of a semiconductor can be estimated using OCP measurements and flat band potential measurements. Under equilibrium conditions, the Fermi energy level aligns with the chemical potential of the electrolyte at the CdS-electrolyte interface, bending the energy band of CdS NPs downward (Figure B.3(a)). In flat band potential measurements, the bias (*vs.* Ag/AgCl, the reference electrode) is added so that the energy band bending is compensated (Figure B.3(b)). Thus, the measured flat band potential indicates band bending. To determine the extent of band bending, we measured the OCP in the dark, thus determining the energy difference between the electrolyte chemical potential and the reference electrode (Figure B.3(c)). As a result, the difference between the flat band potential (*vs.* Ag/AgCl) and the OCP (*vs.* Ag/AgCl) is the band bending.

**B.4 CBD CdS cannot be made into a hybrid device due to its poor dispersion**

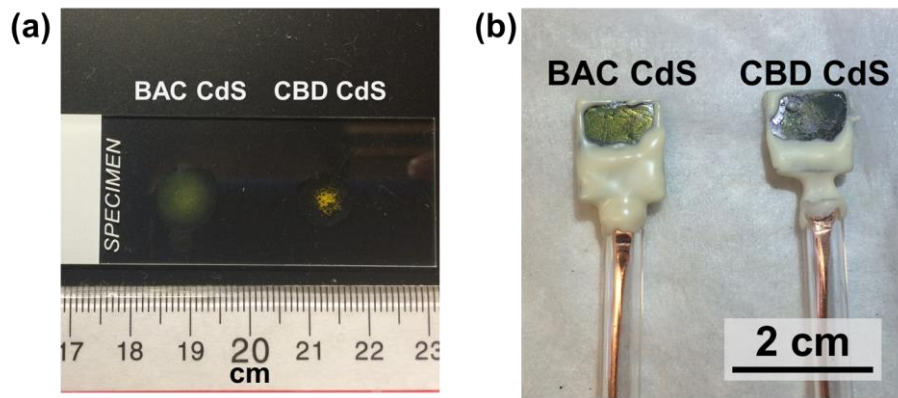
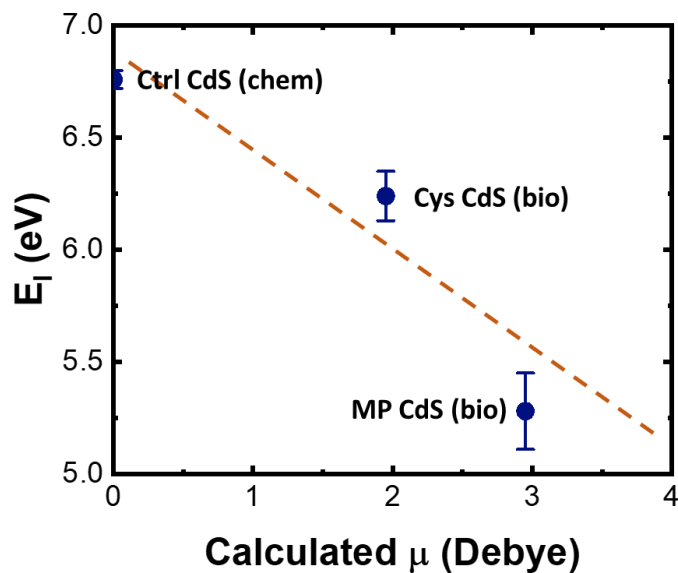


Figure B.4 (a) shows that BAC CdS NPs disperse more uniformly in a drop of water than CBD CdS with no ligand passivation, which tend to agglomerate. Agglomeration prevents CBD CdS from forming a continuous film in dropcasting, and thus prohibits fabrication of a hybrid device (Figure B.4(b)). Direct contact of electrolyte gel with the ITO substrate will lead to recombination of the photogenerated electrons and holes, killing the performance of the device.

### B.5 Cd and S atomic ratio from XPS survey scans

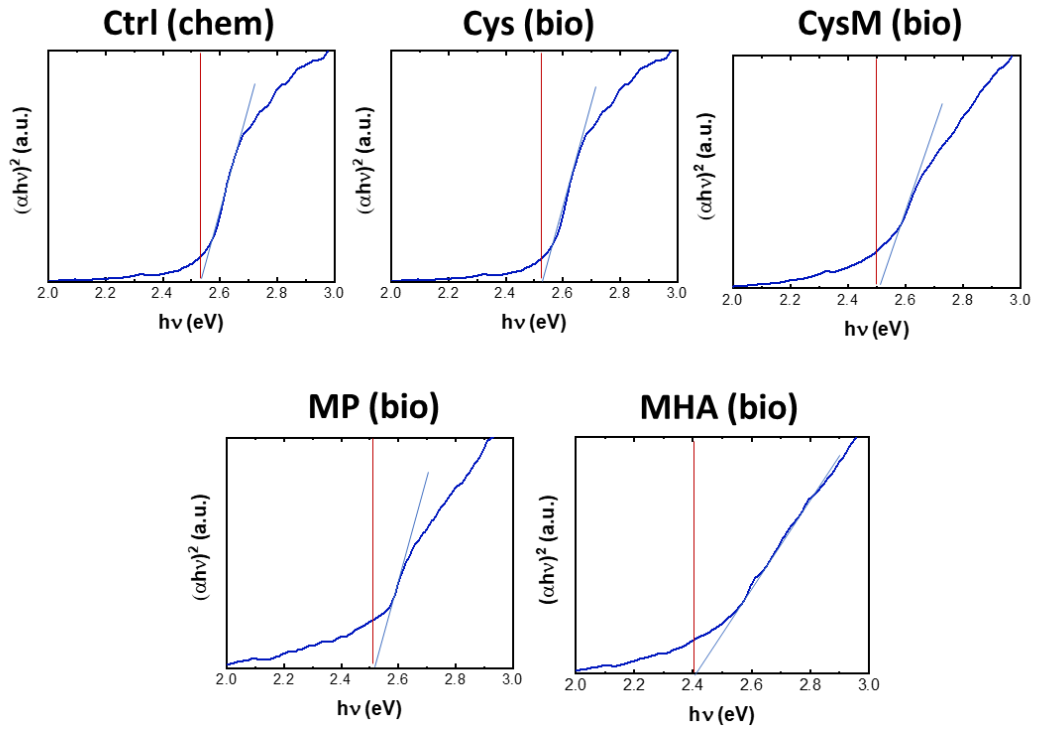
Biosynthetic CdS	Cd atm%	S atm%
Ctrl CdS	20.7	15.7
Cys CdS	20.3	16.5
CysM CdS	18.7	16.0
MP CdS	14.7	13.4
MHA CdS	12.4	10.3

### B.6 The relationship between dipole moments and ionization energy for polarized ligand capped CdS NPs



For polarized ligands, cysteine and mercaptopropanol, the dipole moment and the ionization energy correlate, which is also reported in the literature.[134]

## B.7 Tauc plots for bandgap fitting for CdS with different ligands



## Bibliography

- [1] [1] Rajamathi M, Seshadri R. Oxide and chalcogenide nanoparticles from hydrothermal/solvothermal reactions. *Current Opinion in Solid State and Materials Science*. 2002 (6) 337-345.
- [2] Kovalenko MV, Scheele M, Talapin DV. Colloidal Nanocrystals with Molecular Metal Chalcogenide Surface Ligands. *Science*. 2009 (324) 1417-1420.
- [3] Fernando A, Weerawardene KLDM, Karimova NV, Aikens CM. Quantum Mechanical Studies of Large Metal, Metal Oxide, and Metal Chalcogenide Nanoparticles and Clusters. *Chemical Reviews*. 2015 (115) 6112-6216.
- [4] Narayanan R, El-Sayed MA. Catalysis with Transition Metal Nanoparticles in Colloidal Solution: Nanoparticle Shape Dependence and Stability. *The Journal of Physical Chemistry B*. 2005 (109) 12663-12676.
- [5] Beletskaya IP, Ananikov VP. Transition-Metal-Catalyzed C-S, C-Se, and C-Te Bond Formation via Cross-Coupling and Atom-Economic Addition Reactions. *Chemical Reviews*. 2011 (111) 1596-1636.
- [6] Özel F, Sarılmaz A, İstanbullu B, Aljabour A, Kuş M, Sönmezoglu S. Penternary chalcogenides nanocrystals as catalytic materials for efficient counter electrodes in dye-synthesized solar cells. *Scientific Reports*. 2016 (6) 29207.
- [7] Wang D-S, Zheng W, Hao C-H, Peng Q, Li Y-D. A Synthetic Method for Transition-Metal Chalcogenide Nanocrystals. *Chemistry – A European Journal*. 2009 (15) 1870-1875.
- [8] Jeong S, Yoo D, Jang J-t, Kim M, Cheon J. Well-Defined Colloidal 2-D Layered Transition-Metal Chalcogenide Nanocrystals via Generalized Synthetic Protocols. *Journal of the American Chemical Society*. 2012 (134) 18233-18236.
- [9] da Costa JP, Girão AV, Trindade T, Costa MC, Duarte A, Rocha-Santos T. Biological synthesis of nanosized sulfide semiconductors: current status and future prospects. *Applied Microbiology and Biotechnology*. 2016 (100) 8283-8302.
- [10] Jacob JM, Lens PNL, Balakrishnan RM. Microbial synthesis of chalcogenide semiconductor nanoparticles: a review. *Microbial Biotechnology*. 2016 (9) 11-21.
- [11] Xu W, Ye P, Iocozzia J, Zhang H, Yuan Y, Lin Z. A general and rapid approach to crystalline metal sulfide nanoparticle synthesis for photocatalytic H<sub>2</sub> generation. *Journal of Materials Chemistry A*. 2017 (5) 21669-21673.
- [12] Ana C, Guillermo RC. Bionanoparticles, a green nanochemistry approach. *Electronic Journal of Biotechnology*; 2013 (16).

- [13] Sastry M, Ahmad A, Islam Khan M, Kumar R. Biosynthesis of metal nanoparticles using fungi and actinomycete. 2003 (85) 162-170.
- [14] Iravani S. Green synthesis of metal nanoparticles using plants. *Green Chemistry*. 2011 (13) 2638-2650.
- [15] Faramarzi MA, Sadighi A. Insights into biogenic and chemical production of inorganic nanomaterials and nanostructures. *Advances in Colloid and Interface Science*. 2013 (189-190) 1-20.
- [16] Korbekandi H, Iravani S, Abbasi S. Production of nanoparticles using organisms. *Critical Reviews in Biotechnology*. 2009 (29) 279-306.
- [17] Rice MK, Ruder WC. Creating biological nanomaterials using synthetic biology. *Science and Technology of Advanced Materials*. 2014 (15) 014401.
- [18] Raouf Hosseini M, Nasiri Sarvi M. Recent achievements in the microbial synthesis of semiconductor metal sulfide nanoparticles. *Materials Science in Semiconductor Processing*. 2015 (40) 293-301.
- [19] Dameron CT, Reese RN, Mehra RK, Kortan AR, Carroll PJ, Steigerwald ML, *et al.* Biosynthesis of cadmium sulphide quantum semiconductor crystallites. *Nature*. 1989 (338) 596-597.
- [20] Stürzenbaum SR, Höckner M, Panneerselvam A, Levitt J, Bouillard JS, Taniguchi S, *et al.* Biosynthesis of luminescent quantum dots in an earthworm. *Nature Nanotechnology*. 2012 (8) 57-60.
- [21] Syed A, Ahmad A. Extracellular biosynthesis of CdTe quantum dots by the fungus *Fusarium oxysporum* and their anti-bacterial activity. *Spectrochimica Acta Part A: Molecular and Biomolecular Spectroscopy*. 2013 (106) 41-47.
- [22] Wang C, Lum A, Ozuna S, Clark D, Keasling J. Aerobic sulfide production and cadmium precipitation by *Escherichia coli* expressing the *Treponema denticola* cysteine desulfhydrase gene. *Applied Microbiology and Biotechnology*. 2001 (56) 425-430.
- [23] Sweeney RY, Mao C, Gao X, Burt JL, Belcher AM, Georgiou G, *et al.* Bacterial Biosynthesis of Cadmium Sulfide Nanocrystals. *Chemistry & Biology*. 2004 (11) 1553-1559.
- [24] Suresh AK, Doktycz MJ, Wang W, Moon J-W, Gu B, Meyer HM, *et al.* Monodispersed biocompatible silver sulfide nanoparticles: Facile extracellular biosynthesis using the  $\gamma$ -proteobacterium, *Shewanella oneidensis*. *Acta Biomaterialia*. 2011 (7) 4253-4258.

- [25] Choi Y, Park TJ, Lee DC, Lee SY. Recombinant *Escherichia coli* as a biofactory for various single- and multi-element nanomaterials. *Proceedings of the National Academy of Sciences*. 2018 (115) 5944-5949.
- [26] Ulloa G, Collao B, Araneda M, Escobar B, Álvarez S, Bravo D, *et al.* Use of acidophilic bacteria of the genus *Acidithiobacillus* to biosynthesize CdS fluorescent nanoparticles (quantum dots) with high tolerance to acidic pH. *Enzyme and Microbial Technology*. 2016 (95) 217-224.
- [27] Kang SH, Bozhilov KN, Myung NV, Mulchandani A, Chen W. Microbial Synthesis of CdS Nanocrystals in Genetically Engineered *E. coli*. *Angewandte Chemie International Edition*. 2008 (47) 5186-5189.
- [28] Al-Shalabi Z, Stevens-Kalceff MA, Doran PM. Application of *Solanum lycopersicum* (tomato) hairy roots for production of passivated CdS nanocrystals with quantum dot properties. *Biochemical Engineering Journal*. 2014 (84) 36-44.
- [29] Venegas FA, Saona LA, Monrás JP, Órdenes-Aenishanslins N, Giordana MF, Ulloa G, *et al.* Biological phosphorylated molecules participate in the biomimetic and biological synthesis of cadmium sulphide quantum dots by promoting H<sub>2</sub>S release from cellular thiols. *RSC Advances*. 2017 (7) 40270-40278.
- [30] Ulloa G, Quezada CP, Araneda M, Escobar B, Fuentes E, Álvarez SA, *et al.* Phosphate Favors the Biosynthesis of CdS Quantum Dots in *Acidithiobacillus thiooxidans* ATCC 19703 by Improving Metal Uptake and Tolerance. *Frontiers in Microbiology*. 2018 (9) 234.
- [31] Liu XW, Jia; Yue, Lei; Xin, Baoping; Chen, Shi; Dai, Jiulan; Wang, Renqing; Wang, Yutao. Biosynthesis of high-purity  $\gamma$ -MnS nanoparticle by newly isolated *Clostridiaceae* sp. and its properties characterization. *Bioprocess and biosystems engineering*. 2014 (38) 219-227.
- [32] Kaviya S. Size dependent ratiometric detection of Pb (II) ions in aqueous solution by light emitting biogenic CdS NPs. *Journal of Luminescence*. 2018 (195) 209-215.
- [33] Bao H, Lu Z, Cui X, Qiao Y, Guo J, Anderson JM, *et al.* Extracellular microbial synthesis of biocompatible CdTe quantum dots. *Acta Biomaterialia*. 2010 (6) 3534-3541.
- [34] Fellowes JW, Patrick RAD, Lloyd JR, Charnock JM, Coker VS, Mosselmans JFW, *et al.* Ex situ formation of metal selenide quantum dots using bacterially derived selenide precursors. *Nanotechnology*. 2013 (24) 145603.
- [35] Gallardo C, Monrás JP, Plaza DO, Collao B, Saona LA, Durán-Toro V, *et al.* Low-temperature biosynthesis of fluorescent semiconductor nanoparticles (CdS) by

- oxidative stress resistant Antarctic bacteria. *Journal of Biotechnology*. 2014 (187) 108-115.
- [36] Yang Z, Lu L, Berard VF, He Q, Kiely CJ, Berger BW, *et al.* Biomanufacturing of CdS quantum dots. *Green Chemistry*. 2015 (17) 3775-3782.
- [37] Marusak KE, Feng Y, Eben CF, Payne ST, Cao Y, You L, *et al.* Cadmium sulphide quantum dots with tunable electronic properties by bacterial precipitation. *RSC Advances*. 2016 (6) 76158-76166.
- [38] Dunleavy R, Lu L, Kiely CJ, McIntosh S, Berger BW. Single-enzyme biomineralization of cadmium sulfide nanocrystals with controlled optical properties. *Proceedings of the National Academy of Sciences*. 2016 (113) 5275-5280.
- [39] Abu A. Ansary \* IUaMIK. Biomimetic Synthesis of CdSe Nanoparticles with Potential Bioimaging Applications. *International Journal of Pharmaceutical Sciences and Research*. 2017 (8) 2526-2532.
- [40] Murray AJ, Roussel J, Rolley J, Woodhall F, Mikheenko IP, Johnson DB, *et al.* Biosynthesis of zinc sulfide quantum dots using waste off-gas from a metal bioremediation process. *RSC Advances*. 2017 (7) 21484-21491.
- [41] Moon J-W, Ivanov IN, Duty CE, Love LJ, Rondinone AJ, Wang W, *et al.* Scalable economic extracellular synthesis of CdS nanostructured particles by a non-pathogenic thermophile. *Journal of Industrial Microbiology & Biotechnology*. 2013 (40) 1263-1271.
- [42] Rangel-Ch, vez LG, Neria-Gonz, lez MI, *et al.* Synthesis of CdS Nanocrystals by Employing the By-Products of the Anaerobic Respiratory Process of *Desulfovibrio alaskensis* 6SR Bacteria. *Journal of Nanomaterials*. 2015 (2015) 260397.
- [43] Fuku X, Diallo A, Maaza M. Nanoscaled Electrocatalytic Optically Modulated ZnO Nanoparticles through Green Process of *Punica granatum* L. and Their Antibacterial Activities. *International Journal of Electrochemistry*. 2016 (2016) 4682967.
- [44] Spangler LC, Lu L, Kiely CJ, Berger BW, McIntosh S. Biomineralization of PbS and PbS–CdS core–shell nanocrystals and their application in quantum dot sensitized solar cells. *Journal of Materials Chemistry A*. 2016 (4) 6107-6115.
- [45] Wang B, Zeng C, Chu KH, Wu D, Yip HY, Ye L, *et al.* Enhanced Biological Hydrogen Production from *Escherichia coli* with Surface Precipitated Cadmium Sulfide Nanoparticles. *Advanced Energy Materials*. 2017 (7) 1700611.
- [46] Wei W, Sun P, Li Z, Song K, Su W, Wang B, *et al.* A surface-display biohybrid approach to light-driven hydrogen production in air. *Science Advances*. 2018 (4) 9253.

- [47] Kornienko N, Sakimoto KK, Herlihy DM, Nguyen SC, Alivisatos AP, Harris CB, *et al.* Spectroscopic elucidation of energy transfer in hybrid inorganic–biological organisms for solar-to-chemical production. *Proceedings of the National Academy of Sciences*. 2016 (113) 11750-11755.
- [48] Sakimoto KK, Zhang SJ, Yang P. Cysteine–Cystine Photoregeneration for Oxygenic Photosynthesis of Acetic Acid from CO<sub>2</sub> by a Tandem Inorganic–Biological Hybrid System. *Nano Letters*. 2016 (16) 5883-5887.
- [49] Cao Y, Feng Y, Ryser MD, Zhu K, Herschlag G, Cao C, *et al.* Programmable assembly of pressure sensors using pattern-forming bacteria. *Nature Biotechnology*. 2017 (35) 1087-1093.
- [50] Chang C-H, Lee Y-L. Chemical bath deposition of CdS quantum dots onto mesoscopic TiO<sub>2</sub> films for application in quantum-dot-sensitized solar cells. 2007 (91) 053503.
- [51] Contreras MA, Romero MJ, To B, Hasoon F, Noufi R, Ward S, *et al.* Optimization of CBD CdS process in high-efficiency Cu(In,Ga)Se<sub>2</sub>-based solar cells. *Thin Solid Films*. 2002 (403-404) 204-211.
- [52] Nair PK, Nair MTS, Garcia VM, Arenas OL, Pena Y, Castillo A, *et al.* Semiconductor thin films by chemical bath deposition for solar energy related applications. *Solar Energy Materials and Solar Cells*. 1998 (52) 313-344.
- [53] Ortega - Borges R, Lincot D. Mechanism of Chemical Bath Deposition of Cadmium Sulfide Thin Films in the Ammonia - Thiourea System In Situ Kinetic Study and Modelization. *Journal of the Electrochemical Society*. 1993 (140) 3464-3473.
- [54] Pavaskar NR, Menezes CA, Sinha APB. Photoconductive CdS films by a chemical bath deposition process. *Journal of the Electrochemical Society*. 1977 (124) 743-748.
- [55] Rakhshani AE, Al-Azab AS. Structure and morphology of chemical bath-deposited CdS films and clusters. *Applied Physics A: Materials Science & Processing*. 2001 (73) 631-636.
- [56] Wang H, Bai Y, Zhang H, Zhang Z, Li J, Guo L. CdS quantum dots-sensitized TiO<sub>2</sub> nanorod array on transparent conductive glass photoelectrodes. *The Journal of Physical Chemistry C*. 2010 (114) 16451-16455.
- [57] Pauporté T, Lincot D. Electrodeposition of semiconductors for optoelectronic devices: results on zinc oxide. *Electrochimica Acta*. 2000 (45) 3345-3353.
- [58] Sasikala G, Dhanasekaran R, Subramanian C. Electrodeposition and optical characterisation of CdS thin films on ITO-coated glass. *Thin Solid Films*. 1997 (302) 71-76.

- [59] Xu D, Chen D, Xu Y, Shi X, Guo G, Gui L, *et al.* Preparation of II-VI group semiconductor nanowire arrays by dc electrochemical deposition in porous aluminum oxide templates. *Pure and applied chemistry*. 2000 (72) 127-135.
- [60] Yu X-Y, Liao J-Y, Qiu K-Q, Kuang D-B, Su C-Y. Dynamic study of highly efficient CdS/CdSe quantum dot-sensitized solar cells fabricated by electrodeposition. *ACS Nano*. 2011 (5) 9494-9500.
- [61] Khanlary M, Townsend P, Ullrich B, Hole DE. Ion-beam luminescence of thin-film CdS on glass formed by pulsed-laser deposition. *Journal of applied physics*. 2005 (97) 023512.
- [62] Ullrich B, Sakai H, Segawa Y. Optoelectronic properties of thin film CdS formed by ultraviolet and infrared pulsed-laser deposition. *Thin Solid Films*. 2001 (385) 220-224.
- [63] Ullrich B, Schroeder R. Green single-and two-photon gap emission of thin-film CdS formed by infrared pulsed-laser deposition on glass. *Quantum Electronics, IEEE Journal of*. 2001 (37) 1363-1367.
- [64] Compaan AD, Gupta A, Lee S, Wang S, Drayton J. High efficiency, magnetron sputtered CdS/CdTe solar cells. *Solar Energy*. 2004 (77) 815-822.
- [65] Moon B-S, Lee J-H, Jung H. Comparative studies of the properties of CdS films deposited on different substrates by RF sputtering. *Thin Solid Films*. 2006 (511) 299-303.
- [66] Paudel NR, Wieland KA, Compaan AD. Ultrathin CdS/CdTe solar cells by sputtering. *Solar Energy Materials and Solar Cells*. 2012 (105) 109-112.
- [67] Punnoose A, Marafi M, Prabu G, El - Akkad F. CdS thin films prepared by RF magnetron sputtering in Ar atmosphere. *physica status solidi (a)*. 2000 (177) 453-458.
- [68] Shao M, Fischer A, Grecu D, Jayamaha U, Bykov E, Contreras - Puente G, *et al.* Radio - frequency - magnetron - sputtered CdS/CdTe solar cells on soda - lime glass. *Applied physics letters*. 1996 (69) 3045-3047.
- [69] Cortes A, Gomez H, Marotti RE, Riveros G, Dalchiele EA. Grain size dependence of the bandgap in chemical bath deposited CdS thin films. *Solar energy materials and solar cells*. 2004 (82) 21-34.
- [70] Mahdi MA, Kasem SJ, Hassen JJ, Swadi AA. Structural and optical properties of chemical deposition CdS thin films. *Thin Solid Films*. 2009 (518) 1259-1262.
- [71] Mekis I, Talapin DV, Kornowski A, Haase M, Weller H. One-pot synthesis of highly luminescent CdSe/CdS core-shell nanocrystals via organometallic and "greener" chemical approaches. *The Journal of Physical Chemistry B*. 2003 (107) 7454-7462.

- [72] Prasad K, Jha AK. Biosynthesis of CdS nanoparticles: An improved green and rapid procedure. *Journal of Colloid and Interface Science*. 2010 (342) 68-72.
- [73] Sanghi R, Verma P. A facile green extracellular biosynthesis of CdS nanoparticles by immobilized fungus. *Chemical Engineering Journal*. 2009 (155) 886-891.
- [74] Gupta A, Compaan AD. All-sputtered 14% CdS/CdTe thin-film solar cell with ZnO: Al transparent conducting oxide. *Applied Physics Letters*. 2004 (85) 684-686.
- [75] Gupta A, Parikh V, Compaan AD. High efficiency ultra-thin sputtered CdTe solar cells. *Solar Energy Materials and Solar Cells*. 2006 (90) 2263-2271.
- [76] Romeo N, Bosio A, Tedeschi R, Romeo A, Canevari V. A highly efficient and stable CdTe/CdS thin film solar cell. *Solar Energy Materials and Solar Cells*. 1999 (58) 209-218.
- [77] Ahmad A, Mukherjee P, Mandal D, Senapati S, Khan MI, Kumar R, *et al.* Enzyme mediated extracellular synthesis of CdS nanoparticles by the fungus, *Fusarium oxysporum*. *Journal of the American Chemical Society*. 2002 (124) 12108-12109.
- [78] Wang CL, Maratukulam PD, Lum AM, Clark DS, Keasling JD. Metabolic engineering of an aerobic sulfate reduction pathway and its application to precipitation of cadmium on the cell surface. *Applied and environmental microbiology*. 2000 (66) 4497-4502.
- [79] Marusak KE, Feng Y, Eben CF, Payne ST, Cao Y, You L, *et al.* Cadmium sulphide quantum dots with tunable electronic properties by bacterial precipitation. *RSC Adv*. 2016 (6) 76158-76166.
- [80] Feng Y, Ngaboyamahina E, Marusak KE, Cao Y, You L, Glass JT, *et al.* Hybrid (Organic/Inorganic) Electrodes from Bacterially Precipitated CdS for PEC/Storage Applications. *The Journal of Physical Chemistry C*. 2017 (121) 3734-3743.
- [81] Patterson AL. The Scherrer formula for X-ray particle size determination. *Physical review*. 1939; (6) 978-982.
- [82] Chen Z, Jaramillo TF, Deutsch TG, Kleiman-Shwarsstein A, Forman AJ, Gaillard N, *et al.* Accelerating materials development for photoelectrochemical hydrogen production: Standards for methods, definitions, and reporting protocols. *Journal of Materials Research*. 2010 (25) 3-16.
- [83] Mansur HS. Quantum dots and nanocomposites. *Wiley Interdiscip Rev Nanomed Nanobiotechnol*. 2010 (2) 113-129.
- [84] Murphy CJ, Coffey JL. QuantumDots: APrimer. *Applied Spectroscopy*. 2002 (56) 16-27.

- [85] Pesika NS, Stebe KJ, Searson PC. Determination of the Particle Size Distribution of Quantum Nanocrystals from Absorbance Spectra. *Advanced Materials*. 2003 (15) 1289-1291.
- [86] Sotirios B, Andreas FT. Size-dependent band gap of colloidal quantum dots. *Journal of Applied Physics*. 2006 (99) 013708.
- [87] Li Q, Guo B, Yu J, Ran J, Zhang B, Yan H, *et al.* Highly efficient visible-light-driven photocatalytic hydrogen production of CdS-cluster-decorated graphene nanosheets. *Journal of the American Chemical Society*. 2011 (133) 10878-10884.
- [88] Navarro RM, Sanchez-Sanchez MC, Alvarez-Galvan MC, Del Valle F, Fierro JLG. Hydrogen production from renewable sources: biomass and photocatalytic opportunities. *Energy & Environmental Science*. 2009 (2) 35-54.
- [89] QingáLu G. Enhanced photocatalytic hydrogen evolution by prolonging the lifetime of carriers in ZnO/CdS heterostructures. *Chemical communications*. 2009 (23) 3452-3454.
- [90] Sathish M, Viswanathan B, Viswanath RP. Alternate synthetic strategy for the preparation of CdS nanoparticles and its exploitation for water splitting. *International Journal of Hydrogen Energy*. 2006 (31) 891-898.
- [91] Wang G, Yang X, Qian F, Zhang JZ, Li Y. Double-sided CdS and CdSe quantum dot co-sensitized ZnO nanowire arrays for photoelectrochemical hydrogen generation. *Nano Lett*. 2010 (10) 1088-1092.
- [92] Kitano M, Hara M. Heterogeneous photocatalytic cleavage of water. *Journal of Materials Chemistry*. 2010 (20) 627-641.
- [93] Byoung-Yong C, Su-Moon P. Electrochemical Impedance Spectroscopy. *Annual Review of Analytical Chemistry*. 2010 (3) 207-229.
- [94] Gratzel RvdKM. *Photoelectrochemical Hydrogen Production*. 2012.
- [95] Ramprakash Y, Subramanian V, Krishnakumar R, Lakshmanan AS, Venkatesan VK. Photoelectrochemical study of screen-printed cadmium sulphide electrodes. *Journal of Power Sources*. 1988 (24) 41-50.
- [96] M. MfBBLWNKK-HPA]BACMAFSEWJ. Determination of Flat-band Position of CdS Crystals, Films, and Powders by Photocurrent and Impedance Techniques. Photoredox Reactoin Mediated by Intragap States. *J Phys Chem*. 1985 (89) 5676-5681.
- [97] Memming DMR. Photoelectrochemistry of Cadmium Sulfide. 1. Reanalysis of Photocorrosion and Flat-band Potential. *J Phys Chem*. 1988 (92) 3476-3483.
- [98] Gimenez SB, J. *Photoelectrochemical Solar Fuel Production: From Basic Principles to Advanced Devices*. Springer International Publishing: 2016.

- [99] Rajeshwar K. Fundamentals of Semiconductor Electrochemistry and Photoelectrochemistry. Encyclopedia of Electrochemistry. 2007.
- [100] Aliyev MAS, El-rouby M. Electrochemical Studies on the Cathodic Electrodeposition of n-type semiconductor CdS thin film from Thiosulfate Acidic Aqueous Solution. International Journal of Thin Films Science and Technology. 2013 (2) 195-205.
- [101] Miller E, Dinh H, Chen Z. Photoelectrochemical water splitting; standards, experimental methods, and protocols. 2013.
- [102] Leff DV, Brandt L, Heath JR. Synthesis and Characterization of Hydrophobic, Organically-Soluble Gold Nanocrystals Functionalized with Primary Amines. Langmuir. 1996 (12) 4723-4730.
- [103] Stankovich S, Dikin DA, Dommett GH, Kohlhaas KM, Zimney EJ, Stach EA, *et al.* Graphene-based composite materials. Nature. 2006 (442) 282-286.
- [104] Aricò AS, Bruce P, Scrosati B, Tarascon J-M, van Schalkwijk W. Nanostructured materials for advanced energy conversion and storage devices. Nature Materials. 2005 (4) 366-377.
- [105] Lee JB, Chen Z, Allen MG, Rohatgi A, Arya R. A miniaturized high-voltage solar cell array as an electrostatic MEMS power supply. Journal of Microelectromechanical Systems. 1995 (4) 102-108.
- [106] Tarascon JM, Armand M. Issues and challenges facing rechargeable lithium batteries. Materials for Sustainable Energy. 2012.
- [107] Zhang LL, Zhao XS. Carbon-based materials as supercapacitor electrodes. Chemical Society Reviews. 2009 (38) 2520-2531.
- [108] Alexandru V, Neelam S, Charudatta G, Pulickel MA. Design Considerations for Unconventional Electrochemical Energy Storage Architectures. Advanced Energy Materials. 2015 (5) 1402115.
- [109] Tsutomu M, Takurou NM. The photocapacitor: An efficient self-charging capacitor for direct storage of solar energy. Applied Physics Letters. 2004 (85) 3932-3934.
- [110] Xiao W, Zhao L, Gong Y, Liu J, Yan C. Preparation and performance of poly(vinyl alcohol) porous separator for lithium-ion batteries. Journal of Membrane Science. 2015 (487) 221-228.
- [111] Zang J, Cao C, Feng Y, Liu J, Zhao X. Stretchable and high-performance supercapacitors with crumpled graphene papers. Sci Rep. 2014 (4) 6492.
- [112] Nogueira AF, Longo C, De Paoli MA. Polymers in dye sensitized solar cells: overview and perspectives. Coordination Chemistry Reviews. 2004 (248) 1455-1468.

- [113] Wu K, Lei C, Yang W, Chai S, Chen F, Fu Q. Surface modification of boron nitride by reduced graphene oxide for preparation of dielectric material with enhanced dielectric constant and well-suppressed dielectric loss. *Composites Science and Technology*. 2016 (134) 191-200.
- [114] Li C, Yang S, Zheng B, Zhou T, Yuan H, Xiao D. Cadmium sulfide nanotubes thin films: Characterization and photoelectrochemical behavior. *Thin Solid Films*. 2012 (520) 2520-2525.
- [115] Liang X, Liu J, Zeng D, Li C, Chen S, Li H. Hydrogen generation promoted by photocatalytic oxidation of ascorbate and glucose at a cadmium sulfide electrode. *Electrochimica Acta*. 2016 (198) 40-48.
- [116] Kamat PV, Christians JA. Solar Cells versus Solar Fuels: Two Different Outcomes. *J Phys Chem Lett*. 2015 (6) 1917-1918.
- [117] Feng X, Mao W, Yan W. The critical conversion efficiency of light energy to hydrogen from photocatalytic water decomposition. *International Journal of Hydrogen Energy*. 2008 (33) 3644-3650.
- [118] Zhang J, Wang Y, Jin J, Zhang J, Lin Z, Huang F, *et al.* Efficient visible-light photocatalytic hydrogen evolution and enhanced photostability of core/shell CdS/g-C<sub>3</sub>N<sub>4</sub> nanowires. *ACS Appl Mater Interfaces*. 2013 (5) 10317-10324.
- [119] Rajabi HR. Photocatalytic Activity of Quantum Dots. *Semiconductor Photocatalysis - Materials, Mechanisms and Applications*. 2016.
- [120] Reshak AH. Quantum dots in photocatalytic applications: efficiently enhancing visible light photocatalytic activity by integrating CdO quantum dots as sensitizers. *Phys Chem Chem Phys*. 2017 (19) 24915-24927.
- [121] Koleilat GI, Levina L, Shukla H, Myrskog SH, Hinds S, Pattantyus-Abraham AG, *et al.* Efficient, Stable Infrared Photovoltaics Based on Solution-Cast Colloidal Quantum Dots. *ACS Nano*. 2008 (2) 833-840.
- [122] Ben-Shahar Y, Scotognella F, Waiskopf N, Kriegel I, Dal Conte S, Cerullo G, *et al.* Effect of surface coating on the photocatalytic function of hybrid CdS-Au nanorods. *Small*. 2015 (11) 462-471.
- [123] Lee JR, Li W, Cowan AJ, Jäckel F. Hydrophilic, Hole-Delocalizing Ligand Shell to Promote Charge Transfer from Colloidal CdSe Quantum Dots in Water. *The Journal of Physical Chemistry C*. 2017 (121) 15160-15168.
- [124] Yuan M, Liu M, Sargent EH. Colloidal quantum dot solids for solution-processed solar cells. *Nature Energy*. 2016 (1) 16016.

- [125] Harvey D. Analytical Chemistry Textbook Maps. Map: Analytical Chemistry 2.0 (Harvey). 2016, 472-489.
- [126] Chen J-L, Zhu C-Q. Functionalized cadmium sulfide quantum dots as fluorescence probe for silver ion determination. *Analytica Chimica Acta*. 2005 (546) 147-153.
- [127] Barreca D, Gasparotto A, Maragno C, Tondello E. Nanostructured Cadmium Sulfide Thin Films by XPS. *Surface Science Spectra*. 2002 (9) 46-53.
- [128] Xu P, Milstein TJ, Mallouk TE. Flat-Band Potentials of Molecularly Thin Metal Oxide Nanosheets. *ACS Applied Materials & Interfaces*. 2016 (8) 11539-11547.
- [129] Gelderman K, Lee L, Donne SW. Flat-Band Potential of a Semiconductor: Using the Mott-Schottky Equation. *Journal of Chemical Education*. 2007 (84) 685-688.
- [130] dos Santos WS, Rodriguez M, Afonso AS, Mesquita JP, Nascimento LL, Patrocínio AOT, *et al.* A hole inversion layer at the BiVO<sub>4</sub>/Bi<sub>4</sub>V<sub>2</sub>O<sub>11</sub> interface produces a high tunable photovoltage for water splitting. *Scientific Reports*. 2016 (6) 31406.
- [131] Ramsden JJ, Grätzel M. Photoluminescence of small cadmium sulphide particles. *Journal of the Chemical Society, Faraday Transactions 1: Physical Chemistry in Condensed Phases*. 1984 (80) 919-933.
- [132] Joswig J-O, Springborg M, Seifert G. Structural and Electronic Properties of Cadmium Sulfide Clusters. *The Journal of Physical Chemistry B*. 2000 (104) 2617-2622.
- [133] Brown PR, Kim D, Lunt RR, Zhao N, Bawendi MG, Grossman JC, *et al.* Energy Level Modification in Lead Sulfide Quantum Dot Thin Films through Ligand Exchange. *ACS Nano*. 2014 (8) 5863-5872.
- [134] Kroupa DM, Vörös M, Brawand NP, McNichols BW, Miller EM, Gu J, *et al.* Tuning colloidal quantum dot band edge positions through solution-phase surface chemistry modification. *Nature Communications*. 2017 (8)15257.
- [135] Melitz W, Shen J, Kummel AC, Lee S. Kelvin probe force microscopy and its application. *Surface Science Reports*. 2011 (66) 1-27.
- [136] Novikov A. Experimental measurement of work function in doped silicon surfaces. *Solid-State Electronics*. 2010 (54) 8-13.
- [137] Sasaki K. Study on Work Function of the {0001} Faces of CdS Crystal. I. *Japanese Journal of Applied Physics*. 1974 (13) 933-938.
- [138] Miller EM, Kroupa DM, Zhang J, Schulz P, Marshall AR, Kahn A, *et al.* Revisiting the Valence and Conduction Band Size Dependence of PbS Quantum Dot Thin Films. *ACS Nano*. 2016 (10) 3302-3311.

- [139] Marusak KE, Krug JR, Feng Y, Cao Y, You L, Zauscher S. Bacterially driven cadmium sulfide precipitation on porous membranes: Toward platforms for photocatalytic applications. *Biointerphases*. 2018 (13) 011006.
- [140] George SM. Atomic Layer Deposition: An Overview. *Chemical Reviews*. 2010 (110) 111-131.
- [141] Dasgupta NP, Meng X, Elam JW, Martinson ABF. Atomic Layer Deposition of Metal Sulfide Materials. *Accounts of Chemical Research*. 2015 (48) 341-348.
- [142] Gregory BW, Stickney JL. Electrochemical atomic layer epitaxy (ECALE). *Journal of Electroanalytical Chemistry and Interfacial Electrochemistry*. 1991 (300) 543-561.
- [143] Foresti ML, Pezzatini G, Cavallini M, Aloisi G, Innocenti M, Guidelli R. Electrochemical Atomic Layer Epitaxy Deposition of CdS on Ag(111): An Electrochemical and STM Investigation. *The Journal of Physical Chemistry B*. 1998 (102) 7413-7420.
- [144] Öznülüer T, Erdoğan İ, Şişman İ, Demir Ü. Electrochemical Atom-by-Atom Growth of PbS by Modified ECALE Method. *Chemistry of Materials*. 2005 (17) 935-937.
- [145] Zang J, Cao C, Feng Y, Liu J, Zhao X. Stretchable and High-Performance Supercapacitors with Crumpled Graphene Papers. *Scientific Reports*. 2014 (4) 6492.

## Biography

Yaying Feng received his Doctor of Philosophy in Mechanical Engineering & Materials Science in December of 2019 at Duke University in Durham, NC, USA. He received his Master of Science in Mechanical Engineering & Materials Science in December of 2015 and Master of Science in Electrical & Computer Engineering in December of 2019 at Duke University. Previously, he had received his Bachelor of Science in Materials Physics in July of 2013 at University of Science and Technology Beijing in Beijing, P.R. China.

### Published papers:

1. Y. Feng, K. Marusak, L. You, S. Zauscher, "Biosynthetic Transition Metal Chalcogenide Semiconductor Nanoparticles: Progress in Synthesis, Property Control and Applications", *Current Opinion in Colloid & Interface Science*, 2018, 38, 190
2. Y. Feng, E. Egaboyamahina, K. Marusak, Y. Cao, L. You, J. Glass, S. Zauscher, "Hybrid (organic/inorganic) electrode from bacterially precipitated CdS for PEC/storage applications", *The Journal of Physical Chemistry C*, 2017, 121, 7, 3734
3. Y. Feng, "Characterization of Bacterially Precipitated Cadmium Sulfide Nanoparticles for Photoelectrochemical Applications", Duke University, Master Thesis
4. C. Cao#, Y. Feng#, J. Zang#, X. Zhao, "Tunable lotus-leaf and rose-petal effects via graphene paper origami", *Extreme Mechanics Letters*, 2015, 4, 18 (#: Equal contribution)
5. J. Zang#, C. Cao#, Y. Feng#, J. Liu, X. Zhao, "Stretchable and high-performance supercapacitors with crumpled graphene papers", *Scientific Reports*, 2014, 4: 6492 (#: Equal contribution)
6. K. Marusak, Y. Feng, C. Eben, S. Payne, Y. Cao, L. You, S. Zauscher, "Cadmium sulphide quantum dots with tunable electronic properties by bacterial precipitation", *RSC Advance*, 2016, 6, 76158

7. Y. Cao, Y. Feng, M. Ryser, K. Zhu, G. Herschlag, K. Marusak, S. Zauscher, L. You, "Programmed assembly of pressure sensors using pattern-forming bacteria", *Nature Biotechnology*, 2017, 35, 11, 1087
8. K. Marusak, J. Krug, Y. Feng, Y. Cao, L. You, S. Zauscher, "Bacterially driven cadmium sulfide precipitation on porous membranes: Toward platforms for photocatalytic applications", *Biointerphases*, 2018, 13, 1, 011006
9. X. Chen, X. Yan, Z. Bai, P. Lin, Y. Shen, X. Zheng, Y. Feng, Y. Zhang, "Facile fabrication of large-scale patterned ZnO nanorod arrays with tunable arrangement, period and morphology", *CrystEngComm*, 15, 39, 8022